LEIBNITZ INSTITUT FÜR FESTKÖRPER- UND WERKSTOFFFORSCHUNG

FAKULTÄT MATHEMATIK UND NATURWISSENSCHAFTEN
DER TECHNISCHEN UNIVERSITÄT DRESDEN

Investigation of renormalization effects in high temperature cuprate superconductors

Dissertation
zur Erlangung des akademischen Grades
Doctor rerum naturalium (Dr. rer. nat.)

vorgelegt von
Volodymyr B. Zabolotnyy
geboren am 18. Februar 1981 in Mykolaiv (Ukraine)

Institute for Solid State Research, IFW Dresden
P. O. Box 270116, D-01171 Dresden, Germany.

Eingereicht am 17.10.2007

Berichterstatter

1. Gutachter: **Prof. Dr. Bernd Büchner**
IFW Dresden
P. O. Box 270116
D-01171 Dresden

2. Gutachter: **Jun.-Prof. Dr. Ilya Eremin**
Institute für Mathematische und Theoretische Physik
TU-Braunschweig
38106 Braunschweig

3. Gutachter: **Dr. Tonica Valla**
Brookhaven National Laboratory, USA
20 Pennsylvania Street
P. O. Box 5000
Upton, NY 11973-500

Verteidigt am 16.04.2008

Contents

Abstract

Superconductivity happens to be one of the most marvelous and exciting phenomena in the solid state physics. After its first observation in 1911 by Kamerlingh Onnes [1] it took almost 50 years to gain microscopic understanding of the phenomenon [2–5]. Nonetheless, when Bednorz and Müller discovered the high temperature superconductivity in La–Ba–Cu oxide ceramics, the theories found themselves as perplexed as 50 years ago when trying to explain the effect. Though there is no commonly accepted theory of high temperature superconductivity, certain progress has been made in understanding these new materials. Nowadays there is enough evidence to believe that electrons in high-T_C materials are coupled in Cooper pairs [6–8], while the pairing media still remains under debates. Obviously, the properties of the pairing interaction must affect the electronic structure of a high temperature superconductor, in particular its electronic self-energy. As the angle resolved photoemission proved to be the best fitted tool to probe the occupied electronic states with accuracy of few meV and momentum resolution $\Delta\mathbf{k} \lesssim 0.01\,\text{Å}^{-1}$, allowing one for detection of fine effects in the self-energy, it has been found that the self-energy of high-T_C cuprates indeed exhibits a well pronounced structure, which is currently attributed to coupling of the electrons either to lattice vibrations or to collective magnetic excitations in the system. To clarify this issue, the renormalization effects and the electronic structure of two cuprate families $\mathrm{Bi_2Sr_2CaCu_2O_{8+\delta}}$ and $\mathrm{YBa_2Cu_3O_{7-\delta}}$ were chosen as the main subject for this thesis.

Layout of the thesis *Chapter 1* starts from the general introduction into the angle resolved photoemission. Basic things such as the three step model and the origin for the conservation of the parallel component of photoelectron quasimomentum are discussed. The notion of quasiparticles (one particle excitations) in photoemission is explained in details. After a brief introduction of the Green's functions and the spectral function, the sudden approximation frequently used in photoemission is enlightened to provide the reader with the "feeling" to which extent the photoemission intensity and the spectral function can be treated as identical

entities.

Chapter 2 continues the formal and relatively strict exposition to show what kind of spectral function one expects in the superconducting state based on the BCS theory. With a simple example of an electronic system coupled to a collective mode unusual renormalization features observed in the photoemission spectra are introduced.

Chapter 3 deals with technical aspects of angle resolved photoemission, such as sample preparation and handling of the raw experimental data, in particular Fermi surface mapping and determination of the sample doping based on it. Though this part might seem too technical, one should not underestimate its value, as improper data handling in most of the cases produces a lot of “new physics” and unexpected effects.

In *Chapter 4*, after introducing the sample properties and briefly reviewing the earlier results on renormalization in Bi-2212 cuprate family current results on Zn and Ni impurity substituted samples are presented. It is shown that impurity substitution in general leads to suppression of the unusual renormalization, which is found to be in consent with the behaviour of the neutron resonance mode observed in inelastic neutron scattering experiments under introduction of impurities.

Since early photoemission data for the Y-123 family is much more controversial, *Chapter 5* contains an extended discussion of the photoemission spectra for this compound. It is shown that due to cleavage issues the sample surface, which is primarily contributing to the spectrum, turns out to be overdoped, which explains the difficulties with observation of the superconducting gap and renormalization for Y-123. To substantiate the hypothesis of the overdoped surface layer and disentangle surface and bulk photoemission, spectra measured with circularly polarised light are discussed in details. Finally an alternative possibility to obtain a purely superconducting surface of Y-123 via partial substitution of Y atoms with Ca is introduced. It is shown that renormalization in the superconducting Y-123 has similar strong momentum dependence as in the Bi-2212 family. It is also shown that in analogy to Bi-2212 the renormalization appears to have strong dependence on the doping level (no kinks for the overdoped component) and practically vanishes above T_C suggesting that coupling to magnetic excitations fits much better than competing scenarios, according to which the unusual renormalization in ARPES spectra is caused by the coupling to single or multiple phononic modes.

Chapter 1

Theoretical aspects of angle resolved photoemission

The electronic subsystem determines numerous properties of solids. Electric conductivity, optical and magnetic properties, heat capacity and the still not completely understood phenomenon of high temperature superconductivity are governed by the electrons. Therefore it is clear that detailed knowledge of the electronic structure is necessary to get better understanding of all these phenomena.

Photoemission happens to be the most direct and the most convenient tool to study the electrons in solids. Although, at first glance the method seems to be rather simple, developing a strict theory that would accurately account for all relevant effects appears to be a real challenge [9–11]. As the different level of approximations are often used to interpret the experimental data, a clear idea of the limits within which each approximation remains valid is a necessary prerequisite for the correct understanding of the experimental data. Therefore, along with the introduction into the theoretical aspects of the method, the aim of the chapter is to give the feeling of those limitations.

1.1 Introduction

At the heart of all various types of photoelectron spectroscopies (UPS, XPS, ARPES) lies the photoelectron effect initially discovered by H. Hertz [12] and later on explained by A. Einstein [13]. In Fig. 1.1 a general sketch of a photoemission experiment is given. When the beam of monochromatic light is shone on the sample and the energy of photons $h\nu$ is enough to excite the electrons bound in the solid

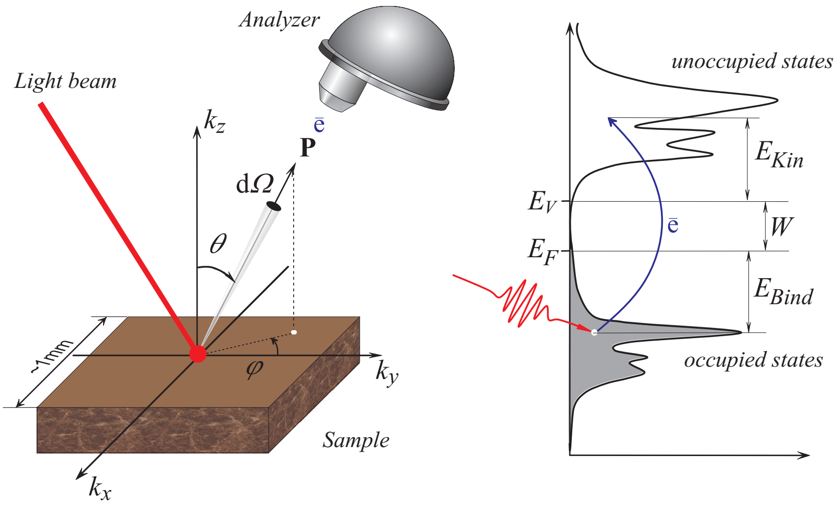

Figure 1.1: General principles and geometry of ARPES experiment.

above the vacuum level E_0 they will start to leave the sample. Hence measuring their kinetic energy and using simple energy conservation considerations one can find the binding energy of the levels from which the electrons were excited:

$$h\nu - E_{\text{Binding}} - W = \mathscr{E}_{\text{kinetic}}, \tag{1.1}$$

This is, in principle, what is called the X-ray photoelectron spectroscopy (XPS), i.e., when relatively high photon energies ($h\nu = 2000 - 100$ eV) are used to probe the core levels of atoms comprising the solid. Already this comparatively unsophisticated technique has found numerous applications, one of which is analysis of chemical composition.

In the solid with periodic lattice the eigenstates of the delocalized valence electrons can be approximated by the Bloch waves that, in addition to the energy, are also characterized by their quasimomentum. Unlike the angle integrated spectroscopy, where all photoelectrons are treated alike, irrelevant of the direction of their momentum **P**, the angle resolved photoelectron spectroscopy (ARPES) treats such electrons as contributors to independent spectra. In the early experimental setups this was achieved via a finite acceptance angle of the analysers, while the new generation machines make use of special electronic optics allowing simultaneous recording of several hundreds of spectra corresponding to a certain range of directions of the photoelectron momentum. The angular resolution makes it possible to recover the quasimomentum of the initial states from which the electrons were excited and hence to obtain the dispersion of low lying conduction and valence bands. Further technical details of this procedure will be discussed in the next chapter.

1.2 Three step model, photoemission for the noninteracting electron gas in a periodic potential

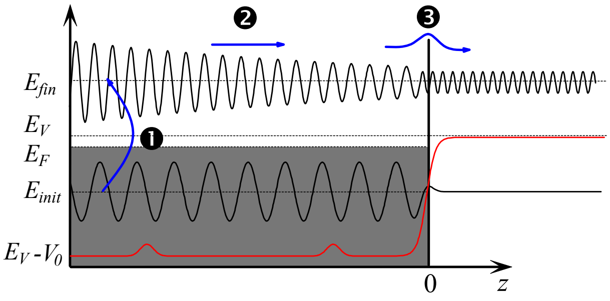

Figure 1.2: Schematic representation of the three step model. The red curve corresponds to a crystal potential.

The three step model is one of the earliest assumptions used to estimate the photoelectron intensity [14–16]. Although this model was shown to be a rather crude approximation [17] and current numerical methods are now well advanced to calculate the photocurrent within the so-called one-step model [17,18] the three step model was a rather successful approach and still does not lose its value providing intuitive insight into the photoemission process.

In the three step model it is assumed that the intensity of photoemission can be calculated as a product of three independent steps that do not interfere one with another:

- optical excitation of the initial bulk state $|\Psi_{\mathrm{init}}\rangle$ into the excited one $|\Psi_{\mathrm{fin}}\rangle$;
- propagation of the excited photoelectron to the surface;
- transition through the solid-vacuum interface.

To illustrate each step the solid will be treated as a non-interacting electron gas in the infinite 3-dimensional crystal with effective periodic potential $V(\mathbf{r}) = V(\mathbf{r}+\mathbf{a}_1 m_1+\mathbf{a}_2 m_2+\mathbf{a}_3 m_3)$, $\{m_1, m_2, m_3\} \subset \mathbb{Z}$.

Optical excitation. At the stage of optical excitation the three step model completely neglects the presence of the surface that breaks the translational symmetry along one of the spatial dimensions, so that the final and initial eigenstates are supposed to be 3-dimensional Bloch waves:

$$\psi^{\mathrm{3D}}_{\nu,\mathbf{k}}(\mathbf{r}) = u^{\mathrm{3D}}_{\nu}(\mathbf{r})\, e^{i\mathbf{k}\mathbf{r}}, \tag{1.2}$$

where ν is a zone number, $\mathbf{k}$ is the electron *quasimomentum*, and $u_\nu(\mathbf{r})$ is a periodic in lattice function, whose actual form depends upon the effective potential $V(\mathbf{r})$.

Considering the light as a perturbation to the system Hamiltonian within the

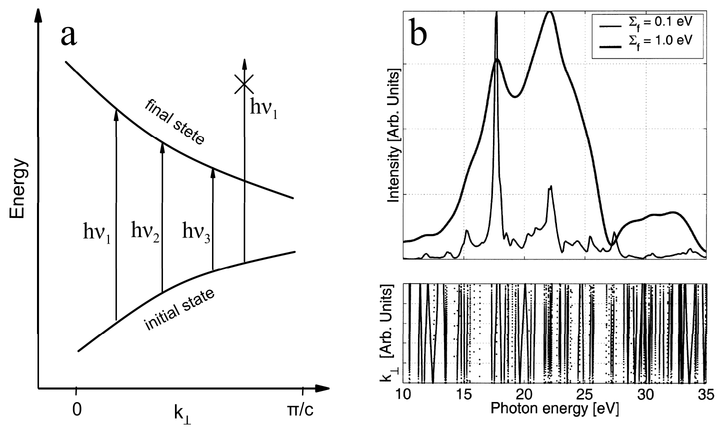

Figure 1.3: (a) Dispersion of initial and final states. Momentum component parallel to the surface kept constant $\mathbf{k}_{\|}$=const. Varying the photon energy allows to probe transitions at different $\mathbf{k}_{\perp}$. (b) Calculated band structure for Bi-2212 at $\mathbf{k}_{\|} = (\pi/a, 0, 0)$ [19]. Owing to finite lifetime of the final states $\tau = 1/\Sigma$ "forbidden" transitions become possible.

frames of time dependent perturbation theory [20] the transition probability is proportional to the matrix element of the perturbation operator Δ between the initial and final states:

$$w_{\text{init,fin}} \sim \frac{2\pi}{\hbar} \left| \langle \Psi^{\text{fin}} | \Delta | \Psi^{\text{fin}} \rangle \right|^2 \delta(E^{\text{fin}} - E^{\text{init}} - h\nu), \tag{1.3}$$

where the perturbation to the Hamiltonian by the electromagnetic field is given by

$$\Delta = \frac{e}{2mc}(\mathbf{A}\hat{\mathbf{p}} + \hat{\mathbf{p}}\mathbf{A} - e\Phi + \frac{e^2}{2mc^2}\mathbf{A}^2). \tag{1.4}$$

Here $\hat{\mathbf{p}}$ is the momentum operator, Φ and $\mathbf{A}$ are the scalar and the vector potential of the electromagnetic field respectively. For the usually used light intensities the quadratic in $\mathbf{A}$ term can be safely neglected. Quite often near-surface induced fields are neglected as well, and only the bulk photoemission is taken to be the major contributor to the photocurrent. In this case the term div$\mathbf{A}$ arising form expanding the combination $\hat{\mathbf{p}}\mathbf{A}$ is zero.† Therefore for the plane wave with a wave vector $\mathbf{q}$ and the actual Bloch waves for the initial and final states the formula for the transition

---

† Although, this is not always justified, as there are known cases when the term div$\mathbf{A}$ results in a significant modification of the matrix element (1.3) [21] or even indirect transitions [22].

probability reduces to: [†]

$$
\begin{aligned}
w_{\mathrm{init,fin}} &\sim \left|\langle u_{\nu_{\mathrm{fin}},\mathbf{k}_{\mathrm{fin}}}(\mathbf{r})\, e^{i\mathbf{k}_{\mathrm{fin}}\mathbf{r}} | \mathbf{A}_0 e^{i\mathbf{qr}} \cdot \nabla | u_{\nu_{\mathrm{init}},\mathbf{k}_{\mathrm{init}}}(\mathbf{r})\, e^{i\mathbf{k}_{\mathrm{init}}\mathbf{r}} \rangle\right|^2 \delta(E^{\mathrm{fin}} - E^{\mathrm{init}} - h\nu) \\
&= \left| \int\limits_{\text{one unit cell}} u^*_{\nu_{\mathrm{fin}},\mathbf{k}_{\mathrm{fin}}}(\mathbf{r})\, u_{\nu_{\mathrm{init}},\mathbf{k}_{\mathrm{init}}}(\mathbf{r})\, \mathbf{A}_0 (\nabla V(\mathbf{r}))\, e^{i(\mathbf{q}+\mathbf{k}_{\mathrm{init}}-\mathbf{k}_{\mathrm{fin}})\mathbf{r}}\, \mathrm{d}\,\mathbf{r} \right|^2 \\
&\qquad \times \left| \sum_{\mathbf{G}} e^{i(\mathbf{q}+\mathbf{k}_{\mathrm{init}}-\mathbf{k}_{\mathrm{fin}})\mathbf{G}} \right|^2 \delta(E^{\mathrm{fin}} - E^{\mathrm{init}} - h\nu) \\
&= |M_{\mathrm{fin,\ init}}|^2 \delta(\mathbf{q}+\mathbf{k}_{\mathrm{init}} - \mathbf{k}_{\mathrm{fin}}) \delta(E^{\mathrm{fin}} - E^{\mathrm{init}} - h\nu).
\end{aligned}
\tag{1.5}
$$

For the excitation with low photon energies ($h\nu \lesssim 100\,\mathrm{eV}$) the photon momentum $\mathbf{q}$ is negligibly small as compared to the size of the Brillouin zone, which leads to well known rule of “vertical” optical transitions, i.e. $\mathbf{k}_{\mathrm{init}} = \mathbf{k}_{\mathrm{fin}}$. It also becomes obvious that a fixed initial state cannot be excited by any photon energy, as there might not be a finale state that would satisfy the condition $E^{\mathrm{fin}} - E^{\mathrm{init}} - h\nu = 0$.

Although, in its simplest formulation, the three step model does not account properly for the scattering effects and for the fact that the excited electron actually escapes the solid, and therefore, strictly speaking, cannot be an eigenstate, one still may account for these effects ascribing a finite life time for the finale state. This remits the problem of final states making initially “forbidden” transitions possible (see Fig. 1.3).

From equation 1.5 also follows that the transition probability has a certain dependence on the symmetry of the initial and final states, the so-called *dipole selection rules* [23, 24]. The case, when the initial and final states are symmetric or antisymmetric with respect to reflections in some mirror plane $\mathfrak{M}$, is the simplest example. In this case the useful symmetry properties of the matrix elements can be summarized in the following way:

$$
\begin{aligned}
\langle \mathrm{even} | \mathbf{A}(\mathbf{r}) \nabla | \mathrm{odd} \rangle &= 0 \quad \text{if } \mathbf{A}(\mathbf{r}) \text{ is odd with respect to } \mathfrak{M}; \\
\langle \mathrm{even} | \mathbf{A}(\mathbf{r}) \nabla | \mathrm{even} \rangle &= 0 \quad \text{if } \mathbf{A}(\mathbf{r}) \text{ is even with respect to } \mathfrak{M}; \\
\langle \mathrm{odd} | \mathbf{A}(\mathbf{r}) \nabla | \mathrm{odd} \rangle &= 0 \quad \text{if } \mathbf{A}(\mathbf{r}) \text{ is even with respect to } \mathfrak{M}.
\end{aligned}
\tag{1.6}
$$

[†] Here a so-called acceleration form for the matrix element is used: $\langle \psi_{\mathrm{fin}} | \mathbf{A} \nabla | \psi_{\mathrm{init}} \rangle = \langle \psi_{\mathrm{fin}} | \mathbf{A}(\nabla V) | \psi_{\mathrm{init}} \rangle / (E_{\mathrm{init}} - E_{\mathrm{fin}})$, where V is a crystal potential and ψ_{init} , ψ_{fin} are the eigenstates with corresponding energies.

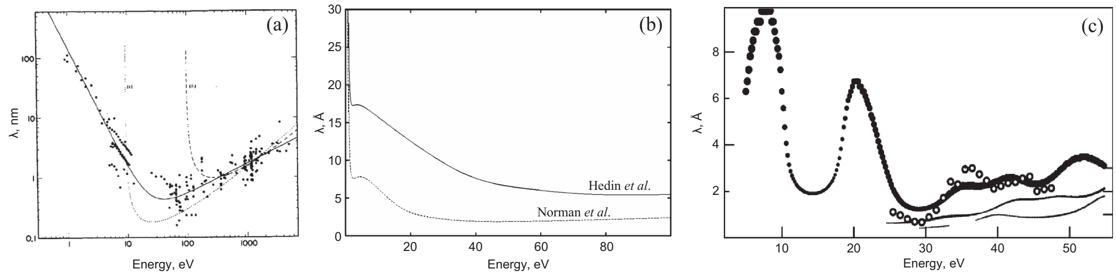

Figure 1.4: (a) Universal curve for electron mean free path (IMFP) after Seach et al. [27]. (b) Calculated values of IMFP in Bi-2212 [28, 29]. (c) Influence of elastic scattering on electron escape depth in graphite. The empty circles correspond to experimental data, the filled symbols are the result of calculations [30]. The pronounced dip at about 15 eV is due to elastic scattering effects.

The selection rules are often helpful in establishing the symmetry of final/initial state [25], as well as when one needs to choose the correct light polarization in order to enhance or suppress the emission from the state of known symmetry [26].

Propagation of the excited photoelectron to the surface. Usually the propagation of the excited state is treated phenomenologically in terms of an electron mean free path λ. The main factor limiting the electron escape depth λ is inelastic electron scattering due to electron-electron and electron-phonon interactions. Seach et al. [27] analysing the experimental data for the inelastic mean free path in various materials showed that its value follows a typical universal curve, with a minimum of about 5–20 Å at the energy region of 50–100 eV [Fig. 1.4(a)]. This rather small electron escape depth is actually the reason for considering the photoemission as surface sensitive technique.

Along with the purely phenomenological approach to the problem there are also theoretical attempts to estimate λ. For the low energy electrons ($E_{\mathrm{kin}} \lesssim 5\,\mathrm{keV}$) a traditional way to account for interaction with electron excitations is a dielectric theory. The probability for the electron being scattered with energy loss of $\hbar\omega$ and momentum loss of $\mathbf{q}$ is given by $\frac{d\hbar\omega\, d\mathbf{q}}{\pi a_{\mathrm{Bohr}} E \mathbf{q}} \,\mathrm{Im}\, \frac{1}{\varepsilon(\mathbf{q},\omega)}$. Based on this, both Norman et al. [29] and Hedin and Lee [28] made their estimates for the inelastic mean free path in Bi-2212. Unfortunately the EELS data [31] used for the estimates of $\varepsilon(\mathbf{q},\omega)$, was available only for $\mathbf{q} = 0.1$ Å^{-1}, so that different assumptions as for the dispersion were necessary to be made, which resulted in λ values that differs by about 2–3 times [Fig. 1.4(b)].

The elastic scattering, as pointed out in [30], may also have notable impact on the photoemission, especially at low kinetic energies (5-20 eV), when it becomes comparable to those of the inelastic scattering. As an example in Fig. 1.4(c) the results of theoretical calculations and experimental data for λ in graphite are given, where the pronounced dips at energies about 15 eV and 30 eV can hardly be overlooked. However when discussing the inelastic scattering effects one needs to be cautious lest counting the same thing twice. Because of the artificial splitting of the photoemission process into three steps, the elastic scattering can also be understood in terms of band structure effects, i.e. strong damping of the Bloch waves, whose energies and quasi-momenta fall into the regions of band gaps. Since the elastic scattering can be thought of as a diffraction off the crystal potential it is supposed to be especially strong for layered materials owing their highly modulated crystal potential. As a result appearance of diffraction minima along certain directions in **k**-space may occur in photoemission for such materials.

Transition through the solid-vacuum interface. At the first step it was natural to regard a crystal as a structure having strict 3-dimensional translational symmetry, although even there such an assumption was not the best one. At the step, where the surface is directly involved, it is necessary to account for the lack of the translational symmetry along the direction perpendicular to the sample surface. It can be easily shown that in this case the general form of the eigenfunction characterised by the energy $\mathscr{E}(\mathbf{k})$ is

$$\psi^{2\mathrm{D}}_{\nu,\mathbf{k}}(\mathbf{r}_{\|},z) = u^{2\mathrm{D}}_{\nu}(\mathbf{r}_{\|},z)e^{i\mathbf{k}_{\|}\mathbf{r}_{\|}}, \tag{1.7}$$

where $u^{2\mathrm{D}}_{\nu}(\mathbf{r}_{\|},z)$ is only periodic along $\mathbf{a}_1$ and $\mathbf{a}_2$ directions, which are taken here to be parallel to the sample surface. It is obvious that deep in the bulk this function asymptotically behaves like its 3D counterpart $\psi^{3\mathrm{D}}_{\nu,\mathbf{k}}(\mathbf{r})$, while in the vacuum, far enough from the surface, it has to be an eigenfunction of the free electron Hamiltonian $\hat{H}_0 = -\frac{\hbar^2\nabla^2}{2m}$ with the same eigenvalue $\mathscr{E}(\mathbf{k})$, which is just the experimentally measured kinetic energy of the photoelectrons. Expanding the periodic function $u^{2\mathrm{D}}_{\nu}(\mathbf{r}_{\|},z)$ in a series and representing the non-periodic in z coefficients $u^{2\mathrm{D}}_{G_x,G_y}(z)$ as Fourier integrals yields [†]

[†] For brevity of notation the zone index ν has been ommited.

$$\begin{aligned}\hat{H}_0\psi^{2\mathrm{D}}_{\nu,\mathbf{k}}(\mathbf{r}_{||},z) &= \hat{H}_0\sum_{\mathbf{G}_{||}}\int u^{2\mathrm{D}}_{\mathbf{G}_{||}}(p_z)e^{i\left((\mathbf{k}_{||}+\mathbf{G}_{||})\mathbf{r}_{||}+p_z z/\hbar\right)}dp_z\; e^{i\mathbf{k}_{||}\mathbf{r}_{||}} \\ &= \sum_{\mathbf{G}_{||}}\int\left(\frac{\hbar^2(\mathbf{k}_{||}+\mathbf{G}_{||})^2+p_z^2}{2m}\right)u^{2\mathrm{D}}_{\mathbf{G}_{||}}(p_z)e^{i\left(\mathbf{k}_{||}\mathbf{r}_{||}+p_z z/\hbar\right)}dp_z,\end{aligned} \tag{1.8}$$

here $\mathbf{G}_{||}$ stands for parallel to the surface components of reciprocal lattice vectors. Therefore, for $\psi^{2\mathrm{D}}_{\nu,\mathbf{k}}(\mathbf{r}_{||},z)$ to be an eigenfunction of $\hat{H}_0$ with eigenvalue $\mathscr{E}(\mathbf{k})$ requires from the coefficients $u^{2\mathrm{D}}_{\mathbf{G}_{||}}(p_z)$ to be of the form:

$$u^{2\mathrm{D}}_{\mathbf{G}_{||}}(p_z) = \tilde{u}^{2\mathrm{D}}_{\mathbf{G}_{||}}\delta\left(p_z-\tilde{p}_z(\mathbf{G}_{||})\right),\ \text{with}\ \tilde{p}_z(\mathbf{G}_{||}) = \sqrt{2m\mathscr{E}(\mathbf{k})-\hbar^2\mathbf{G}^2_{||}}. \tag{1.9}$$

That is, the electron wave function, far from the surface, is just a sum of plane waves, whose momentum components parallel to the surface equals to the parallel component of quasimomentum in the bulk $\hbar\mathbf{k}_{||}$ up to the parallel component of the reciprocal lattice vector $\hbar\mathbf{G}_{||}$, while the energy with respect to Hamiltonian H_0 is $\mathscr{E}(\mathbf{k})$:

$$\psi^{2\mathrm{D}}_{\nu,\mathbf{k}}(\mathbf{r}_{||},z) = \sum_{\mathbf{G}_{||}}\tilde{u}^{2\mathrm{D}}_{\mathbf{G}_{||}}e^{i(\mathbf{k}_{||}+\mathbf{G}_{||})\mathbf{r}_{||}+i\tilde{p}_z(\mathbf{G}_{||})z/\hbar}, \tag{1.10}$$

which is frequently referred as to a conservation of parallel component of the electron momentum [32]:

$$\mathbf{p}_{||} = \hbar\mathbf{k}_{||}+\hbar\mathbf{G}_{||}. \tag{1.11}$$

The equation (1.11) tells us that the (real) momentum distribution of the photoelectrons contains multiple instances of the band structure shifted by all possible vectors $\hbar\mathbf{G}_{||}$, for which the corresponding p_z are still positive reals, i.e. when the electrons are still able to overcome the surface barrier. The photoemission with $\mathbf{G}_{||}=0$ is sometimes called a primary cone, while all the others are referred to as secondary cones [11]. The alternative notation would be the 1st Brillouin zone for the primary cone, and the 2nd zone, etc. for the secondary cones. This is somehow reminiscent of the extended zone scheme, but has nothing to do with it. The extended zone scheme is just a convenient way of representing the band structure, while the photointensity distributions with their primary and secondary cones are real physical entities. The intensity variation between the different cones, which

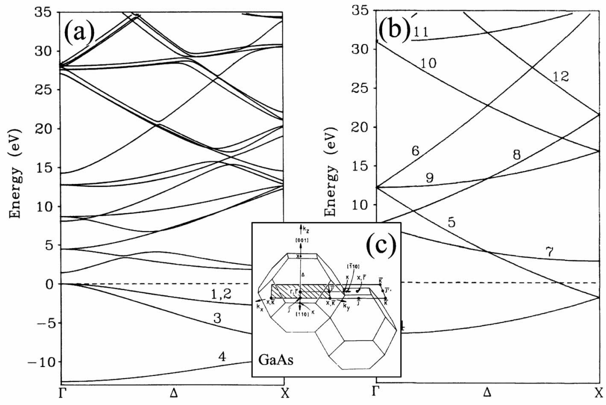

Figure 1.5: GaAs band structure after Ref. 33. (a) Result of empirical calculation. (b) A hypothetical case for a free-electron parabola case.

corresponds to the same initial and final states, is determined by the crystal potential at the surface, i.e. how the bulk solution inside the crystal can be "stitched" to a set of plane waves outside it.

Solving the equation $\mathscr{E}_{\text{fin}}(\hbar\mathbf{k}_{\|}, \mathbf{k}_z) = \mathscr{E}(\mathbf{k})$, the value for $\mathbf{k}_z$ can be obtained. The most straightforward way to do this, is to assume the final states to be plane waves with the energy $\mathscr{E}_{\text{fin}}(\mathbf{k}_{\|}^{\text{fin}}, \mathbf{k}_z^{\text{fin}}) = \hbar^2(\mathbf{k}_{\|}^2 + \mathbf{k}_z^2)/2m + V_0$, where V_0 is a crystal inner potential (see Fig. 1.2). In this case

$$\mathbf{k}_z = \sqrt{\frac{\mathscr{E}(\mathbf{k}) - V_0}{\hbar^2} - \mathbf{k}_{\|}^2}. \tag{1.12}$$

For the high excitation energies this seems to be a rather good approximation. For instance, comparing the calculated band structure for GaAs with the free-electron model† (Fig. 1.5), one sees that, while in the low energy range (0-20 eV) there are considerable discrepancies, at the energies of 30 eV and higher the calculated band structure becomes close to a free-electron case. For the cases, when the free-electron approximation for the final state breaks down, it is possible to obtain $\mathbf{k}_z$ for some high symmetry directions [34] without extra assumptions about the final state. However, in general it is necessary to know the dispersion of the final state $\mathscr{E}_{\text{fin}}(\mathbf{k})$, which, for instance, can be taken as an input from a theoretical calculation. There are also cases when the required final state dispersion was obtained from the LEED experiments [35,36].

As we see the extraction of $\mathbf{k}_z$ dispersion from ARPES data turns out to be a rather involved procedure, that is why the great deal of its success as a band mapping technique ARPES owes to the quasi two-dimensional compounds, where the $\mathbf{k}_z$

---

† Zero crystal potential still can be regarded as periodic in lattice, which allows description in terms of Bloch functions, while the dispersion is just a free-electron parabola folded into the 1st Brillouin zone.

dispersion is negligibly small and does not cause any difficulties. More detail, concerning the treatment of experimental data will be addressed in the corresponding chapter.

1.3 Many body system, one-particle excitations. Lifetime of the quasiparticles.

When dealing with a system consisting of interacting particles one cannot any longer single out a separate particle and ascribe to it some dispersion or energy levels. Particles lose their identities and only for the total system such entities as momentum and energy can be defined. Therefore, the previously discussed notion of noninteracting particles gives only an approximate description of real many-body systems, and the one-particle dispersion turns out to be a mere abstraction. Nonetheless the net behaviour of the system consisting of interacting particles can be a reminiscent of a non-interacting system. In such cases, one still can think of the interacting system as if being comprised of some effective quasiparticles. This subchapter is meant to give an idea how the extension to the interacting case can be made and what the quasiparticles actually are.

For simplicity let us assume that the system consists of N fermions of the same type. If the particles are not interacting one with another but only with some external potential, the Hamiltonian $\hat{H}_{\mathrm{tot}} = \sum_i^N \hat{H}_i$ splits into a sum of one-particle terms $\hat{H}_i$, and the problem reduces to finding the spectrum $\{E_n\}$ and the set of eigenfunctions $\{\varphi_n()\}$ of the one-particle equation $\hat{H}_i \varphi_n(\mathbf{r}_i) = E_n \varphi_n(\mathbf{r}_i)$, that would theoretically give a full description of the system properties. Any Slater determinant $\psi_A(\mathbf{r}_1, ..., \mathbf{r}_N) \equiv \det|\varphi_{\nu_{A,i}}(\mathbf{r}_j)|$ composed by a set of one-particle functions $A = \{\varphi_{\nu_{A,1}}, ..., \varphi_{\nu_{A,N}}\} \subset \{\varphi_n\}$ will be an eigenfunction of the N-particle system with the eigenenergy E_A given by the sum of one-particle energies $E_A = E_{\nu_{A,1}} + \cdots + E_{\nu_{A,N}}$. If at some moment t_0 the N-particle wave function $\Psi(\mathbf{r}_1, ..., \mathbf{r}_N, t_0) = \psi_A(\mathbf{r}_1, ..., \mathbf{r}_N)$, then its time evolution will be given by $\Psi(\mathbf{r}_1, ..., \mathbf{r}_N, t) = e^{-iE_A(t-t_0)/\hbar}\psi_A(\mathbf{r}_1, ..., \mathbf{r}_N)$, which is essentially the same Slater determinant up to a phase factor, i.e. the occupancy of the states $\{\varphi_{\nu_{A,1}}, ..., \varphi_{\nu_{A,N}}\}$ does not change with time. This is actually the reason why in the non-interacting case one can speak about separate particles that are occupying certain states. To treat such states it is more convenient to use the formalism of creation and annihilation operators. The state $\psi_A(\mathbf{r}_1, ...\mathbf{r}_N)$ can

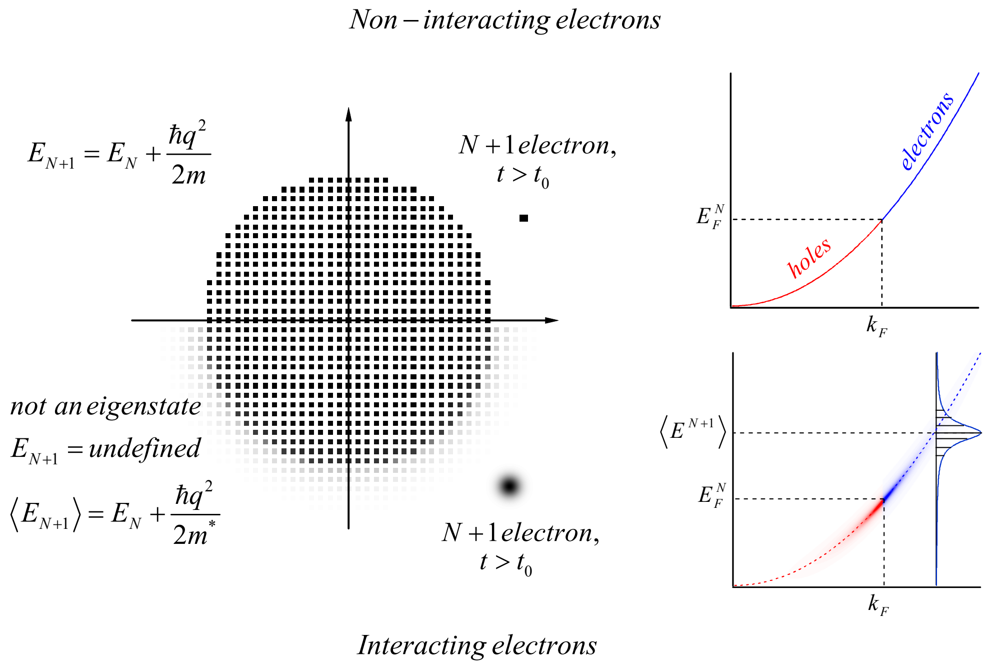

Figure 1.6: One particle excitation of the non-interacting and interacting Fermi sea of electrons. The graphs to the right show the dispersion of the electron/hole excitations.

be written as $\hat{c}^\dagger_{\nu_{A,N}}...\hat{c}^\dagger_{\nu_{A,1}}|0\rangle$, where $|0\rangle$ corresponds to an empty 0×0 determinant, i.e. a system containing 0 particles, while the action of each following operator $\hat{c}^\dagger_{\nu_{A,k}}$ results in adding a row $\varphi_{\nu_{A,k}}(\mathbf{r}_1), ..., \varphi_{\nu_{A,k}}(\mathbf{r}_k)$ and a column $\varphi_{\nu_{A,1}}(\mathbf{r}_k), ..., \varphi_{\nu_{A,k}}(\mathbf{r}_k)$ to the previous determinant of size $k-1 \times k-1$. In the case of interacting system such a simple description fails and the Slater determinants built out of one-particle functions are no longer eigenstates.

However, when studying a many-body system its response to certain excitations rather than the wave function itself is of prior interest. One of such excitations could be adding or removing of one particle, which is particularly interesting with respect to *direct* and *inverse* photoemission processes. Consider the Fermi sea of N non-interacting electrons $|\mathrm{FS}_N\rangle = \hat{c}^\dagger_{\mathbf{k}_N}...\hat{c}^\dagger_{\mathbf{k}_1}|0\rangle$ in a ground state with energy $E_N = \hbar^2(\mathbf{k}_1^2 + ... + \mathbf{k}_N^2)/2m$, $|\mathbf{k}_i| \leq k_{\mathrm{Fermi}}$ and total momentum $\mathbf{P}_{\mathrm{system}} = 0$. Adding another electron in the state above the Fermi sphere $\varphi_{\mathbf{q}}(\mathbf{r}) = e^{i\mathbf{qr}}$, $|\mathbf{q}| \geq k_{\mathrm{Fermi}}$ would result in the excited state of the system $\hat{c}^\dagger_{\mathbf{q}}|\mathrm{FS}_N\rangle$ with a well-defined energy $E_{N+1} = E_N + \hbar^2\mathbf{q}^2/2m$ and total momentum $\mathbf{P}_{\mathrm{system}} = \hbar\mathbf{q}$, as the excited state is also an eigen one. Such one-particle excitation one can call an *electron* and ascribe to it a dispersion $\mathscr{E}_{\mathrm{el}}(\mathbf{q}) = E_{N+1}(\mathbf{q}) - E_N = \hbar\mathbf{q}^2/2m$. Similarly, one can consider removing of a particle from under the Fermi sphere, and call such an excitation a *hole* with dispersion $\mathscr{E}_{\text{hole}}(\mathbf{q}) = E_N - E_{N-1}(\mathbf{q}) = \hbar\mathbf{q}^2/2m$ (see graph in Fig. 1.6)[†]. As the excited state is an eigenstate for the system Hamiltonian its time evolution will have just an exponential pre-factor $\exp(-iE_{N+1}(t-t_0)/\hbar)$ in front of $\hat{c}^\dagger_{\mathbf{q}}|\text{FS}_N\rangle$. Therefore, if later on, at moment t, one would like to "remove" the added electron, the electron will be found with 100% probability where it has been "left": $\left|\langle \text{FS}_N|\exp(+iE_N(t-t_0)/\hbar)\hat{c}_{\mathbf{q}}\exp(-iE_{N+1}(t-t_0)/\hbar)\hat{c}^\dagger_{\mathbf{q}}|\text{FS}_N\rangle\right|^2 = \left|\langle \text{FS}_N|\hat{c}_{\mathbf{q}}\hat{c}^\dagger_{\mathbf{q}}|\text{FS}_N\rangle\right|^2 = 1$. Similar, with 100% probability the hole state will remain unoccupied. It is natural to refer to the described effects of well-defined dispersion of excitations and the related stationary excited states as to infinite lifetime of the one-particle excitation.

In the case of an interacting system, N-particle eigenstates $|N, E_i\rangle$ with eigenenergies E_i are some linear combinations of the size $N \times N$ Slater determinants, therefore adding a particle to the ground state of interacting system $|\text{FS}^{\text{int}}_N\rangle \neq |\text{FS}_N\rangle$ would generally result in a mixed $N+1$-particle state $\hat{c}^\dagger_{\mathbf{q}}|\text{FS}^{\text{int}}_N\rangle = \sum_i a_i|N+1, E_i\rangle$, where $|N+1, E_i\rangle$ are the eigenstates for the $N+1$ particle problem with corresponding eigenenergies E_i. Therefore the energy measurements of the excited state will result in different values E_i with probabilities $|a_i|^2$. The time evolution of the excited state will be such that the interference between different components $|N+1, E_i\rangle$ will "scatter" the added particle from its initial one-particle state $\varphi_{\mathbf{q}}(\mathbf{q}) = e^{i\mathbf{q}\mathbf{r}}$:

$$\begin{aligned}
&\left|\left\langle \text{FS}^{\text{int}}_N, (t-t_0)\right|\hat{c}_{\mathbf{q}}\sum_i a_i\left|N+1, E_i, (t-t_0)\right\rangle\right|^2 \\
&\qquad = \left|\left\langle \text{FS}^{\text{int}}_N\right| e^{\frac{iE_n(t-t_0)}{\hbar}}\sum_i a_i e^{\frac{-iE_i(t-t_0)}{\hbar}}\hat{c}_{\mathbf{q}}\left|N+1, E_i\right\rangle\right|^2 \\
&\qquad = \left|\sum_{i,j} a_i a_j^* e^{\frac{-iE_i(t-t_0)}{\hbar}}\left\langle N+1, E_j\middle|N+1, E_i\right\rangle\right|^2 \\
&\qquad\qquad = \left|\sum_i |a_i|^2 e^{\frac{-iE_i(t-t_0)}{\hbar}}\right|^2 \leq \left|\sum_i |a_i|^2\right|^2 \equiv 1^2. \qquad (1.13)
\end{aligned}$$

For the cases of weakly interacting particles the set of coefficients $\{a_i\}$ is such

---

[†] When doing the statistical averaging in the system containing a big number of particles N, the N is assumed to be a variable and the energies are counted from the chemical potential. Using this convention the hole dispersion can be written as $\mathscr{E}_{\text{hole}}(\mathbf{q}) = E_N - \mu N - (E_{N-1}(\mathbf{q}) - \mu(N-1)) = \hbar\mathbf{q}^2/2m - \mu$. Similar holds for adding an electron.

that the distribution of measured energies[†] $\zeta(E) = \sum_i |a_i|^2 E_i$ is close to a gaussian peaked at some average $\langle E_{N+1}\rangle$ with a characteristic width $\Delta\langle E_{N+1}\rangle$. It can be shown that in this case the filling of the one-particle state $\varphi_{\mathbf{q}}(\mathbf{q})$ will be exponentially decaying at rate $\left|\sum_i |a_i|^2 e^{\frac{-iE_i(t-t_0)}{\hbar}}\right|^2 \sim e^{-\frac{\Delta E_{N\pm1}(t-t_0)}{\hbar}} = e^{-\frac{(t-t_0)}{\tau}}$. Usually in such a case it is said that there are quasiparticle excitations in the system with dispersion $\mathscr{E}_{\text{el,hole}} = \pm\left(\langle E_{N\pm1}(\mathbf{q})\rangle - E_N\right) = \hbar^2\mathbf{q}^2/2m^*$. The effective mass m^* merely accounts for the fact that the dispersion differs from the non-interacting case, which is a so-called mass renormalization effect. However in certain phenomena on a time scale τ such excitations would behave like real particles with mass m^*, which is the main motivation for introducing the idea of a quasiparticle.

The rigorous treatment of the many-body problem and one-particle excitations is achieved via the machinery of Green's functions, whose advantage is that they can be perturbatively computed from the Green's functions of the non-interacting system. In the next paragraph the main definitions for the Green's functions and their relation to the spectral function will be given.

1.4 Green's function and the spectral function $A(\mathbf{k},\omega)$

There are several types of Green's functions used in literature. Here accents are made only on those that have immediate relation to the interpretation of inverse and direct photoemission experiments.

The retarded Green's function $G^{\mathrm{R}}_{\nu_2,\nu_1}(t_2,t_1)$, $G^{>}_{\nu_2,\nu_1}(t_2,t_1)$, and $G^{<}_{\nu_2,\nu_1}(t_2,t_1)$ for fermions at zero temperature in the one-particle basis $\{\varphi_\nu\} \equiv \{|\nu\rangle\}$ are defined as

$$\begin{aligned}
G^{\mathrm{R}}_{\nu_2,\nu_1}(t_2,t_1) &= -i\theta(t_2-t_1)\langle\Psi_0|\hat{c}_{\nu_2}(t_2)\hat{c}^\dagger_{\nu_1}(t_1) + \hat{c}^\dagger_{\nu_1}(t_1)\hat{c}_{\nu_2}(t_2)|\Psi_0\rangle,\\
G^{<}_{\nu_2,\nu_1}(t_2,t_1) &= +i\langle\Psi_0|\hat{c}^\dagger_{\nu_1}(t_1)\hat{c}_{\nu_2}(t_2)|\Psi_0\rangle,\\
G^{>}_{\nu_2,\nu_1}(t_2,t_1) &= -i\langle\Psi_0|\hat{c}_{\nu_2}(t_2)\hat{c}^\dagger_{\nu_1}(t_1)|\Psi_0\rangle,
\end{aligned} \tag{1.14}$$

where $|\Psi_0\rangle$ denotes the ground state of the many-particle system. Averaging over the temperature distribution of the state $|\Psi\rangle$ allows to extend these correlators to

---

[†] Note the analogy with Energy Distribution Curve in ARPES spectra.

the case of finite temperature T [†]

$$G^{<}_{\nu_2,\nu_1}(t_2,t_1)=\frac{i}{Z}\sum_n e^{-\frac{E_n}{kT}}\langle n|\hat{c}^{\dagger}_{\nu_1}(t_1)\hat{c}_{\nu_2}(t_2)|n\rangle, \text{where } Z=\sum_n e^{-\frac{E_n}{kT}}. \tag{1.15}$$

Here the summation runs over all eigenstates $|n\rangle$ characterized by energies E_n. Similar holds for the remaining Green's functions. Inserting the identity matrix $\sum_m |m\rangle\langle m|$, with $|m\rangle$ being the eigenstates of the system Hamiltonian, into (1.15) and expanding the time evolution of the $\hat{c}$-operators allows to obtain Lehmann's representation for the Green's function, which reveals certain properties of this function related to the one-particle excitation spectrum discussed previously.

$$\begin{aligned}G^{<}_{\nu_2,\nu_1}(t_2-t_1)&=\sum_{n,m}\frac{ie^{-\frac{E_n}{kT}}}{Z}\langle n|\hat{c}^{\dagger}_{\nu_1}(t_1)|m\rangle\langle m|\hat{c}_{\nu_2}(t_2)|n\rangle\\&=\sum_{n,m}\frac{ie^{-\frac{E_n}{kT}}}{Z}\langle n|\hat{c}^{\dagger}_{\nu_1}|m\rangle\langle m|\hat{c}_{\nu_2}|n\rangle e^{\frac{-i(E_n-E_m)(t_2-t_1)}{\hbar}}\end{aligned}\tag{1.16}$$

Taking the Fourier transform of this result and making similar calculations for the other two Green's functions we arrive at:

$$\begin{aligned}G^{<}_{\nu_2,\nu_1}(\omega)=&\frac{+2\pi i}{Z}\sum_{n,m}e^{-\frac{E_n}{kT}}\langle n|\hat{c}^{\dagger}_{\nu_1}|m\rangle\langle m|\hat{c}_{\nu_2}|n\rangle\delta(E_n-E_m-\omega),\\G^{>}_{\nu_2,\nu_1}(\omega)=&\frac{-2\pi i}{Z}\sum_{n,m}e^{-\frac{E_n}{kT}}\langle n|\hat{c}_{\nu_2}|m\rangle\langle m|\hat{c}^{\dagger}_{\nu_1}|n\rangle\delta(E_n-E_m+\omega),\\G^{\mathrm{R}}_{\nu_2,\nu_1}(\omega)=&\frac{-i}{Z}\int_0^{+\infty}\sum_{n,m}e^{-\frac{E_n}{kT}}\Big(\langle n|\hat{c}_{\nu_2}|m\rangle\langle m|\hat{c}^{\dagger}_{\nu_1}|n\rangle e^{+\frac{i(E_n-E_m)(t_2-t_1)}{\hbar}}\\&+\langle n|\hat{c}^{\dagger}_{\nu_1}|m\rangle\langle m|\hat{c}_{\nu_2}|n\rangle e^{-\frac{i(E_n-E_m)(t_2-t_1)}{\hbar}}\Big)e^{i(\omega+i\eta)(t_2-t_1)}\mathrm{d}(t_2-t_1)\\=&\frac{1}{Z}\sum_{n,m}(e^{-\frac{E_m}{kT}}+e^{-\frac{E_n}{kT}})\frac{\langle n|\hat{c}_{\nu_2}|m\rangle\langle m|\hat{c}^{\dagger}_{\nu_1}|n\rangle}{E_n-E_m+\omega+i\eta}.\end{aligned}\tag{1.17}$$

To understand how the introduced Green's functions are related to what has been discussed in the previous subchapter, consider, for example, the diagonal element of $G^{<}_{\nu_{\mathbf{k}},\nu_{\mathbf{k}}}(\omega)$ defined in the one-particle basis of plane waves $\nu_{\mathbf{k}}\in\{e^{i\mathbf{kr}}\}$ at $T=0$. In this case $G^{<}_{\nu_{\mathbf{k}},\nu_{\mathbf{k}}}(\omega)=\sum_m\left|\langle m|\hat{c}_{\nu_{\mathbf{k}}}|n_0\rangle\right|^2\delta(E_{n_0}-E_m-\omega)$. Here $|n_0\rangle$ is the state

---

[†] This should not be mixed with the Matsubara Green's functions of imaginary time. Here the great canonical ensemble with variable particle number is used. For this case the system Hamiltonian is $\hat{H}'=\hat{H}_0-\mu\hat{N}$, where $\hat{H}_0$ is a Hamiltonian of a system with a fixed particle number. The statistical weight for a certain state is given by $w_n=\frac{1}{Z}\exp(\frac{-E'_n}{kT})$ where the partition function $Z=Z(V,T,\mu)$ depends on the system volume V, temperature T and chemical potential μ. For brevity the prime at all energies has been omitted!

of N-particle system that has the lowest energy E_{n_0}, i.e. the ground state, as only this state will be "picked up" by the summation over the initial states $|n\rangle$ at $T = 0$. The remaining m-summation runs over the ground and all excited eigenstates $|m\rangle$ of the $N-1$ particle system with well defined eigenenergies E_m. In the case of noninteracting particles there will be only one state $|m\rangle$, and only if $|\mathbf{k}| < |\mathbf{k}_{\mathrm{Fermi}}|$, giving a non-zero summand, namely $|m_{\mathbf{k}}\rangle = \hat{c}_{\nu_{\mathbf{k}}}|n_0\rangle$ with energy $E_{m_{\mathbf{k}}} = E_{n_0} - \mathbf{k}^2/2m$. Therefore the Green's function will consist of a trail of delta functions aligned along the hole dispersion $\omega = E_{n_0} - E_{m_{\mathbf{k}}} = \mathbf{k}^2/2m$. For interacting particles different states $|m\rangle$ will contribute to the sum at fixed $\mathbf{k}$, so that the hole dispersion will get smeared along the energy axis in full analogy to what has been discussed in the previous subchapter. Similarly one can find that $G^{>}_{\nu_{\mathbf{k}},\nu_{\mathbf{k}}}(\omega)$ would give the dispersion of electron-like excitation of the system, while poles of $G^{\mathrm{R}}_{\nu_{\mathbf{k}},\nu_{\mathbf{k}}}(\omega)$ combines both dispersions in one function.

Therefore it is convenient to define a spectral function as $A_{\nu_2,\nu_1}(\omega) = -2\,\mathrm{Im}\,G^{\mathrm{R}}_{\nu_2,\nu_1}(\omega)$. Using the previous formulae it can be found that:

$$\begin{aligned} A_{\nu_2,\nu_1}(\omega) = \frac{2\pi}{Z}\sum_{n,m}(e^{-\frac{E_n}{kT}} + e^{-\frac{E_m}{kT}})\langle n|\hat{c}_{\nu_2}|m\rangle\langle m|\hat{c}^{\dagger}_{\nu_1}|n\rangle\delta(E_n - E_m + \omega) \\ = +i(1 + e^{-\frac{\omega}{kT}})G^{>}_{\nu_2,\nu_1}(\omega). \end{aligned} \tag{1.18}$$

From this follows an important relation between the $G^{>/<}_{\nu_2,\nu_1}(\omega)$ functions and the spectral function that are frequently used in literature:

$$\begin{aligned} -iG^{<}_{\nu_2,\nu_1}(\omega) &= f(\omega)A_{\nu_2,\nu_1}(\omega), \\ +iG^{>}_{\nu_2,\nu_1}(\omega) &= (1 - f(\omega))A_{\nu_2,\nu_1}(\omega), \end{aligned} \tag{1.19}$$

where $f(\omega) = \frac{1}{1+e^{\frac{\omega}{kT}}}$ is the Fermi-Dirac function.

1.5 Photoemission intensity within a sudden approximation

It is intuitively clear that, since the photoemission is just removing of an electron from the many-body system, the photocurrent has to be somehow represented via $G^{<}_{\nu_2,\nu_1}(\omega)$ and the spectral function $A_{\nu_2,\nu_1}(\omega)$. In certain cases such connection indeed can be done. One is a so-called sudden approximation that is being frequently used to describe the photoemission data when the picture of noninteracting particles fails and many-body effects need to be somehow accounted for.

To calculate the photoemission intensity similarly to the one-electron case one can use the Golden rule, however now the photoemission operator Δ becomes a many-particle operator acting upon a many-particle initial $|\Psi_N^{\text{init}}\rangle$ and a final $|\Psi_N^{\text{fin}}\rangle$ state:

$$\Delta = \sum_i^N \frac{e}{2mc}(\mathbf{A}\hat{\mathbf{p}}_i + \hat{\mathbf{p}}_i\mathbf{A} - e\Phi + \frac{e^2}{2mc^2}\mathbf{A}^2), \tag{1.20}$$

where $\hat{\mathbf{p}}_i$ is the momentum operator for the i-th electron in the system. Making the same assumptions as before, (1.20) can be written as:

$$\Delta = \sum_i^N \frac{e}{mc}\mathbf{A}\hat{\mathbf{p}}_i = \sum_{m,n} \frac{e}{mc}\Delta_{m,n}\hat{a}_m^\dagger \hat{a}_n. \tag{1.21}$$

The last sum represents the second quantized form of the photoemission operator Δ, where $\Delta_{m,n} = \langle\phi_m|\Delta|\phi_n\rangle$ being the matrix elements in the one-particle basis $\{|\phi_n\rangle\}$, the same in which creation and annihilation operators are defined.

To calculate the matrix element (1.3) in the sudden approximation it is assumed that after excitation of the N-particle system the photoelectron leaves so fast that the interaction with the remaining $N-1$ particles can be neglected. It is obvious that the higher the photon energy would be, the quicker photoelectron would escape the solid and hence the more accurate would be the sudden approximation approach. Strictly speaking, one can expect this assumption to hold for rather small and localised systems like molecules. Nevertheless, early ARPES experiments showed that for the cuprates the assumption is approximately valid down to $h\nu = 20$ eV [37]. More recent laser research [38] performed with laser light source ($h\nu \sim 7$ eV) also did not reveal crucial deviations from the 20 – 100 eV measurements, suggesting that the sudden approximation possibly holds even at such low energies.

This assumptions allow considering the excited system as being comprised of two independent parts: the photoelectron and the remaining $N-1$ electron system. This, in turn, allows one to speak separately about the energy and momentum of the excited photoelectron (the later is measured experimentally) and the energy and momentum of the remaining $N-1$ electron system:

$$\begin{aligned} h\nu + E_N^{\text{init}} &\overset{\substack{\text{energy}\\ \text{conservation}}}{=} E_N^{\text{fin}} \overset{\substack{\text{sudden}\\ \text{approximation}}}{=} E_{N-1}^{\text{fin}} + \mathscr{E}_{\text{el}} \\ \mathbf{k}_{\text{photon}} + \mathbf{k}_N^{\text{init}} &\overset{\substack{\text{momentum}\\ \text{conservation}}}{=} \mathbf{k}_N^{\text{fin}} \overset{\substack{\text{sudden}\\ \text{approximation}}}{=} \mathbf{k}_{N-1}^{\text{fin}} + \mathbf{k}_{\text{el}}. \end{aligned} \tag{1.22}$$

In this simplified case the wave function of the excited system can be explicitly expressed via the wave function of the $N-1$ electron system left behind $\Psi_{N-1}^{\text{fin}}(\mathbf{r}_1, ..., \mathbf{r}_{N-1})$, and the one-electron function $\phi_f(\mathbf{r}) \in \{\phi_n()\}$ that describes the final state of the photoelectron:

$$\Psi_N^{\text{fin}}(\mathbf{r}_1, ..., \mathbf{r}_N) = \frac{1}{\sqrt{N}} \sum_{i=1}^{N} (-1)^i \Psi_{N-1}^{\text{fin}}(\mathbf{r}_1, ..., \mathbf{r}_{i-1}, \mathbf{r}_{i+1} ..., \mathbf{r}_N) \phi_f(\mathbf{r}_i). \tag{1.23}$$

Using the same one-electron basis $\{\phi_n()\}$ to introduce second quantization, the last equation can be written as $|\Psi_N^{\text{fin}}\rangle = \hat{a}_f^\dagger |\Psi_{N-1}^{\text{fin}}\rangle$.

It is necessary to mention that the final state $|\Psi_{N-1}^{\text{fin}}\rangle$ generally is not an eigenstate one for the $N-1$ particle system, it is a mixed state $|\Psi_{N-1}^{\text{fin}}\rangle = \sum_m c_m |\Psi_{N-1}^m\rangle$ and upon the detection of the photoelectron the system collapses into one of its eigenstates $|\Psi_{N-1}^m\rangle$ with probability $|c_m|^2$. This is the mechanism that results in a broadening of the photoemission peaks and is completely analogous to that discussed in the previous section. Therefore, for the transition probability between the ground initial state of the N-electron system and one of the possible excited states of the $N-1$ electron system one can write:

$$w_{0,\text{m}} = \frac{2\pi}{\hbar} \left| \langle \Psi_{N-1}^{\text{m}} | \sum_{i,k} \hat{a}_f \Delta_{k,i} \hat{a}_k^\dagger \hat{a}_i \, |\Psi_N^0\rangle \right|^2 \delta(h\nu + E_N^0 - \mathscr{E}_{\text{el}} - E_{N-1}^{\text{m}}). \tag{1.24}$$

Further simplifications can be made assuming that $\hat{a}_f|\Psi_N^0\rangle \approx 0$, which becomes an exact equation for the non-interacting case, as otherwise the system would already contain the excited photoelectron in the initial state. In the case of an interacting system, this means that the coefficients in front of the Slater determinants containing one-particle state φ_f in the expansion of the initial state are negligibly small. Therefore it is clear that the higher the one-particle energy of the state φ_f is the better such approximation would work. Therefore, using this assumption and the identity $\hat{a}_f \hat{a}_k^\dagger \hat{a}_i = \delta_{f,k}\hat{a}_i + \hat{a}_k^\dagger \hat{a}_f \hat{a}_i$ the equation (1.24) reduces to:

$$\begin{aligned} w_{0,\mathrm{m}} &= \frac{2\pi}{\hbar} \left| \langle \Psi^{\mathrm{m}}_{N-1} | \sum_i \Delta_{f,i} \hat{a}_i | \Psi^0_N \rangle \right|^2 \delta(h\nu + E^0_N - \mathscr{E}_{\mathrm{el}} - E^{\mathrm{m}}_{N-1}) \\ &= \frac{2\pi}{\hbar} \sum_{i,j} \Delta_{f,i} \Delta^*_{f,j} \langle \Psi^0_N | \hat{a}^\dagger_j | \Psi^{\mathrm{m}}_{N-1} \rangle \langle \Psi^{\mathrm{m}}_{N-1} | \hat{a}_i | \Psi^0_N \rangle \delta(h\nu + E^0_N - \mathscr{E}_{\mathrm{el}} - E^{\mathrm{m}}_{N-1}). \end{aligned} \tag{1.25}$$

Passing to a great canonical ensemble with the Hamiltonian $\hat{H}' = \hat{H}_0 - \mu\hat{N}$, as previously used in the definition of the Green's functions, the energy levels transforms as $E'_N = E_N - \mu N$. Taking this into account and summing over all possible final states $|\Psi^{\mathrm{m}}_{N-1}\rangle$ and making the thermodynamical averaging over the initial state $|\Psi^{\mathrm{n}}_N\rangle$ one gets for the photo-intensity:

$$\begin{aligned} I(\mathscr{E}_{\mathrm{el}}, f) &\sim \frac{1}{Z} \sum_{m,n} e^{-\frac{E_n - \mu N_n}{kT}} w_{\mathrm{n,m}} = \frac{2\pi}{Z\hbar} \sum_{\substack{i,j \\ m,n}} \Delta_{f,i} \Delta^*_{f,j} e^{-\frac{E_n - \mu N_n}{kT}} \langle \Psi^{\mathrm{n}}_N | \hat{a}^\dagger_j | \Psi^{\mathrm{m}}_{N-1} \rangle \\ &\times \langle \Psi^{\mathrm{m}}_{N-1} | \hat{a}_i | \Psi^{\mathrm{n}}_N \rangle \delta(E'^{\mathrm{n}}_N - E'^{\mathrm{m}}_{N-1} + \mu - \mathscr{E}_{\mathrm{el}} + h\nu) = \frac{-i}{\hbar} \sum_{i,j} \Delta_{f,i} \Delta^*_{f,j} G^<_{i,j}(\omega) \\ &= \frac{f(\omega)}{\hbar} \sum_{i,j} \Delta_{f,i} \Delta^*_{f,j} A_{i,j}(\omega), \end{aligned} \tag{1.26}$$

where $\omega = -(h\nu + \mu - \mathscr{E}_{\mathrm{el}}) = -(h\nu - (E_V - \mu) - (\mathscr{E}_{\mathrm{el}} - E_V)) = -(h\nu - W - \mathscr{E}^{\mathrm{kin}}_{\mathrm{el}}) = -E_{\mathrm{bind}}$, $\mathscr{E}^{\mathrm{kin}}_{\mathrm{el}}$ is a kinetic energy of the ejected photoelectron, and $W = E_V - \mu$ is the sample work function[†].

The Green's function can be shown to be diagonal in a certain basis if the system possesses some symmetry. For example, the Green's function of the electron gas is diagonal in the basis of plane waves $\{e^{i\mathbf{kr}}\}$ due to the invariance under translation by any vector $\mathbf{r}$. Similarly the Green's function for the electron gas in a periodic potential is diagonal in quasi-momentum $\mathbf{k}$ in the basis of Bloch waves $\{\psi_{\mathbf{q},n}\}$. Neglecting the elements non-diagonal in the zone number n, one obtains frequently listed in photoemission literature formula for the photocurrent intensity:

$$I(\omega) \sim f(\omega) \sum_{\mathbf{q},n} |\Delta_{\mathbf{q},\mathbf{k}}|^2 A_{\mathbf{q},n}(\omega). \tag{1.27}$$

[†] $\mathscr{E}_{\mathrm{el}}$ is the energy of the electron excited into the final state φ_f. To get the kinetic energy of this electrons outside the sample one needs to take a difference between this energy level and the vacuum level $\mathscr{E}^{\mathrm{kin}}_{\mathrm{el}} = \mathscr{E}_{\mathrm{el}} - E_V$. Please see Fig. 1.2.

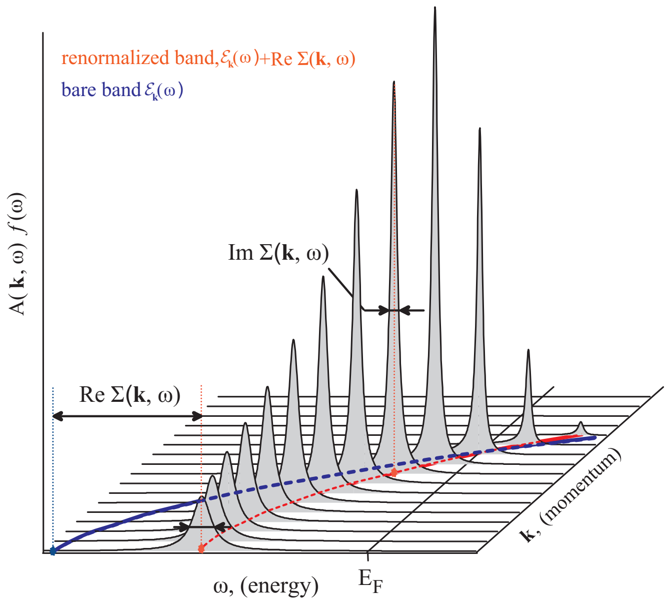

Figure 1.7: Model spectral function for Fermi liquid $A(\mathbf{k},\omega)$ multiplied by the Fermi function $f(\omega)=1/(1+e^{\frac{\omega}{kT}})$.

1.6 Green’s function of the noninteracting and interacting system. Self-energy

The important conclusion from the previous subchapter is that the APRPES signal is essentially the spectral function of a many-body system. In case of noninteracting particles with a known energy dispersion of one-particle states $\mathcal{E}_{\mathbf{k}}$ one can easily obtain the spectral representation for the retarded Green’s function $G_0^{\mathrm{R}}(\mathbf{k},\omega)$ and corresponding spectral function $A_0(\mathbf{k},\omega)$ [20]:

$$\begin{aligned} G_0^{\mathrm{R}}(\mathbf{k},\omega) &= \frac{1}{\omega-\mathcal{E}_{\mathbf{k}}+i\delta}, \\ A_0(\mathbf{k},\omega) &= -2\,\mathrm{Im}\,G_0^{\mathrm{R}}(\mathbf{k},\omega)=2\pi\delta(\omega-\mathcal{E}_{\mathbf{k}}). \end{aligned} \tag{1.28}$$

The advantage of the Green’s function formalism is that the true Green’s functions for the system with interacting particles can be perturbatively calculated from the bare ones. It follows from the theory that the Green’s function for the interacting system can be obtained from the bare one as a solution of the Dyson equation, which in the Fourier domain turns into a simple algebraic equation:

$$G^{\mathrm{R}}(\mathbf{k},\omega)=G_0^{\mathrm{R}}(\mathbf{k},\omega)+G_0^{\mathrm{R}}(\mathbf{k},\omega)\Sigma^{\mathrm{R}}(\mathbf{k},\omega)G^{\mathrm{R}}(\mathbf{k},\omega), \tag{1.29}$$

where the self-energy function $\Sigma(\mathbf{k},\omega)$ is obtained as a result of summation of Feynman diagrams [†]. The calculations are also facilitated by the fact that Σ requires the

---

[†] Similar equation holds for the advanced Green’s function. In the following, where the superscript ‘R’

summation of smaller amount of diagrams than the direct calculation of the renormalized Green's function. Since this is not an introduction into diagram calculus, taking also into account that any intelligible introduction into this field would take at least 15 pages, it is more sound to redirect the reader to the rich literature on this topic [20,39,40].

From Eq.1.29 it follows that the renormalized (full) Green's function and spectral functions can be written as:

$$\begin{aligned} G^{\mathrm{R}}(\mathbf{k},\omega) &= +\frac{G_0^{\mathrm{R}}(\mathbf{k},\omega)}{1-\Sigma(\mathbf{k},\omega)G_0^{\mathrm{R}}(\mathbf{k},\omega)} = \frac{1}{\omega-\mathscr{E}_{\mathbf{k}}-\Sigma(\mathbf{k},\omega)}, \\ A(\mathbf{k},\omega) &= \frac{1}{\pi}\frac{|\operatorname{Im}\Sigma_{\mathbf{k}}(\omega)|}{[\omega-\mathscr{E}_{\mathbf{k}}-\operatorname{Re}\Sigma(\mathbf{k},\omega)]^2+[\operatorname{Im}\Sigma(\mathbf{k},\omega)]^2}. \end{aligned} \tag{1.30}$$

To illustrate the effect of the self-energy on the spectral function in Fig. 1.7 is given the spectral function for a Fermi liquid at zero temperature, i.e. when $\operatorname{Re}\Sigma \sim \omega$ and $\operatorname{Im}\Sigma \sim \omega^2$. As can be seen there are two major effects. First, all the peaks in energy distribution curves get broadened so that $\mathrm{FWHM} = \operatorname{Im}\Sigma$. The second effect can be seen in the shift of the peaks from their original positions given by $\operatorname{Re}\Sigma$. Therefore both parts of the self-energy can be given a physical interpretation. The imaginary part is causing the damping of the particle motion, which is related to the finite mean free path of the excitations or their energy and momentum uncertainty, while the real part gives the change of the excitation energy, and hence changing the particle dispersion from the bare to the renormalized one determines the particle effective mass. As the time representation of $\Sigma^{\mathrm{R}}(\mathbf{k},t)$ is a casual function $\operatorname{Re}\Sigma(\mathbf{k},\omega)$ and $\operatorname{Im}\Sigma(\mathbf{k},\omega)$ are not independent and are connected by the Kramers-Kronig relations:

$$\begin{aligned} \operatorname{Re}\Sigma(\mathbf{k},\omega) &= \frac{1}{\pi}\fint_{-\infty}^{+\infty}\frac{\operatorname{Im}\Sigma(\mathbf{k},x)}{x-\omega}\mathrm{d}x, \\ \operatorname{Im}\Sigma(\mathbf{k},\omega) &= -\frac{1}{\pi}\fint_{-\infty}^{+\infty}\frac{\operatorname{Re}\Sigma(\mathbf{k},x)}{x-\omega}\mathrm{d}x. \end{aligned} \tag{1.31}$$

---

is omitted the retarded self-energy is meant. There is a simple relation between the advanced and retarded self-energies: $\Sigma^{\mathrm{R}} = (\Sigma^{\mathrm{A}})^*$.

Checking for K-K consistency is sometimes a useful test for how strongly the experimentally measured photoelectron intensity deviates from being the spectral function. At certain cases it is also possible to extract the bare dispersion from the experimental data [41].[†]

To conclude, one needs to mention that the self-energy contains not only the electron-electron scattering effects, but also effects of coupling of the electronic system to all other degrees of freedom, like phonons [42], plasmons [43], magnetic excitations [44], as well as effects of scattering on impurities [45], and, therefore, turns out to be a central characteristic to be extracted from ARPES spectra.

1.7 Luttinger theorem

Usually the Fermi surface is introduced for the system of noninteracting fermions, where it separates the occupied and unoccupied single particle states in the momentum space at zero temperature. In this case there exists a useful relation between the volume embraced by the Fermi surface V_{FS} and the particle concentration N/V

$$\frac{N}{V} = 2\frac{V_{\mathrm{FS}}}{(2\pi)^3}, \text{ or } \quad \bar{n} = 2\frac{V_{\mathrm{FS}}}{V_{\mathrm{BZ}}}, \tag{1.32}$$

where n is the number of fermions (electrons) per unit cell, and V_{BZ} is the volume of the Brillouin zone for the case of particles in a periodic potential.

By analogy to the noninteracting case ($\mathrm{FS} = \{\mathbf{k} : \mathscr{E}_{\mathbf{k}}(0) = 0\}$), Luttinger extended the notion of the Fermi surface to the case of interacting particles, defining it as a set of $\mathbf{k}$ points at which the renormalized band dispersion is zero at the Fermi level [46]:

$$\mathrm{FS}^{\mathrm{int}} = \{\mathbf{k} : E_{\mathbf{k}}(0) \equiv \mathscr{E}_{\mathbf{k}}(0) + \mathrm{Re}\,\Sigma(\mathbf{k}, 0) = 0\}. \tag{1.33}$$

Assuming the validity of the perturbation theory two important consequences were drawn.

First, the extended Fermi surface is a rigorous object, as the momentum distribution of the particles

$$n_{\mathbf{k}} = \langle \hat{c}^{\dagger}_{\mathbf{k}} \hat{c}_{\mathbf{k}} \rangle = \int_{-\infty}^{+\infty} A(\mathbf{k}, \omega) f(\omega)\, \mathrm{d}\,\omega \tag{1.34}$$

[†] The use of the K-K in practice is addressed in more details in the appendix A.

develops a finite discontinuity $0 < Z \leqslant 1$ when traversing the FS.

Second, the volume of the Fermi surface is given by the same equation (1.32) as in the case of non-interacting particles, which provides a useful method of determining the charge concentration from the experimentally obtained data.

None the less, as the proof was based on the perturbation theory, and since perturbation expansions may not converge for certain interactions between the particles, the theorem could be violated.[†]

Later on it was shown that if the perturbation holds then the imaginary self-energy should behave like $\operatorname{Im}\Sigma(\mathbf{k},\omega) \sim \omega^2$ in the vicinity of Fermi level [48]. This is actually why the theorem is frequently associated with the Fermi liquid regime and is commonly believed to be violated in the case of underdoped cuprates ($x \lesssim 0.1$) [49, 50].

More definitive conclusions as for the validity of Luttinger theorem were obtained in [51], namely that the theorem should hold as long as there are no gaps in the excitation spectrum. There are also theoretical claims that even in the case of pronounced non-Fermi liquid or Mott insulator regime the Luttinger theorem can be still further extended [52, 53]. Here for the Fermi (Luttinger) surface one takes all the k-points where the real part of the Green's function changes sign, i.e both zeroes and infinities are considered, and the charge density is obtained as:

$$n_{\mathrm{k}} = \int\limits_{\operatorname{Re} G(\mathbf{k},0)>0} \frac{d\mathbf{k}}{(2\pi)^3}. \tag{1.35}$$

Obviously there are no peaks in $A(\mathbf{k},0)$ for the zeroes of the Green's function and experimental applicability of this formulation remains unclear. However for the doping range (0.15–0.3), which is in the scope of this study, the Luttinger theorem in formulation (1.33) seems to be well justified and the net deviation rarely reaches 3% [54, 55].

[†] There also exists non-perturbative proof for the case of normal Fermi liquid [47].

Chapter 2

Signatures of superconductivity in photoemission spectra

2.1 Introduction

In the previous chapter it was shown how the simple picture of non-interacting electrons can be extended to the case of a system with interacting particles, what information, and under which assumptions can be obtained using angle resolved photoemission spectroscopy. Those considerations are mainly of general character.

The aim of this chapter is to give an idea what additional particularities are brought into the photoemission spectrum with the onset of the superconductivity, and how they are related to the interaction that modifies the ground state of the system, turning it from the Fermi liquid, when the picture of electrons moving in an average potential is a good starting point, into the superconductor, a system with a ground state significantly different from the free electron approximation.

2.2 BCS superconductors and their spectral function

Although the nature of high temperature superconductivity remains unclear, there are enough reasons to believe that the mechanism of high temperature superconductivity involves Cooper pairing [6–8,56], though the interaction that leads to this phenomenon might not necessary be of the lattice origin. Therefore conventional BCS theory can be a good starting point to gain some basic understanding of what to expect from photoemission spectra of high-T_C compounds below the critical temperature, and how the pairing mechanism may manifest itself in the ARPES spectra.

The Hamiltonian given below can be considered as a rather general approximation to discuss the matter of superconductivity

$$\hat{H}^{\mathrm{MF}} = \sum_{\mathbf{k},\sigma} \xi_{\mathbf{k}} \hat{c}^{\dagger}_{\mathbf{k}\sigma} \hat{c}_{\mathbf{k}\sigma} + \sum_{\substack{\mathbf{q},\mathbf{k},\mathbf{k}' \\ \sigma,\sigma'}} V_{\mathbf{q},\mathbf{k},\mathbf{k}'} \hat{c}^{\dagger}_{\mathbf{k}'-\mathbf{q},\sigma'} \hat{c}_{\mathbf{k}',\sigma'} \hat{c}^{\dagger}_{\mathbf{k}+\mathbf{q},\sigma} \hat{c}_{\mathbf{k},\sigma}. \tag{2.1}$$

In the simplest approach, to account for the many-body interactions in the system, the $\hat{c}$-operators are not taken to create and annihilate true electrons, but rather correspond to Landau quasiparticles with effective dispersion $\xi_{\mathbf{k}}$ and effective two-particle interaction $V_{\mathbf{q},\mathbf{k},\mathbf{k}'}$. For the conventional superconductivity the minimal set of interactions to be included into the second term comprises of screened Coulomb repulsion and electron-electron interaction via the lattice vibrations [†]:

$$V_{\mathbf{q},\mathbf{k},\mathbf{k}'} = V^{\text{el-el}}_{\mathbf{q},\mathbf{k},\mathbf{k}'} + V^{\text{el-ph}}_{\mathbf{q},\mathbf{k},\mathbf{k}'} = \frac{4\pi e^2}{\mathbf{q}^2 \varepsilon(q)} + \frac{\hbar\omega_{\mathbf{k}} |M_{\mathbf{k}}|^2}{(\xi_{\mathbf{k}} - \xi_{\mathbf{k}'})^2 - (\hbar\omega_{\mathbf{k}})^2}. \tag{2.2}$$

One can easily see that for particular $\mathbf{k}$ and $\mathbf{k}'$ when $\xi_{\mathbf{k}} \cong \xi_{\mathbf{k}'}$ the term $V_{\mathbf{q},\mathbf{k},\mathbf{k}'}$ may become negative. Unlike the Sommerfeld-Bloch theory of individual particles, which neglects the correlation between different electrons, in the BCS theory [2, 59] this was taken into account and it was shown that properly filling the phase space with pairs of quasiparticles of opposite quasi-momenta $\mathbf{k}$ and spins σ one can arrive at a state with a lower energy, which clearly points that the Fermi sea with the state occupancy given simply by the Fermi-Dirac distribution is not a true ground state of the system.

One may try to incorporate the Cooper correlations into the 2N-particle wave function in the following way

$$|\Psi_{2N}\rangle = \sum_{\mathbf{k}_1} \dots \sum_{\mathbf{k}_N} g_{\mathbf{k}_1} \dots g_{\mathbf{k}_N} \hat{c}^{\dagger}_{\mathbf{k}_1,\uparrow} \hat{c}^{\dagger}_{-\mathbf{k}_1,\downarrow} \dots \hat{c}^{\dagger}_{\mathbf{k}_N,\uparrow} \hat{c}^{\dagger}_{-\mathbf{k}_N,\downarrow} |0\rangle, \tag{2.3}$$

which would guarantee the same occupancy of the states $|\mathbf{k},\uparrow\rangle$ and $|-\mathbf{k},\downarrow\rangle$. However, this function turns out to be too complicated for practical use, and in the BCS theory it was suggested to use a more general form

$$|\Psi^0_{\mathrm{BCS}}\rangle = \prod_{\mathbf{k}} (u_{\mathbf{k}} + v_{\mathbf{k}} \hat{c}^{\dagger}_{\mathbf{k},\uparrow} \hat{c}^{\dagger}_{-\mathbf{k},\downarrow}) |0\rangle, \tag{2.4}$$

[†] It is not clear if the phonons can mediate pairing in the case of high temperature superconductors, so other possibilities, like coupling to spin fluctuations were also suggested [57], though it is frequently argued that the mediator that couples electrons into Cooper pairs should necessary be of external origin to the electronic system (like the phonons in the case of conventional superconductivity). This conviction, however, should not be regarded as serious ground for arguments of the kind of "How could electrons pair themselves?" To realize the weakness of such an argument one can think of superfluid ^{3}He [58], where the coupling into pairs is accomplished without involving any external "mediator".

which unlike (2.3) is not characterized by a fixed particle number, thus the whole problem is treated using grand canonical ensemble. The BCS wave function is that complicated ground state which numerous perturbative approaches [3–5, 60] fail to describe correctly, and search after which took about 50 years since the first experimental observation of superconductivity by Kamerlingh Onnes [1] in 1911.

Considering only the pairs $|\mathbf{k},\uparrow\rangle$ and $|-\mathbf{k},\downarrow\rangle$ one can further reduce the Hamiltonian (2.1) to obtain

$$\hat{H}_{\text{BCS}} = \sum_{\mathbf{k},\sigma} \xi_{\mathbf{k}} \hat{c}^{\dagger}_{\mathbf{k}\sigma} \hat{c}_{\mathbf{k}\sigma} + \sum_{\mathbf{k},\mathbf{q}} \tilde{V}_{\mathbf{k},\mathbf{k}+\mathbf{q}}\, \hat{c}^{\dagger}_{-(\mathbf{k}+\mathbf{q}),\downarrow}\, \hat{c}_{-\mathbf{k},\downarrow}\, \hat{c}^{\dagger}_{\mathbf{k}+\mathbf{q},\uparrow}\, \hat{c}_{\mathbf{k},\uparrow}. \tag{2.5}$$

The original way to solve the problem was to minimize the system energy with respect to parameters $u_{\mathbf{k}}$ and $v_{\mathbf{k}}$, which results in a so-called gap equation

$$\begin{gathered} \Delta_{\mathbf{k}} = -\sum_{\mathbf{k}'} \tilde{V}_{\mathbf{k},\mathbf{k}'} \frac{\Delta_{\mathbf{k}'}}{2E_{\mathbf{k}'}}, \quad \text{where} \quad \Delta_{\mathbf{k}} \overset{\text{def}}{=} \sum_{\mathbf{k}'} \tilde{V}_{\mathbf{k},\mathbf{k}'} u_{\mathbf{k}'} v_{\mathbf{k}'} \text{ and} \\ |u_{\mathbf{k}}|^2 = \frac{1}{2}\left(1 + \frac{\xi_{\mathbf{k}}}{E_{\mathbf{k}}}\right), \quad |v_{\mathbf{k}}|^2 = \frac{1}{2}\left(1 - \frac{\xi_{\mathbf{k}}}{E_{\mathbf{k}}}\right), \quad E_{\mathbf{k}} = \sqrt{\xi_{\mathbf{k}}^2 + \Delta_{\mathbf{k}}^2}. \end{gathered} \tag{2.6}$$

Solution of the gap equation (2.6) provides the coefficients $u_{\mathbf{k}}$ and $v_{\mathbf{k}}$, which allows the ground state wave function $|\Psi^0_{\text{BCS}}\rangle$ to be written explicitly and the ground state energy calculated as $E_0 = \langle \Psi^0_{\text{BCS}} | \hat{H}_{\text{BCS}} | \Psi^0_{\text{BCS}} \rangle$.

For the spectroscopy, however, the possible excitation in the system are of principal interest. In the mean field approximation the BCS Hamiltonian can be diagonalized using Bogoliubov-Valatin transformations [61, 62]:

$$\begin{pmatrix} \hat{c}^{\dagger}_{\mathbf{k},\sigma} \\ \hat{c}_{-\mathbf{k},-\sigma} \end{pmatrix} = \begin{pmatrix} u_{\mathbf{k}} & \sigma v_{\mathbf{k}} \\ -\sigma v_{\mathbf{k}} & u_{\mathbf{k}} \end{pmatrix} \begin{pmatrix} \hat{\gamma}^{\dagger}_{\mathbf{k},\sigma} \\ \hat{\gamma}_{-\mathbf{k},-\sigma} \end{pmatrix}, \tag{2.7}$$

so that the diagonalized hamiltonian becomes

$$\hat{H}^{\text{MF}}_{\text{BCS}} = \sum_{\mathbf{k}} E_{\mathbf{k}} \left(\hat{\gamma}^{\dagger}_{\mathbf{k}\uparrow} \hat{\gamma}_{\mathbf{k}\uparrow} + \hat{\gamma}^{\dagger}_{\mathbf{k}\downarrow} \hat{\gamma}_{\mathbf{k}\downarrow} \right) + E_0, \tag{2.8}$$

where E_0 is the ground state energy and $E_{\mathbf{k}}$ is given by (2.6) and defines the dispersion of the excited states. For instance, the energy of some excited state $|\Psi_{E_n}\rangle = \hat{\gamma}^{\dagger}_{\mathbf{k}_1,\sigma_1} \ldots \hat{\gamma}^{\dagger}_{\mathbf{k}_N,\sigma_N} |\Psi^0_{\text{BCS}}\rangle$ would be $E_n = E_{\mathbf{k}_1} + \ldots + E_{\mathbf{k}_N} + E_0$. Thus it is easy to see that the removal of the quasielectron from the one-particle state $|\mathbf{k},\uparrow\rangle$ results in the mixed excited state of the remaining system: $\hat{c}_{\mathbf{k},\uparrow} |\Psi_{E_n}\rangle = v_{\mathbf{k}} \hat{\gamma}^{\dagger}_{\mathbf{k},\uparrow} |\Psi_{E_n}\rangle + u_{\mathbf{k}} \hat{\gamma}_{-\mathbf{k},\downarrow} |\Psi_{E_n}\rangle$[†],

---

[†] Note that for $T = 0$ the second term vanishes, since $\hat{\gamma}_{\mathbf{k},\uparrow}|\Psi\rangle = \hat{\gamma}_{\mathbf{k},\uparrow}|\Psi^0_{\text{BCS}}\rangle = 0$ as there are no excited states to be annihilated by the operator $\hat{\gamma}_{\mathbf{k},\uparrow}$. That is, only the excitations that are increasing the system energy by $E_{\mathbf{k}}$ are possible, which means that only the states with positive binding energy are visible in photoemission.

which means that after such an excitation the system energy will be either increased or decreased by the amount $E_{\mathbf{k}}$, signifying two types of excitations in the superconducting state. The spectral function in the superconducting state can be calculated using expression (1.18)

$$A_{\mathbf{k},\sigma}(\omega) = \frac{2\pi}{Z}\sum_{n,m} e^{-\frac{E_n}{kT}}(1+e^{-\frac{\omega}{kT}})\left|\langle\Psi_{E_m}|u_{\mathbf{k}}\hat{\gamma}^{\dagger}_{\mathbf{k},\sigma} + v_{\mathbf{k}}\hat{\gamma}_{-\mathbf{k},-\sigma}|\Psi_{E_n}\rangle\right|^2 \delta(E_n - E_m + \omega). \tag{2.9}$$

Out of all possible excited eigenstates over which runs the summation in 2.9, non-zero terms will appear only for those pairs $|\Psi_{E_m}\rangle$, $|\Psi_{E_n}\rangle$ that have the same set of excited Bogoliubov quasiparticles, except for one additional or one missing excitation in the state $|\Psi_{E_m}\rangle$ as compared to the state $|\Psi_{E_n}\rangle$, when either operator $u_{\mathbf{k}}\hat{\gamma}^{\dagger}_{\mathbf{k},\sigma}$ or operator $v_{\mathbf{k}}\hat{\gamma}_{-\mathbf{k},-\sigma}$ gives a non-vanishing matrix element. Owing to this property the sum (2.9) can be split into two:

$$\begin{aligned} A_{\mathbf{k},\sigma}(\omega) =& A^{u}_{\mathbf{k},\sigma}(\omega) + A^{v}_{\mathbf{k},\sigma}(\omega) \\ =& \frac{2\pi}{Z}\sum_{n,m} e^{-\frac{E_n}{kT}}(1+e^{-\frac{\omega}{kT}})\left|\langle\Psi_{E_m}|u_{\mathbf{k}}\hat{\gamma}^{\dagger}_{\mathbf{k},\sigma}|\Psi_{E_n}\rangle\right|^2 \delta(E_n - E_m + \omega) \\ &+ \frac{2\pi}{Z}\sum_{n,m} e^{-\frac{E_n}{kT}}(1+e^{-\frac{\omega}{kT}})\left|\langle\Psi_{E_m}|v_{\mathbf{k}}\hat{\gamma}_{-\mathbf{k},-\sigma}|\Psi_{E_n}\rangle\right|^2 \delta(E_n - E_m + \omega). \end{aligned} \tag{2.10}$$

For the term $A^{u}_{\mathbf{k},\sigma}(\omega)$ non-zero matrix elements are appearing only when the state $|\Psi_{E_n}\rangle = \hat{\gamma}^{\dagger}_{\mathbf{k_p},\sigma_P}...\hat{\gamma}^{\dagger}_{\mathbf{k}_1,\sigma_1}|\Psi^0_{\mathrm{BCS}}\rangle$ does not contain the excitation $\hat{\gamma}^{\dagger}_{\mathbf{k},\sigma}$, while the state $|\Psi_{E_m}\rangle$, in addition to the same set of excitations has the one created by $\hat{\gamma}^{\dagger}_{\mathbf{k},\sigma}$: $|\Psi_{E_m}\rangle = \hat{\gamma}^{\dagger}_{\mathbf{k},\sigma}\hat{\gamma}^{\dagger}_{\mathbf{k_p},\sigma_P}...\hat{\gamma}^{\dagger}_{\mathbf{k}_1,\sigma_1}|\Psi^0_{\mathrm{BCS}}\rangle$. Therefore the first summand in (2.10) can be reduced to

$$\begin{aligned} A^{u}_{\mathbf{k},\sigma}(\omega) &= \frac{2\pi}{Z}\sum_{n} e^{-\frac{E_n}{kT}}(1+e^{-\frac{E_{\mathbf{k}}}{kT}})\left|u_{\mathbf{k}}\right|^2 \delta(\omega - E_{\mathbf{k}}), \text{ with} \\ Z &= \sum_{n} e^{-\frac{E_n+E_{\mathbf{k}}}{kT}} + \sum_{n} e^{-\frac{E_n}{kT}} = \sum_{n}(1+e^{-\frac{E_{\mathbf{k}}}{kT}})e^{-\frac{E_n}{kT}}, \end{aligned} \tag{2.11}$$

and the sums running over all possible excited states that do not contain the excitation $\hat{\gamma}^{\dagger}_{\mathbf{k},\sigma}$. Similarly the term $A^{v}_{\mathbf{k}\sigma}(\omega)$ can be calculated to give the total spectral function

$$A(\mathbf{k},\omega) = 2\pi[u^2_{\mathbf{k}}\delta(\omega - E_{\mathbf{k}}) + v^2_{\mathbf{k}}\delta(\omega + E_{\mathbf{k}})]. \tag{2.12}$$

The function (2.12) is plotted in Fig. 2.1(a) with appropriate “broadening” of the delta functions. As can be seen there are no excitations possible at the energy

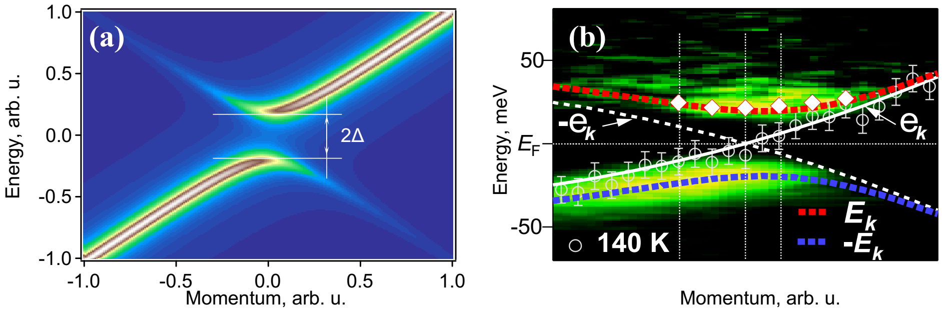

Figure 2.1: (a) BCS spectral function as given in eq. (2.12). Each delta function has been broadened along the energy axis using a Lorentzian of a fixed width. (b) Experimentally observed BCS-like dispersion, Matsui et al. [64].

range $\pm\Delta_{\mathbf{k}}$ around the chemical potential. Choosing the HTSC with reasonably high critical temperature Matsui et al. [see Fig. 2.1(b)] have shown the experimentally observed intensity to be in good agreement with the formulae (2.12). One can easily realise that the ARPES experiment allows one not only to measure the value of the superconducting gap, but also test its dependence on momentum **k**, i.e. the gap symmetry. From the gap equations (2.6) it is clear that the gap symmetry is closely related with the symmetry of the pairing potential [63].

For the conventional superconductors the pairing potential $\tilde{V}_{\mathbf{k},\mathbf{k}'}$ is spherically symmetric and so is the symmetry of the solution $\Delta_{\mathbf{k}}$. For the high temperature superconductors the superconducting gap is believed to have the d-wave symmetry, thus imposing certain limitations on the $\tilde{V}_{\mathbf{k},\mathbf{k}'}$.

2.3 Self-energy effects due to coupling to a collective mode

Actually, the number of experimental observables reflecting the properties of the pairing potential can be extended beyond the gap value and its symmetry, if one recalls the quasi-particle life-time effects, which were completely left without attention in the previous section.

Using perturbation theory in the normal state, Engelsberg and Schrieffer [42] demonstrated that there are notable effects in the electronic self-energy when electrons are coupled to a sharp bosonic mode characterised by frequency Ω. In the original work coupling to the Einstein phonon was discussed, however the considerations can be equally applied to the spin resonance mode [65–67], which is

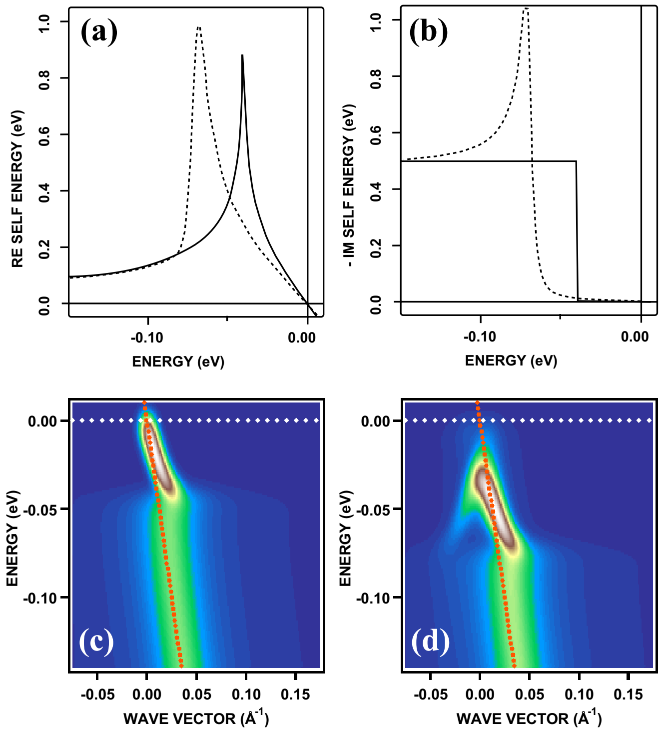

Figure 2.2: Real (a) and imaginary (b) part of the self-energy when coupled to single bosonic mode. The normal and superconducting states are shown with solid and dashed lines respectively. Mode energy and the gap value were set to $\Omega = 40\,\text{meV}$ and $\Delta = 30\,\text{meV}$. (c), (d) corresponding spectral function for the superconducting and normal state multiplied by the Fermi function and convoluted with experimental resolution. Data after Fink et al. [68].

believed to be an alternative explanation to the renormalization effects that are to be introduced here. Detailed description of the experimentally observed effects, as well as *pro* and *contra* for their phononic and magnetic origin are postponed to the following chapters, while here the basic mechanism for their appearance in the spectra is taken to the focus.

Modeling the collective mode as an undamped oscillator with the propagator given by $D(\mathbf{k},\omega) = \frac{1}{\omega^2-\Omega^2+i\delta}$ the electronic self-energy can be approximated by

$$\begin{aligned}\Sigma(\mathbf{k},\omega) &= ig^2 \int\!\!\int \frac{\mathrm{d}\mathbf{k}'\,\mathrm{d}\omega'}{(2\pi)^4} D(\mathbf{k}-\mathbf{k}',\omega-\omega')G^0(\mathbf{k}',\omega') \\ &= ig^2 \int\!\!\int \frac{\mathrm{d}\mathbf{k}'\,\mathrm{d}\omega'}{(2\pi)^4} \frac{1}{(\omega-\omega')^2-\Omega^2+\mathrm{i}\delta}\,\frac{1}{\omega'-\xi_{\mathbf{k}'}-\Sigma(\mathbf{k}',\omega')},\end{aligned} \tag{2.13}$$

where the coupling constant g is taken to be momentum and energy independent, and the $G^0(\mathbf{k},\omega)$ is the Green's function of the uncoupled electronic system. Assuming constant density of states, expressions for the self-energy at T=0 can be obtained

$$\begin{aligned}\operatorname{Im}\Sigma(\omega) &= \frac{-g^2N\pi}{2\Omega}\,\theta(|\omega|-\Omega), \\ \operatorname{Re}\Sigma(\omega) &= \frac{-g^2N}{2\Omega}\ln\left|\frac{\omega+\Omega}{\omega-\Omega}\right|.\end{aligned} \tag{2.14}$$

As can be seen there is an onset of the scattering rate in the imaginary part of the self-energy at $|\omega| > \Omega$ and a corresponding logarithmic divergence in the real part. In reality the mode must have a finite width so that the singularities in the self-energy are effectively removed. For the moderate coupling strength the self-energy (2.14) leads to appearance of the so-called "kink" in the band dispersion as shown in the Fig. 2.2 at energy equal to the mode energy Ω, which was indeed detected experimentally in photoemission spectra of some cuprates [69–72].

In the superconducting state appropriate Green's function for the superconducting state is to be substituted into (2.13). In agreement with [73], it is easy to see from (2.12) that

$$G^0_{\mathrm{SC}}(\mathbf{k},\omega) = \frac{u^2_{\mathbf{k}}}{\omega - E_{\mathbf{k}}} + \frac{v^2_{\mathbf{k}}}{\omega + E_{\mathbf{k}}} = \frac{\omega + \xi_{\mathbf{k}}}{\omega^2 - \xi^2_{\mathbf{k}} - \Delta^2_{\mathbf{k}}}, \tag{2.15}$$

which according to [68] yields for $\omega < 0$

$$\operatorname{Im}\Sigma(\omega) = \frac{-g^2 N\pi}{2\Omega} \operatorname{Re} \frac{\omega + \Omega}{\sqrt{(\omega+\Omega)^2 - \Delta^2}}. \tag{2.16}$$

The corresponding self-energy is plotted with a dashed line in Fig. 2.2(a,b) and the spectral function is given in panel (d). The major difference from the normal state is the appearance of the superconducting gap and the shift of the scattering onset and the "kink" position from $\omega = -\Omega$ to $\omega = -(\Omega + \Delta)$.

Additional corrections to the self-energy can be obtained when taking into account the momentum dependence of the coupling. It is known that for coupling to the magnetic resonance mode, the propagator $D(\mathbf{k},\omega)$ is strongly peaked at the antiferromagnetic vector $Q = (\pi,\pi)$, this in turn requires one to take into account all the details of the electronic structure. As shown by Eschrig and Norman in Refs. [57, 74] it should lead to a strong momentum dependence of the renormalization. The strongest effects are expected to be observed in the vicinity of the antinodal points, while along the nodal direction the sharp features in the self-energy appear due to the finite momentum width of the resonance peak.

Chapter 3

Experimental aspects of ARPES

This chapter is devoted to the experimental aspects of photoemission, that is sample preparation and characterization. It includes a description of the experimental setup. Basic issues of data treatment are addressed, such as setting the energy and momentum scales in the raw data, spectrum intensity normalization, construction of the Fermi surface maps and doping determination, and its accuracy.

3.1 Sample preparation

In this work specimens of two different cuprate families were studied — $Bi_2Sr_2CaCu_2O_{8+\delta}$ and $YBa_2Cu_3O_{7-\delta}$. Pure $Bi_2Sr_2CaCu_2O_{8+\delta}$ and Zn-substituted $Bi_2Sr_2Ca(Cu_{1-x}Zn_x)_2O_{8+\delta}$ ($x = 0.01$) samples were grown in the group of Prof. B. Keimer (MPI-FKF, Stuttgart). $Bi_2Sr_2Ca(Cu_{1-x}Ni_x)_2O_{8+\delta}$ with nominal Ni concentration of 2% were provided by A. Erb (WMI, Garching). Bi-2212 samples were grown by the self-flux method [75]. As the aim was to study the effects of impurities, it was decided to use Pb-free samples in order to minimize possible side effects of lead atoms.

Since the ARPES technique requires atomically clean surfaces, the usual way to prepare such a surface is to cleave the crystal *in situ* in the ultrahigh vacuum chamber (P$\sim 5 \cdot 10^{-11}$ mBar). In a view of weak van der Waals coupling between Bi layers, Bi-2212 is the most suitable crystal for this procedure. After being glued to the sample-holder using conducting silver epoxy as shown in Fig. 3.1(a). the crystal can be easily cleaved with a stripe of sticking tape attached to its free surface, resulting in a mirror-like surface. The lower image in panel (a) shows typical LEED

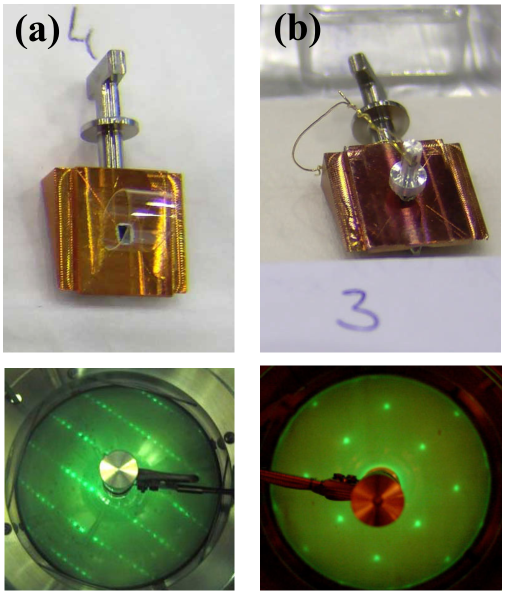

Figure 3.1: Sample cleaving methods and typical LEED pictures recorded from the cleaved surfaces. (a) $Bi_2Sr_2CaCu_2O_{8+\delta}$ samples are cleaved with a stripe of a sticky tape, (b) $YBa_2Cu_3O_{7-\delta}$ sample that requires aluminum top-post to be glued on the top.

picture for Pb-free samples. The set of parallel dots are due to a known incommensurate 4.76:1 surface modulation [76–79].

$YBa_2Cu_3O_{7-\delta}$ high-quality single crystals were synthesized using solution-growth method. To obtain the optimally doped samples with nominal oxygen concentration $\delta = 0.15$ the samples were annealed in O_2 at 520 °C. Underdoping was achieved by annealing in the air at $T = 590\,^\circ\mathrm{C}$ [80]. To untwin the samples, they were subjected to a uniaxial mechanical stress at elevated temperatures as described in [81, 82].

As the Y-123 samples are harder, they require a different cleavage procedure. Instead of a loop of a sticky tape an aluminum top-post can be glued to the sample as shown in Fig. 3.1b. After transferring the sample into the preparation chamber the top-post is kicked off with a screwdriver, resulting in an optically flat surface. A LEED picture, taken to control the surface quality demonstrates a well defined reflexes with no signs of reconstruction. Unlike Bi-2212, Y-123 samples do not have the natural cleavage plane. The details concerning this issue will be discussed in the corresponding chapter.

3.2 Light source

The advance of photoemission technique to a great extent should be attributed to the availability of high quality light sources. Among the requirements to a light

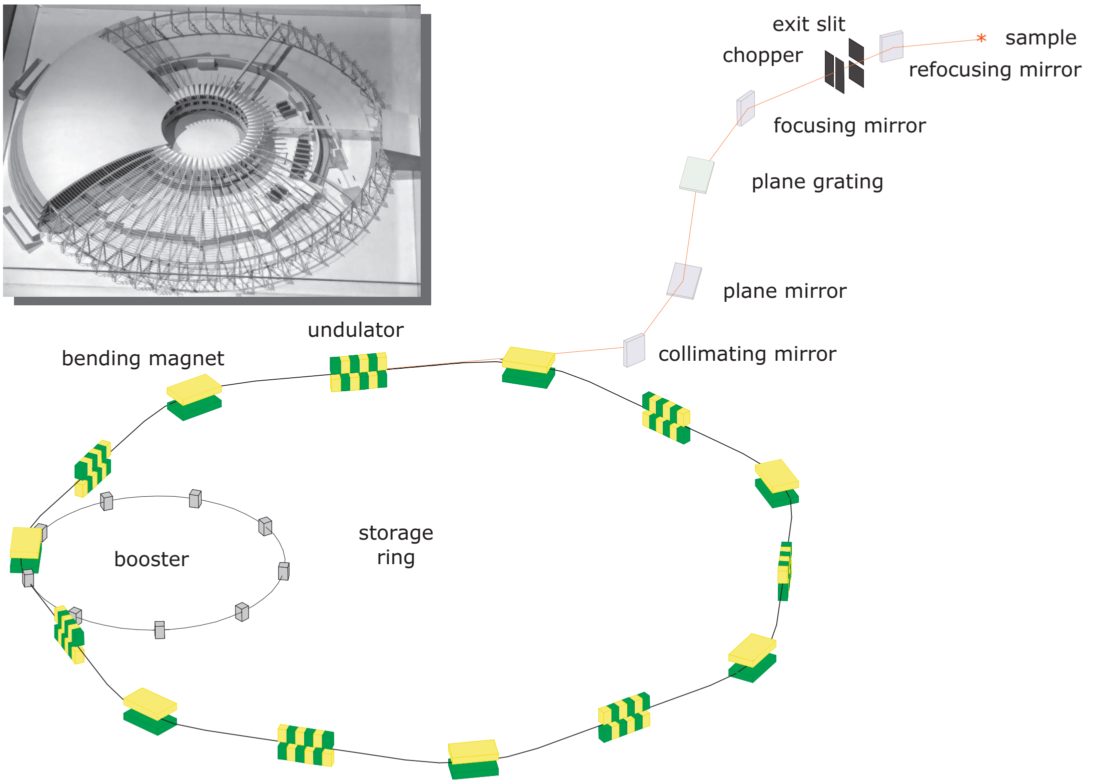

Figure 3.2: Schematics of a synchrotron. High energy electrons are traveling along the closed orbit in the storage ring. Passing trough each bending magnet and undulator electrons experience acceleration and emit light. The light beam after monochromatization and focusing is being delivered to the experiment.

source are high brightness, extended range of energies, high resolution, possibility to set a desired light polarization and small beam spot. With the development of the 3rd generation synchrotron facilities [†] and the build-on-purpose beamlines it became possible to satisfy all the mentioned conditions.

The basic principle of a synchrotron light source is based on the fact that high energy charged particles (in practice electrons are most frequently used), when subjected to large accelerations normal to their velocity emit electromagnetic radiation in the energy spectrum reaching the X-rays [83, 84]. The schematic design of a modern synchrotron is given in fig. 3.2. After acceleration in the Linear accelerator and booster to energy of several GeV the electron beam is injected into the storage ring. The closed orbit is achieved owing to a set of bending magnets, and the energy losses at each revolution are compensated by the radio frequency cavity. To obtain an extremely bright monochromatic source of light the electrons are led through

---

[†] 3rd generation refers to the facilities originally designed as the light sources, where the rings were built with insertion devices and all the magnetic structures designed to increase the photon yield.

	SLS SIS X9L	BESSY UE112PGM3	BESSY UE112LowE(b)
Energy range			
linear horizontal	10–800 eV	15–600 eV	5–250 eV
linear vertical	100–800 eV	—	—
circular	50–800 eV	—	in project
Beam spot size	$50\times100\mu$m	—	slitsize$\times100\mu$m
Monochromator type	PGM	PGM	PGM
Resolving power $E/\Delta E$	10^4	10^4	$> 10^5$
Undulator	UE212	UE112	UE112

Table 3.1: Beamline parameters

the undulator, a special device with a periodic pattern of a magnetic field. The parameters of the undulator (unlike wiggler similar in construction) are tuned in such a way that electrons are emitting radiation mainly on the fundamental mode of the undulator. Due to the relativistic effects the directional radiation pattern of the electron dipole radiation becomes extremely peaked in the forward direction. Additional narrowing arises from the interference of the radiation emitted at each wiggle, further increasing the brightness. Generally the undulators are constructed in the way that electrons are experiencing accelerations in the horizontal plane moving in the field of a precisely adjusted array of permanent magnets, in this case the light emitted along the undulator axis is strictly horizontally polarized, while the periphery of the light beam is elliptically polarized. To obtain circular polarized light special elliptical undulators can be used [85].

The data for this work was collected at two synchrotrons: at Berliner Elektronenspeicherring-Gesellschaft für Synchrotronstrahlung m.b.H. (BESSY), beamline UE125-PGM and UE112-LowE and at Swiss Light Source (SLS), beamline SIS-9L.

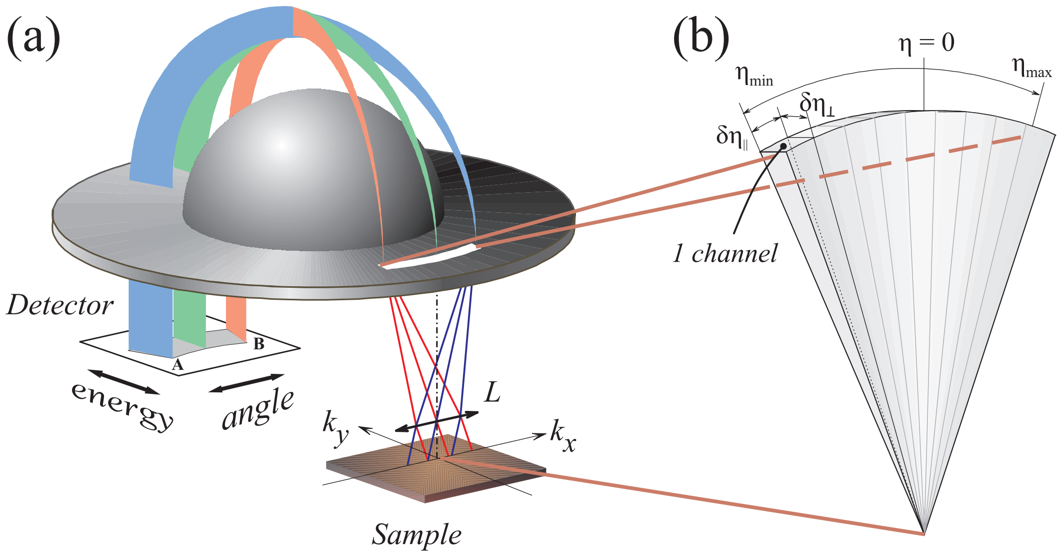

Figure 3.3: (a) Principle of the angular mode in a spherical electron energy analyser. (b) Solid angle from which electrons are being analyzed and main parameters that characterize the angular mode: angular resolution perpendicular to the slit $\delta\eta_{\perp}$, the acceptance angle $\eta_{\text{acc}} = \eta_{\max} - \eta_{\min}$, and the angular resolution along the slit $\delta\eta_{\|}$.

3.3 SCIENTA energy analyser

In the early ARPES studies the angular resolution was achieved via a small acceptance angle of the electron energy analyser, i.e. the device was constructed in a way to collect only the electrons, whose velocities lie within a cone of small aperture of 0.5 – 10°; the aperture determining the angular resolution of the instrument. Therefore at one time instance the spectrum corresponding to one particular direction of photoelectrons could be measured, while all the other electrons were simply wasted (Fig. 1.1). The great advantage in terms of efficiency was achieved after introduction of the angle resolved mode in hemispherical analyser. Fig. 3.3(a) illustrates the principal idea. Placing an electro-optical lens in front of the analyser entrance slit, with the latter being in the focal plane of the lens, would focus parallel electron beams at different parts of the entrance slit, so that finally, after passing through the electric field between the hemispheres † the electrons will be separated according to their angle and kinetic energy, forming a 2D image on the detector. Along one direction, the angle η at which electrons enter the analyser is being resolved, and along the perpendicular one, the photoelectrons are being distributed according to their kinetic energy. Of all possible directions the entrance slit cuts out a fan-like solid angle shown in Fig. 3.3(b). Unavoidable imperfections of the electro-optic

---

† The outer hemisphere in Fig. 3.3 is not shown.

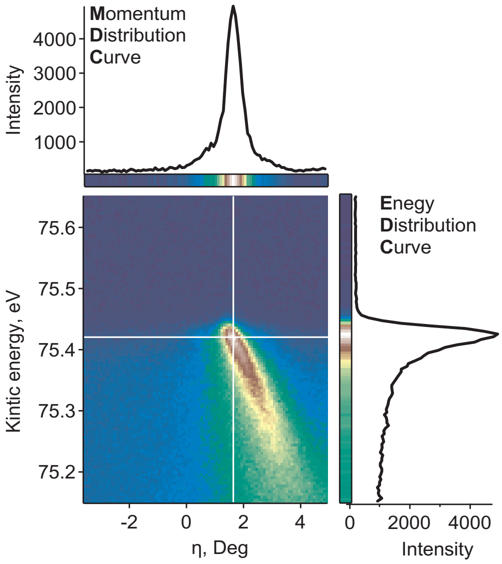

Figure 3.4: Energy-momentum distribution of photo-intensity. Colour denotes the intensity of photocurrent as a function of energy and momentum $I = I(E_{\mathrm{kin}}, \eta)$. In a view of direct relations 3.1-3.2, the angle η can be identified with momentum. Taking a row at fixed energy E_0 out from the 2D data matrix results in a curve referred to as a Momentum Distribution Curve: $\mathrm{MDC}_{E_0}(\eta) = I(E_0, \eta)$. By analogy, the column at fixed angle η_0, i.e. momentum, is called Energy Distribution Curve: $\mathrm{EDC}_{\eta_0}(E_{\mathrm{kin}}) = I(E_{\mathrm{kin}}, \eta_0)$.

system limit the angular resolution, hence the fan-like solid angle can formally be split into segments, within which the electrons are considered as contributing to a separate independent angular channel. The size of such segment defines the angular resolution perpendicular to the slit $\delta\eta_{\perp}$, and along the slit $\delta\eta_{\parallel}$. The total span in angle η is termed as acceptance angle $\eta_{\mathrm{acc}} = \eta_{\max} - \eta_{\min}$.

The detection system predetermines the convenient data representation. Sometimes each independent angular spectrum is shown as a separate curve in a waterfall graph similar to the one given in Fig. 1.7. However, the 2D colour-maps, where the colour encodes the intensity as a function of energy and angle/momentum are more convenient for data representation (see Fig. 3.4).

Momentum scale. For the mutual arrangement of the sample and analyser, as shown in Fig. 3.3, the projections of the photoelectron momentum and corresponding resolutions are given by simple formulae [†]:

$$k_x = |\mathbf{k}|\sin(\eta), \quad \delta k_x \approx |\mathbf{k}|\delta\eta_{\parallel}, \tag{3.1}$$

$$k_y = 0, \qquad \delta k_y \approx |\mathbf{k}|\delta\eta_{\perp}, \quad \text{where } |\mathbf{k}| = \frac{\sqrt{2mE_{\mathrm{kin}}}}{\hbar}. \tag{3.2}$$

Therefore, at higher photon energy one has a wider overview in the reciprocal space, but the price for this is a worse momentum resolution. For a narrow energy window $\Delta E = E_{\max} - E_{\min}$ one can neglect the dependence of $|\mathbf{k}|$ on energy and use the same scale calculated for the average energy in the image

---

[†] Setting the momentum scale for the arbitrary sample orientation will be explained in next subchapter.

Figure 3.5: The image before and after normalization. The red curve shows the MDC's, integrated within the energy window denoted by the white rectangles. For the detector with uniform sensitivity such MDC's are expected to be flat lines, if not, this is achieved through the normalization procedure.

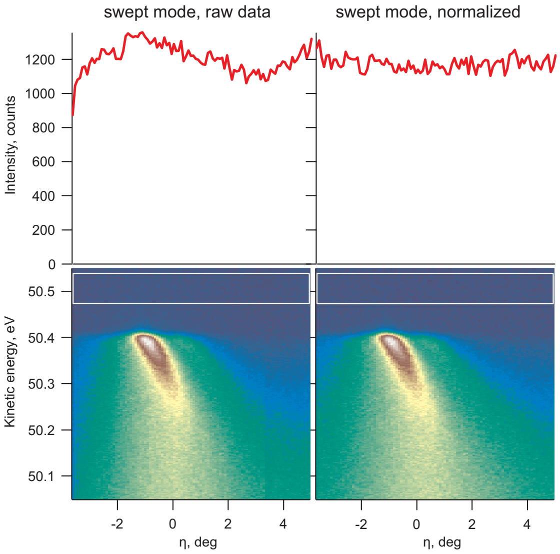

$E_{\mathrm{avg}} = (E_{\max} - E_{\min})/2$. The error introduced by this approximation can be estimated as $\delta\eta \approx \eta_{\mathrm{acc}}(\sqrt{E_{\mathrm{avg}} + \Delta E/2} - \sqrt{E_{\mathrm{avg}}})/\sqrt{E_{\mathrm{avg}}} \approx \eta_{\mathrm{acc}}\Delta E/8E_{\mathrm{avg}}$. For the spectrum shown in Fig. 3.5 this would yield an error of about 0.01°, which is much less than the angular resolution. Nevertheless, for the spectra with a wide energy window, or those measured at low kinetic energies, a separate scale must be set for each MDC.

Normalization. To eliminate possible effects of inhomogeneous detector sensitivity the spectra are to be measured in a swept mode. While this equalizes the sensitivity within each EDC, the sensitivity along the angular scale may still vary, distorting the form of MDC curves. To correct for this, one can normalize the spectrum to the non-zero spectral weight present above the Fermi level. This spectral weight is due to the higher harmonics in the spectrum of synchrotron light and corresponds to the states with high binding energy that already have no angular dependence. Thus the normalized spectrum is found as:

$$\begin{aligned} I_{\mathrm{Norm}}(E_{\mathrm{kin}},\eta) &= I_{\mathrm{Raw}}(E_{\mathrm{kin}},\eta)/\,\mathrm{Norma}(\eta), \text{ where} \\ \mathrm{Norma}(\eta) &= \int_{E_1}^{E_2} I_{\mathrm{Raw}}(E_{\mathrm{kin}},\eta)\,\mathrm{d}\,E_{\mathrm{kin}}, \end{aligned} \tag{3.3}$$

where $[E_1, E_2]$ is a small energy window as shown in figure 3.5. by a white rectangle.

Setting the energy scale. The SCIENTA analyser is equipped with a set of straight and curved entrance slits, which makes one flexible with the resolution and sensitivity of the instrument. Depending on the form of the entrance slit the image

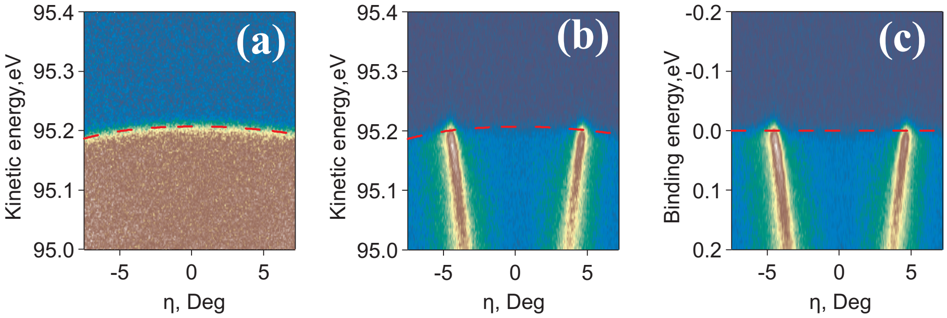

Figure 3.6: Illustration to the energy calibration of energy-momentum distribution measured with a straight analyser slit. (a) Fermi step, (b) raw data, (c) slit-corrected image.

of the Fermi edge measured from the silver or gold sample would be approximately straight or curved. To obtain accurate energy scale the spectra must be corrected for the Fermi edge (slit image) curvature using silver/gold spectrum measured with the same instrument settings (entrance slit, pass energy, beamline settings). The procedure is illustrated in Fig. 3.6. First, each EDC comprising the silver spectrum is fitted with a generalized Fermi Step $(1 + a(E_{\text{kin}} - E_{\text{F}}))/\left(1 + \exp\left(\frac{E_{\text{kin}} - E_{\text{F}}}{T}\right)\right) + C$ to obtain the FL position E_{F} for each angular channel.[†] The result is shown by the red dashed line in Fig. 3.6(a). The obtained from fitting dependence $E_{\text{F}}(\eta)$ is later used to set the binding energy scale: $E^{\text{corr}}_{\text{bind}}(\eta) = E_{\text{F}}(\eta) - E_{\text{kin}}(\eta)$; or to leave the energy scale in kinetic energies, but remove the slit curvature: $E^{\text{corr}}_{\text{kin}}(\eta) = E_{\text{kin}}(\eta) - E_{\text{F}}(\eta) + \langle E_{\text{F}} \rangle$, where $\langle E_{\text{F}} \rangle$ is the average value of $E_{\text{F}}(\eta)$. The correction procedure is illustrated in the Fig. 3.6.

3.4 Experimental geometry and FS mapping technique

The experimental geometry, i.e. the mutual position of the analyser (entrance slit *AB*), the incident light beam **q**, and the sample position, is shown in figure 3.7 (a-b). To demonstrate how changing the sample orientation one can probe different cuts in the energy-momentum space, the sample in the 'Top view' has been rotated around the y_0 axis by a finite angle φ. As can be seen from the drawing, for the case $\varphi = 0$ the k_x projection is also zero, while for the rotated position $k_x = -|\mathbf{k}| \cos \varphi$. In both cases the k_y projection is determined by the analyser angle η. In panel (d)

[†] Here C and α are additional fitting parameters that are introduced to account for the background intensity in the unoccupied part of the spectrum and the slope in the occupied one.

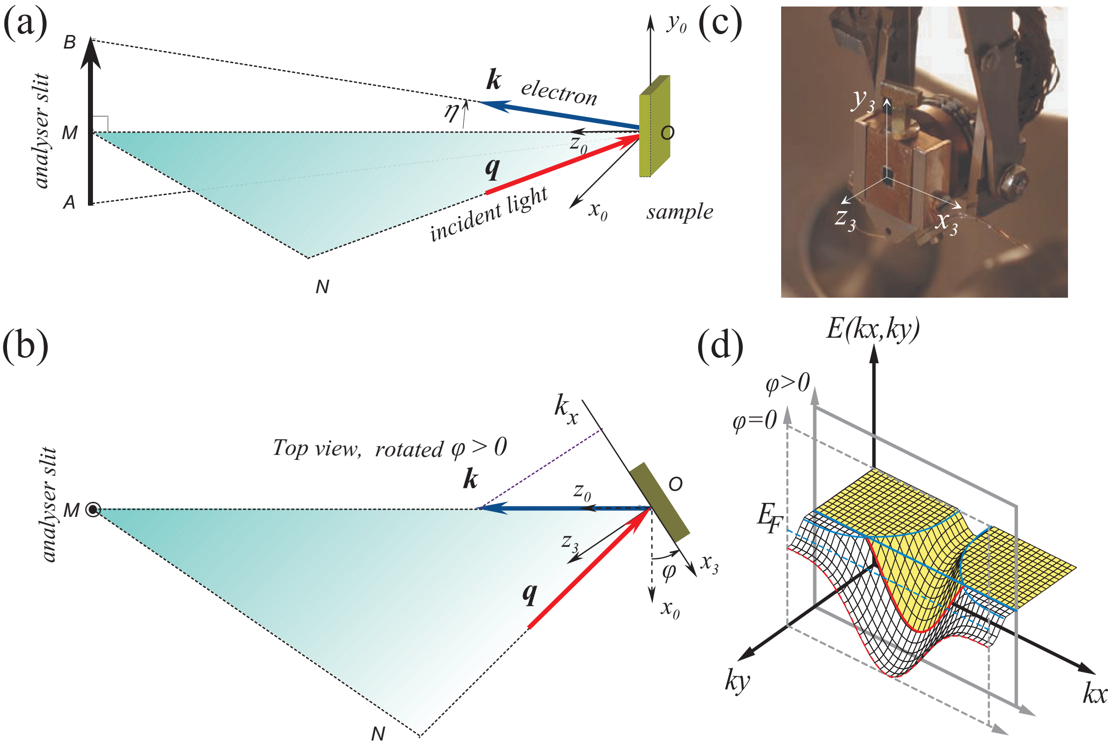

Figure 3.7: (a-b) Experimental geometry. The light beam always remains in the horizontal plane MON, with angle $\angle NOM = 45°$. Segment AB corresponds to the analyser entrance slit which is vertical, so that the analyser collects only those electrons, whose momenta are in plane ABO, hence the momentum direction is fully defined by the angle η. (c) Pocket of the manipulation with a sample holder mounted in. The black square in the middle is the sample. (d) The cartoon of the electronic structure with the white rectangles showing the cuts in energy-momentum space that is projected on the detector.

the grey rectangle shows the part of energy momentum space that are projected on the analyser for these two positions.

It is obvious that high precision mechanical manipulation of the sample is necessary for accessing different parts of the reciprocal space. In this study IFW-4 cryo-manipulator has been used, the rotatable head of which is shown in Figs. 3.7(c) and 3.8. The manipulator allows for the sample rotation around 3 independent axes with angle reproducibility better than 0.2°. Any sample orientation can be represented as three consecutive rotations: polar rotation by angle φ, tilt rotation by angle α, and azimuthal rotation by angle θ. The task is to find the projections of the electron momentum on the sample surface, as this would be the parallel component of quasi-momentum for the state from which the electron has been excited. The simplest way to do this is to introduce 4 systems of coordinates as shown in Fig. 3.8. The coordinates of the electron momentum $\mathbf{k}$ in the laboratory coordinate system (denoted by subscript '0') depend only on the SCIENTA angle η:

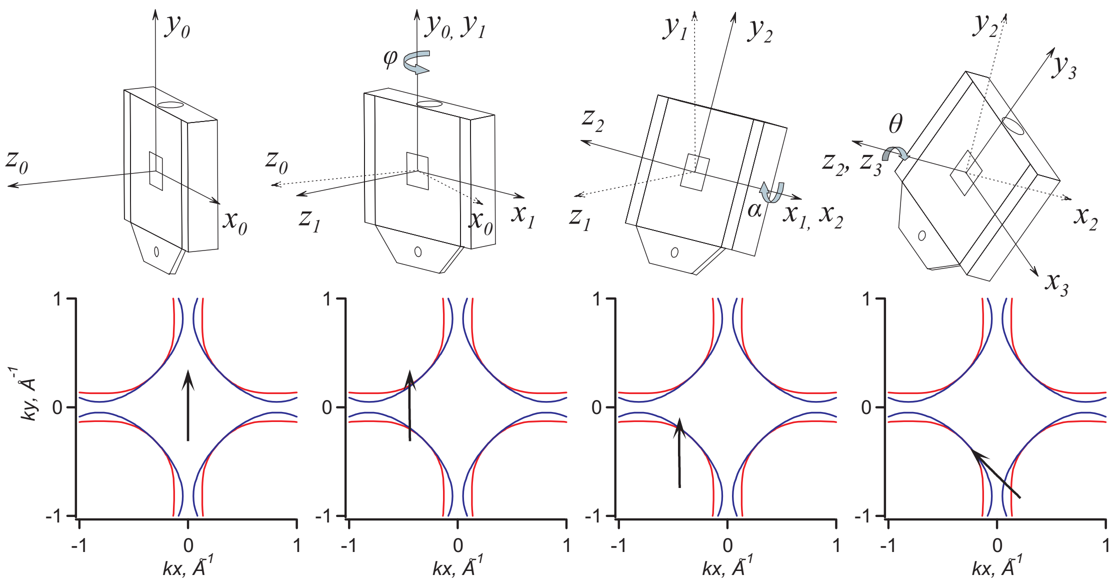

Figure 3.8: The three rotational degrees of freedom of IFW-4 manipulator. The series of pictures shows the three sequential rotations: polar, tilt and azimuthal.

$\mathbf{k} = |\mathbf{k}|(0, \sin\eta, \cos\eta)_0^{\mathrm{T}}$. Making sequential translation of coordinates from the laboratory system of coordinates to Ox_3, y_3, z_3, which is bound to the sample surface, one can find the projections $(x_3, y_3, z_3)^{\mathrm{T}}$ of the electron momentum $\mathbf{k}$ on the sample surface:

$$\begin{pmatrix} x_3 \\ y_3 \\ z_3 \end{pmatrix} = \begin{pmatrix} \cos\theta & -\sin\theta & 0 \\ \sin\theta & \cos\theta & 0 \\ 0 & 0 & 1 \end{pmatrix} \begin{pmatrix} x_2 \\ y_2 \\ z_2 \end{pmatrix};$$

$$\begin{pmatrix} x_2 \\ y_2 \\ z_2 \end{pmatrix} = \begin{pmatrix} 1 & 0 & 0 \\ 0 & \cos\alpha & -\sin\alpha \\ 0 & \sin\alpha & \cos\alpha \end{pmatrix} \begin{pmatrix} x_1 \\ y_1 \\ z_1 \end{pmatrix};$$

$$\begin{pmatrix} x_1 \\ y_1 \\ z_1 \end{pmatrix} = \begin{pmatrix} \cos\varphi & 0 & -\sin\varphi \\ 0 & 1 & 0 \\ \sin\varphi & 0 & \cos\varphi \end{pmatrix} \begin{pmatrix} 0 \\ |\mathbf{k}|\sin\eta \\ |\mathbf{k}|\cos\eta \end{pmatrix}. \qquad (3.4)$$

From Fig. 3.7 it is easy to see that changing the manipulator polar angle in small increments and taking the spectrum at each step one can make a detailed map of the whole band structure. The necessary motion can be programmed into computer, so that for the resulting spectrum one obtains data sets giving the photo-intensity as a function of kinetic energy E_{kin}, SCIENTA angle η and the scanned manipulator

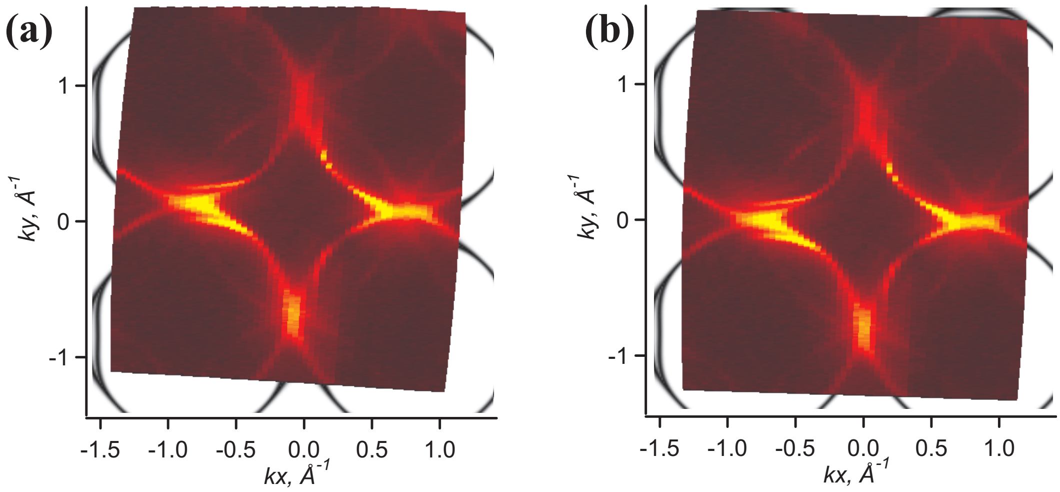

Figure 3.9: Determination of the offsets to the manipulator angles φ, α, θ. The first image shows a typical map of $(BiPb)_2Sr_2CaCu_2O_{8+\delta}$ built using uncorrected angles: $\varphi = \varphi_{\text{manip}}, \alpha = \alpha_{\text{manip}}, \theta = \theta_{\text{manip}}$. The second image gives the same, with corrections taken into account: $\varphi = \varphi_{\text{manip}} + \varphi_{\text{offset}}, \alpha = \alpha_{\text{manip}} + \alpha_{\text{offset}}, \theta = \theta_{\text{manip}} + \theta_{\text{offset}}$.

angle φ: $I = I(E_{\text{kin}}, \eta, \varphi)$, which, using the formulae 3.4, can be transformed to $I(E_{\text{kin}}, k_x, k_y)$. Often it is useful to plot the intensity only at some fixed energy as function of k_x and k_y. Such a plot made at the Fermi level is called a Fermi surface map. Besides providing the information about the topology of the FS, this maps are useful for precise orientation of the sample. Although the relative changes in the manipulator angles are known with accuracy better than 0.2°, the absolute values of the angles may have small offsets, resulting in “misaligned” FS maps (Fig. 3.9). Adjusting parameters $\varphi_{\text{offset}}, \alpha_{\text{offset}}, \theta_{\text{offset}}$ the absolute values for the manipulator angles can be found with accuracy comparable to their relative changes. First the parameters are manually adjusted and then an automatic fit is used to maximize the following norma:

$$N(\varphi_{\text{offset}}, \alpha_{\text{offset}}, \theta_{\text{offset}}) = \sum_{\text{data points}} I_{\text{model}}(E_{\text{FL}}, k_x, k_y) I_{\text{exp}}(E_{\text{FL}}, k_x, k_y), \tag{3.5}$$

where $I_{\text{exp}}(E_{\text{FL}}, k_x, k_y)$ is the experimental intensity calculated using formulae 3.4 with offsets taken into account, and $I_{\text{model}}(E, k_x, k_y) = \exp\left[-\left(\varepsilon(k_x, k_y) - E\right)/w^2\right]$ is the model function for the constant energy map, where for $\varepsilon(k_x, k_y)$ a simple tight binding formula of the band dispersion can be used [86]:

$$\begin{aligned} \varepsilon^{\pm}(k_x, k_y) = \varepsilon_0 - 2t(\cos k_x + \cos k_y) + 4t' \cos k_x \cos k_y \\ -2t''(\cos 2k_x + \cos 2k_y) \pm t_{\perp}(\cos k_x - \cos k_y)^2/4, \end{aligned} \tag{3.6}$$

where the sign ± switches between the antibonding and bonding bands. In Fig. 3.4

this function is plotted using gray scale coding, with black corresponding to 1, and white to 0. For the initial map positioning some approximate set of t-parameters can be used, with a later refinement at the stage of doping determination. When dealing with Bi-2212 samples, whose spectra are affected by the incommensurate superstructure of a known period $m \approx 4.75$ and presence of the shadow Fermi surface [87] it is useful to account for this fact by including the +1st and -1st superstructure replicas and shadows in the model for the FS map intensity:

$$\begin{aligned} I^{\mathrm{SS}}_{\mathrm{model}}(E_{\mathrm{FL}}, k_x, k_y) = I_{\mathrm{model}}(E_{\mathrm{FL}}, k_x, k_y) + \alpha_{\mathrm{Shd}} I_{\mathrm{model}}(E_{\mathrm{FL}}, k_x + \frac{\pi}{a}, k_y + \frac{\pi}{b}) \\ + \alpha_{\pm 1} I_{\mathrm{model}}(E_{\mathrm{FL}}, k_x + \frac{\pi}{ma}, k_y + \frac{\pi}{mb}) + \alpha_{\pm 1} I_{\mathrm{model}}(E_{\mathrm{FL}}, k_x - \frac{\pi}{ma}, k_y - \frac{\pi}{mb}). \end{aligned} \tag{3.7}$$

Here the fixed coefficients $\alpha_{\pm 1}$ and α_{Shd} determine the relative intensity of the superstructure and shadow features.

Doping level determination. An advantage of the ARPES method is that the doping level can be extracted for the same sample and for the same cleavage for which the spectra were measured. This eliminates a possible discrepancy between the doping level provided by the bulk sensitive methods and the actual doping level of the cleaved surface.

The idea is based on the Luttinger theorem [46], which based on a perturbative approach states that in the case of interacting fermions the Fermi surface still remains a well defined object, moreover its volume is the same as in the case of non-interacting particles. As for the applicability of the theorem in high-T_C cuprates, this issue has been discussed in the previous chapter. So here it is simply assumed that the theorem holds and only the technical issues are addressed.

In case of cuprates it is commonly accepted to describe the charge doping not in terms of total charge per Cu atom $\bar{n}$, but in terms of number of holes/electrons x added while doping the compound. As the undoped CuO$_2$ already contains one hole/electron, the formula (1.32) can be rewritten for x as:[†]

$$x_{\mathrm{hole}} = 1 - 2\frac{S^{\mathrm{hole}}}{S^{\mathrm{BZ}}}, \tag{3.8}$$

where S^{hole} is the area embraced by the hole doped barrels of the FS, i.e. the area

---

[†] Here the 2-dimensionality of the electronic structure has already been assumed, so the areas of the FS can be used instead of the volume.

where $\varepsilon(k_x, k_y) > 0$. [†] Therefore the problem simply reduces to finding the area of the Fermi surface.

Before doing any calculations it is instructive to estimate the accuracy with which the FS contour needs to be extracted from the data to give a required accuracy of the hole doping estimate. For simplicity, let us assume that we are dealing with purely 2-dimensional structure that has cylindrical Fermi surface of radius k_F and square lattice with lattice parameter a. It is easy to find the relations between the x and k_F and between their errors δx and δk_F:

$$x = 1 - \frac{k_F^2 a^2}{2\pi}, \qquad \delta k_F = -\frac{\delta x}{a}\sqrt{\frac{\pi}{2(1-x)}}. \tag{3.9}$$

Substituting typical values for cuprates $a = 3.85$ Å, $x = 0.15$ and desired accuracy $\delta x = 0.01$ one finds that $|\delta k_F| \approx 0.0035$ Å. For the excitation energy $h\nu \approx 20$ eV, using (3.2) we see that this corresponds to the angular error of about 0.1°, which is already at the technical limit of the current analysers and manipulators. From here it becomes clear how sensitive to small errors the method is. The errors in angle of only 0.1°, if systematic along the whole FS contour, may result in perceivable overestimation/underestimation of the charge doping.

It is also obvious that the Fermi surface map that covers only an irreducible octant, or less, is not sufficient for the purpose of accurate doping determinations, as it would be almost impossible to position such a map with accuracy comparable to 0.1°. Preorientation of the sample, using for instance X-ray diffraction, seems to be of low or no help here. One can determine the crystal high symmetry directions, but this does not allow one to position the crystal with required accuracy *with respect to the analyser*. That is why the extended maps, containing enough features to snap the map to the model and thus precisely determine the sample orientation *in situ*, are necessary.

Technical implementation of the procedure is very similar to the map positioning described above. One tries to maximize the same norma $N(\varphi_{\text{offset}}, \alpha_{\text{offset}}, \theta_{\text{offset}})$,

---

[†] For electron doping the formula gives the doping with a negative sign, to avoid this one needs to use $x_{\text{el}} = -x_{\text{hole}}$. For the bilayer split compounds such as Bi-2212 doping needs to be estimated separately for the bonding $x^{\text{BB}}_{\text{hole}}$ and antibonding $x^{\text{AB}}_{\text{hole}}$ FS sheets, the total doping can be found as $x_{\text{hole}} = (x^{\text{AB}}_{\text{hole}} + x^{\text{BB}}_{\text{hole}})/2$.

but with respect to the set of the tight binding parameters $t, t', t'', t_\perp$, implicit dependence on which comes from the model function $I^{SS}_{\text{model}}(E_{\text{FL}}, k_x, k_y)$ [†]. Obviously the norma will be maximal when the contours of the model (the dark shaded features in Fig. 3.9) are co-aligned with the bright features on the experimental FS map. Having found the best fitting parameters the area, and hence the doping, can be easily determined using numerically evaluating the following integral for each of the Fermi surface sheets [‡]:

$$S^{\text{hole}} = \int\limits_{BZ} \Theta\left(\varepsilon(k_x, k_y, \varepsilon_0, t, t', t'', t_\perp)\right) \mathrm{d}k_x \mathrm{d}k_y. \tag{3.10}$$

Fitting the FS with a tight binding formula is more preferable than just point-by-point determination of the FS contour. It not only allows one to obtain the tight-binding parameters, but also puts physical restrictions on the Fermi surface shape which might be important if the experimental maps contain regions where the Fermi level crossings are poorly defined.

[†] Introduction of ε_0 into fitting parameters would be redundant, as only the form of the FS is concerned. ε_0 determines only the absolute scale and can be set later on using band velocity or energy positions of the saddle points.

[‡] $\Theta(x)$ is a Heavyside function.

Chapter 4

Effect of impurities on renormalization in $Bi_2Sr_2CaCuO_{8+\delta}$

4.1 $Bi_2Sr_2CaCuO_{8+\delta}$, structure and general information

The discovery of superconductivity in the La-Ba-Cu-O system [88] and later on in Y-Ba-Cu-O [89] stimulated even more active search for superconductors with still higher critical temperature. In 1988 the superconductivity in Bi-Sr-Ca-Cu-O system was reported by numerous authors [76, 77, 90–93]. This cuprate family accommodates several phases with a general chemical formula $Bi_2Sr_2Ca_{n-1}Cu_nO_{8+\delta}$ and maximal critical temperatures $T_C \approx 20, 75$ and 110 K for $n = 1, 2$ and 3 respectively.

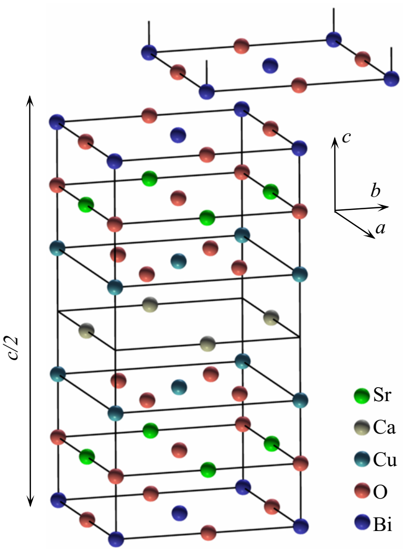

Figure 4.1: Crystal structure of $Bi_2Sr_2CaCuO_8$. The upper part of the unit cell is the same as the lower one up to a cyclic shift by $b/2$ along the **b** unit vector.

Bi-2212 has a rather exceptional structure among cuprate high temperature superconductors. Weak bonding between the Bi–O layers, that results in the natural cleavages plane and negligible k_z dispersion [94], as well as the possibility to grow high quality crystals make this material a leader in photoemission studies of high temperature

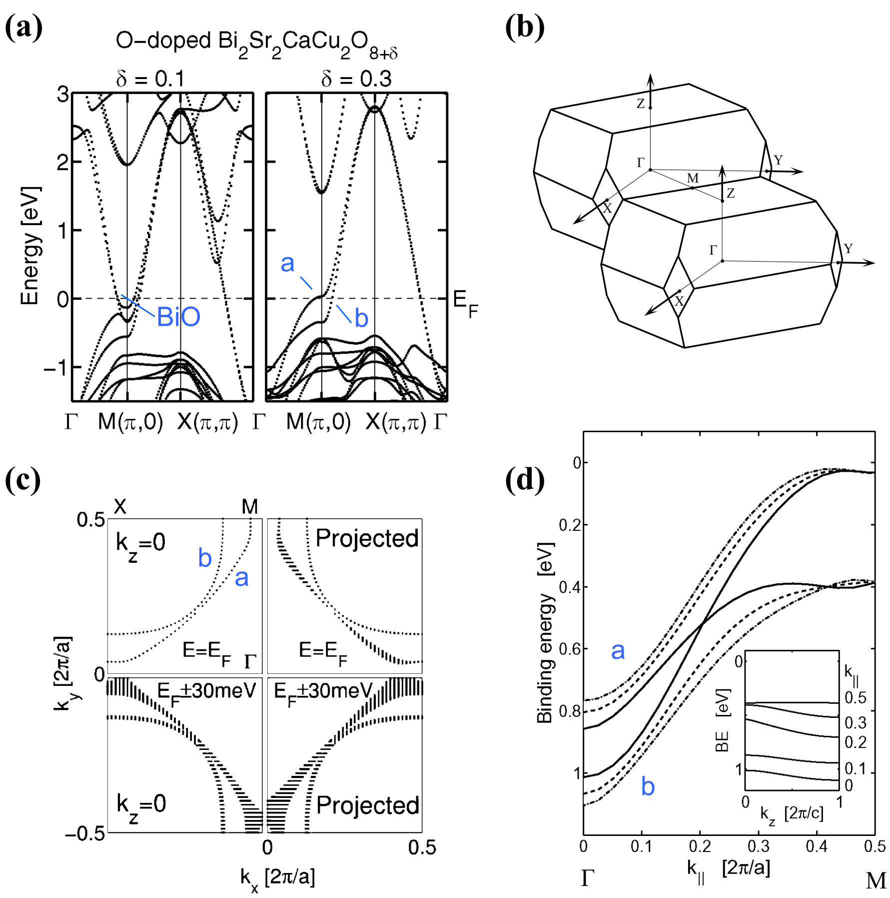

Figure 4.2: Band structure of $Bi_2Sr_2CaCu_2O_{8+\delta}$. (a) Effect of oxygen stoichiometry on the position of Bi-O pockets [98]. (b) 3-D Brilloine zone for $Bi_2Sr_2CaCu_2O_{8+\delta}$. (c) The upper two sectors show the Fermi surface for fixed $k_z = 0$ and the projected one containing contours for all $0 \leq k_z \leq \pi/c$. The lower two sectors show similar data integrated in energy window ±30 meV. (d) Band dispersion along the $\Gamma - \mathrm{M}$ direction for different k_z values; $k_z = 0$ (solid lines); $k_z = \pi/c$ (dashed), and $k_z = 2\pi/c$ (dash-dotted). Data after Ref. 99.

superconductivity. The unit cell of the $Bi_2Sr_2CaCu_2O_{8+\delta}$, or as frequently abbreviated Bi-2212, is shown in Fig. 4.1. It is a layered material that has orthorhombic structure with lattice parameters $a = 5.414\,\text{Å}$, $b = 5.418\,\text{Å}$ and $c = 30.89\,\text{Å}^{\dagger}$. Since the difference between the a and b lattice parameters is very small, the orthorhombic unit cell is being frequently substituted by a pseudotetragonal one with the lattice parameter $\tilde{a} = \tilde{b} \approx 3.82\,\text{Å}$ (see Fig. 4.3).

Typical results of band structure calculations of $Bi_2Sr_2CaCu_2O_8$ are shown in Fig. 4.2. Because of the two CuO_2 planes per primitive unit cell the low-energy copper derived band is split into a bonding and antibonding one, which are forming the Fermi surface of this compound. For the conducting samples the results of the theoretical calculations were found to be in good qualitative agreement with

---

[†] The detailed crystallographic data including the modulation in the supercell as well as the dependence of the lattice parameters on the temperature can be found in Ref. 95–97.

the experimental data [100], except for the Bi-O plane derived bands, which are usually predicted to form electron pockets at the M point. However, when taking into account the excess of oxygen in the real samples as compared to stoichiometric $Bi_2Sr_2CaCu_2O_8$ the Bi–O bands were shown to be lifted up by about 1 eV, thus removing apparent disagreement [98].

As was mentioned the k_z dispersion is frequently being neglected. Based on the results of the calculation accounting for k_z dispersion it is easy to see that such approximation is justified for most of the cases as the momentum broadening of the FS contour because of undefined k_z is comparable to the effects of energy resolution [see Fig. 4.2(c)]. Similarly variation in the band binding energy is small as long as one deals with a narrow energy range at the Fermi Level [see Fig. 4.2(d)].

Much more noticeable deviations may arise from the reduction of the lattice symmetry to the tetragonal one. Formally any infinitesimally small orthorhombic distortion changes the symmetry of the lattice and introduces a new reduced Brillouin zone with the bands flipped around its boundaries [Fig. 4.3(b)]. Concerning the photoemission, it is obvious that the gradual distortion of the lattice cannot lead to an abrupt appearance of the flipped fragments of the Fermi surface. The intensity of these fragment would be suppressed by the photoemission matrix elements and will grow in strength as the distortion is increased. Indeed, such relatively weak flipped bands have been observed in photoemission data, but various reasons for their origin were initially suggested [87,101,102]. Only lately the so-called shadow Fermi surface, formed by the flipped fragments, was identified with orthorhombic lattice distortions [103–105] and, possibly, the final state diffraction at the $c(2 \times 2)$ surface superstructure [106].

There is also another complication of similar character. Strictly speaking the displayed in Fig. 4.1 structure was only a subcell. The atomic positions in the true structure turn out to be modulated along the **b** direction with incommensurate period $4.76b$. This modulation was clearly detected by surface sensitive techniques, such as LEED [76, 77] and tunneling microscopy [78, 79], as well as by the bulk sensitive X-ray diffraction [95], and thus cannot be related to some kind of surface instability. Among the reasons for the modulation [92], a mismatch between the perovskite block and the stereochemical requirements of the Bi in the Bi-O layers seem to be the most viable ones [95]. In case of ARPES the lattice modulations turn out to be an additional obstruction leading to the appearance of the superstructure

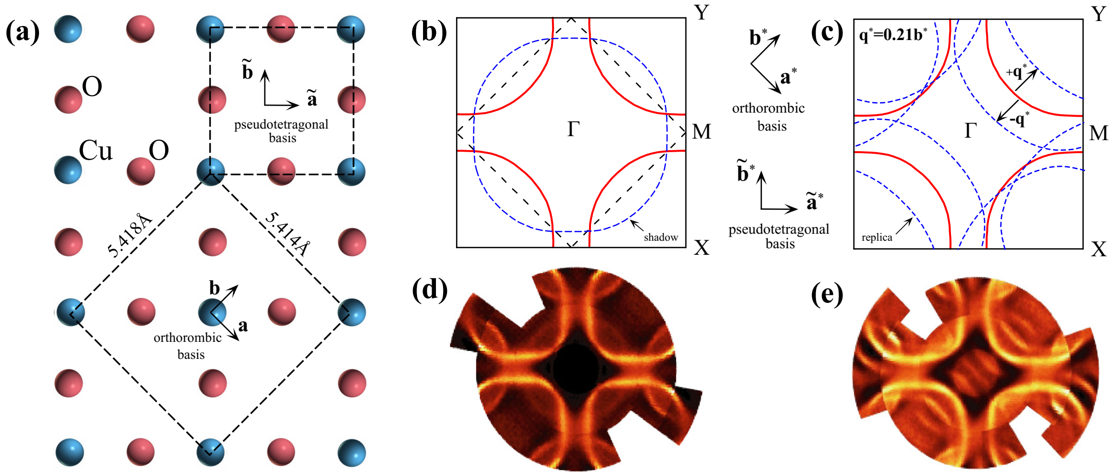

Figure 4.3: (a) CuO$_2$ plaquette, orthorhombic and pseudotetragonal unit cells. (b) Fermi surface folding when changing from tetragonal (solid square) to orthorhombic (dashed square) unit cell. The unfolded Fermi surface is shown by the red solid lined. The elements of the folded FS are plotted by a dashed blue trace. (c) Appearance of the superstructure due to the incommensurate lattice modulation along the b direction with period of $\sim 4.75b$. (d)–(e) Manifestation of the FS folding (shadow FS) and superstructure replicas in ARPES spectra, experimental data after Ref. 112.

replicas in the spectra [107–110]. In the particular case of the FS these look like a set of features shifted by the incommensurate vector $\mathbf{q}^* \approx \pm 0.21\mathbf{b}^*$. Schematic demonstration of the effect can be found in Fig. 4.3 (c),(e). As the recent controversy [111–113] demonstrates, the effects of shadow Fermi surface and replicas should not be disregarded when dealing with ARPES data for Bi-2212.

4.2 Unusual renormalization effects in BiSr$_2$Ca$_2$CuO$_{8+\delta}$

This subchapter is meant to provide the reader with a brief overview of experimental facts concerning the renormalization effects observed in BiSr$_2$Ca$_2$CuO$_{8+\delta}$ and their interpretations. Generally the word renormalization denotes the net result of all interactions in the system that change the observed binding energy of the quasiparticles and lead to their finite life-time, which can be described in terms of the self-energy. While for a normal metal a Fermi liquid model with

$$\Sigma^{\text{el–el}}(\mathbf{k},\omega) = \alpha\omega + i\beta\left[\omega^2(\pi k_B T)^2\right] \tag{4.1}$$

can be considered as a good approximation [48, 114], already early experiments revealed that the high temperature superconductors in the normal state, in particular Bi-2212, do not fit within the frames of the Fermi liquid model. The deviations are especially distinct for the underdoped samples, when, in particular, the imaginary self-energy has quasi-linear dependence on the energy instead of being quadratic [115].

In the superconducting state the self-energy undergoes additional modifications. There is remarkable discontinuity-like behaviour in the electron self-energy that can be seen even in the raw data. This deviation is normally referred to as "unusual" renormalization. Traditionally the earliest measurements were done at the high symmetry parts of BZ, the nodal and antinodal regions. Along the nodal direction (Γ–X, or Γ–Y) the renormalization effects are represented by the so-called "kink" in the experimental dispersion [69, 116, 117], whilst in the vicinity of the $(\pi, 0)$ point of the Brillouin zone (BZ), the renormalization is noticeably stronger and makes itself evident even in the line shape of the single energy distribution curve (EDC) [71, 72, 118]. There are no qualitative or abrupt changes from the "kink" feature to the spectrum observed in the vicinity of the antinodal point, the feature gradually changes from one to the other [69].

Nowadays it is widely accepted that coupling to a collective mode [42, 119] naturally explains these anomalies. The origin of this mode remains a current controversy between two most frequently proposed candidates that are phonons and magnetic excitations.

Existing photoemission data suggest substantial dependence of the coupling between the electrons and the mode on momentum [117], and hole doping [72, 120]. Temperature dependent measurements [71, 115, 121], demonstrating strong suppression of the renormalization just above the T_C, what nicely fits to the disappearance of the magnetic resonance in the normal phase. Typical dependence of the renormalization on momentum and temperature is shown in Fig. 4.4. As can be seen the renormalization disappears rather abruptly in the temperature range 59–88 K and further temperature increase does not produce any spectacular changes to the spectra. Thus the vanishing of the renormalization at high temperature is unlikely to be explained by the "visual" effect of temperature smearing if adhering to the traditional phonon scenario.

However, other similar ARPES experiments were nonetheless interpreted in

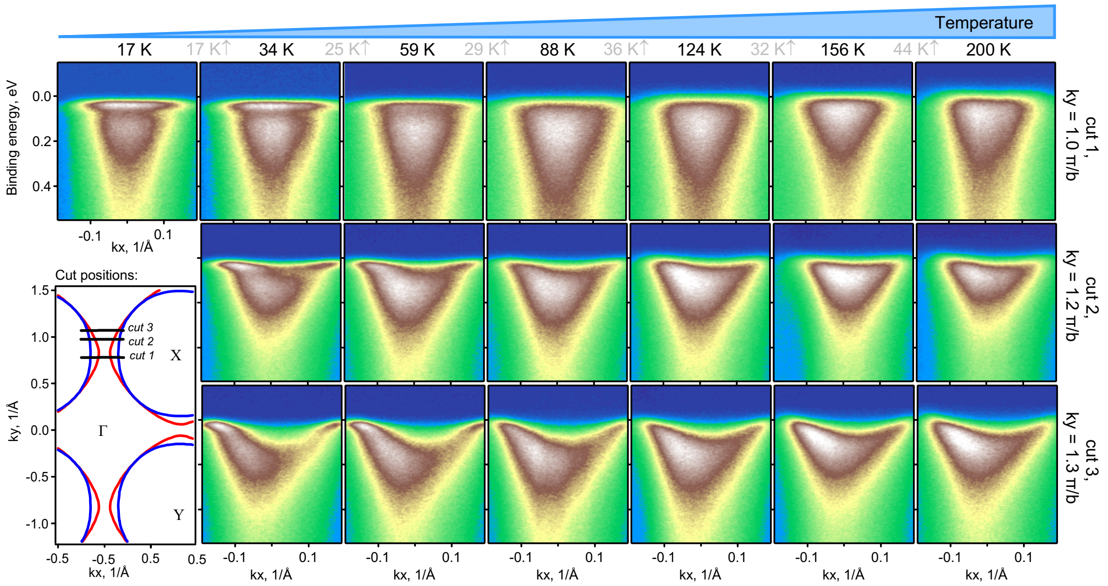

Figure 4.4: Typical dependence of the renormalization on temperature and momentum, i.e. position in the Brillouin zone for the underdoped $Bi_2Sr_2(Ca_{1-y}Dy_y)Cu_2O_{8+\delta}$ sample. Each column corresponds to a fixed temperature stated on top of the column. Similarly each row represents the spectra measured at fixed cut position. The positions are denoted in the inset in the left bottom corner. The spectra were measured with $h\nu = 50$ eV, thus mainly the antibonding band is contributing to the spectra.

terms of phonons [70, 122]. To support the coupling to phonon modes as a main origin for the nodal kink in the dispersion Shi et al. [123] and later Zhou et al. [124] attempted to extract the Eliashberg function and match the observed scales to the known phonon modes. Despite of being interesting and innovative the data analysis was later on criticized as unreliable [124, 125]. Pointing to a richer structure in the experimental data than physically possible, T. Valla suggested that the features observed in the experimental self-energy should be considered as a noise rather than traces of coupling to multiple phonon branches.

This topic has been addressed in many details by the opposite parties in the recent reviews by M. Eschrig [57] and T. Cuk et al. [126], so further details can be found therein. To make a brief summary one needs to mention that a common point of view has not been agreed upon and additional experiments are necessary to arrive at more definitive conclusions.

4.3 Effect of impurities on electron renormalization

To elucidate the nature of the collective mode that causes the strong renormalization of the one-particle spectral function and might be responsible for the superconductivity itself, one could try to vary separately either the phononic or magnetic excitation spectrum. Variation in the phononic spectrum can be achieved by the use of different isotopes. Such an experiment for HTSC has recently been reported [127]. However along with the fact that the observed effect seems to be "unusual", as all major effects have been observed at high energies of 100-300 meV, it did not get any support in the independent measurements [128], which leaves the problem of low-energy anomalies that are relevant for the superconductivity, unsolved. In case of magnetic excitations, there is a possibility to change the magnetic spectrum via doping different types of impurities into the CuO_2 plane. It is known from inelastic neutron scattering (INS) [129, 130] that substitution of Zn and Ni leads to substantial changes in the magnetic spectrum.

In this chapter a systematic study of the Zn and Ni impurities effect on the renormalization in $BiSr_2Ca_2(Cu_{1-y}M_y)O_{8+\delta}$ (M=Zn, Ni) both in the nodal and antinodal region will be presented. The experiments were carried out at the U125/1-PGM beam line with SCIENTA SES100 spectrometer at BESSY. Overall energy resolution was set to 20 meV, and angular resolution was 0.2°, which yields a wave vector resolution 0.013 $Å^{-1}$ and 0.009 $Å^{-1}$ for 50 and 27 eV excitation energies, respectively. All data were acquired at $T = 30$ K in the superconducting state for three high quality samples: nearly optimally doped pure Bi-2212 ($T_C = 92$ K), Zn substituted Bi-2212 with nominal Zn concentration close to 1% ($T_C = 86$ K), and 2% Ni substituted Bi-2212 ($T_C = 87$ K).

First we consider the antinodal region. In general case the EDC, the curve that represents the distribution of photo-intensity as a function of energy at fixed momentum, taken at the $(\pi, 0)$ point [see Fig. 4.5(a)] would consist of two peaks due to the bilayer split band [131], that are schematically shown in Fig. 4.5(a). The intensity of the bonding band was found to be negligibly small for certain excitation energies [131](in this case $h\nu = 50$ eV). Nevertheless, at least for the underdoped samples [132], the line shape is not reduced to a single peak and has a dip at a higher binding energy. The appearance of the dip in a single band EDC is well explained in terms of coupling to a collective mode [42, 119]. Such an interaction

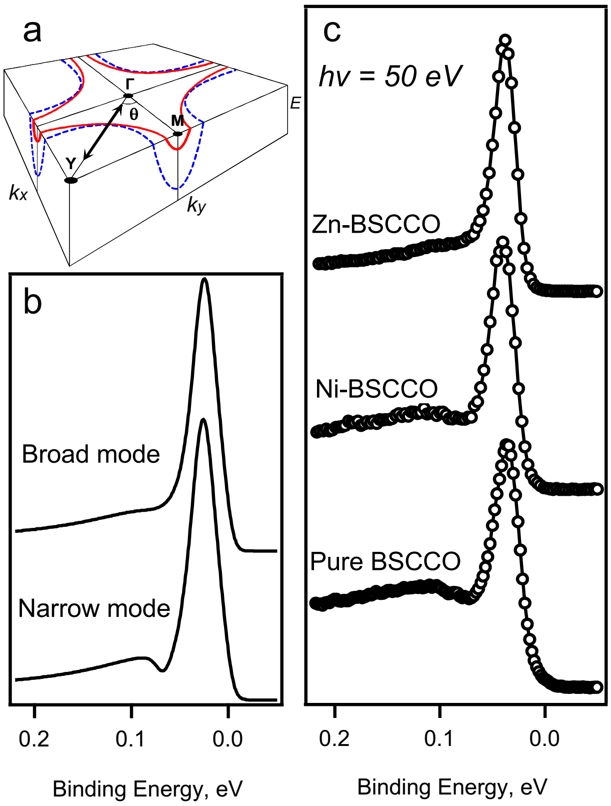

Figure 4.5: (a) Cut of a $k\omega$-space at the Fermi level. The top of the cube contains two sheets of the Fermi surface, red solid line corresponds to the dispersion of the antibonding band, blue dashed one — to the bonding band. k_x and k_y axes are directed along the horizontal edges of the cube. (b) Model line shape of the $(\pi, 0)$ EDC, when coupled to a narrow (2 meV) and broad (20 meV) collective mode. (c) Experimental EDC taken at $(\pi, 0)$ point.

with a sharp mode with energy Ω_{mode} leads to the increase of the scattering rate at binding energies higher than $\Omega_{\mathrm{mode}} + \Delta$, where Δ is a superconducting gap, i.e. to a step like feature in the imaginary part of the self-energy and a logarithmic divergence in the real part of the self-energy giving rise to a dip in photoemission line shape. When the mode has a finite width the dip smears out as demonstrated in Fig. 4.5(b). Therefore, the dip can be a good indicative of the mode width and energy. Broadening of the mode described above well corresponds to our experimental data presented in panel (c) of Fig. 4.5. Comparing these EDC's, measured at $(\pi, 0)$ point with 50 eV photon energy, one can notice a striking difference in the line shapes caused by the impurity substitution: while for the pure sample the spectrum has a pronounced dip, for the Zn substituted sample the dip almost completely vanishes. For the Ni substituted sample the dip "strength" is intermediate.

Another change in the spectra that one can notice is an increase of the intensity of the low-energy peak relative to the spectral weight at higher binding energies upon Ni substitution and even stronger effect on Zn substitution. In a simple model where the step in $\mathrm{Im}\,\Sigma$ is proportional to the mode spectral weight times the coupling strength the intensity variation could be accounted for by a stronger coupling

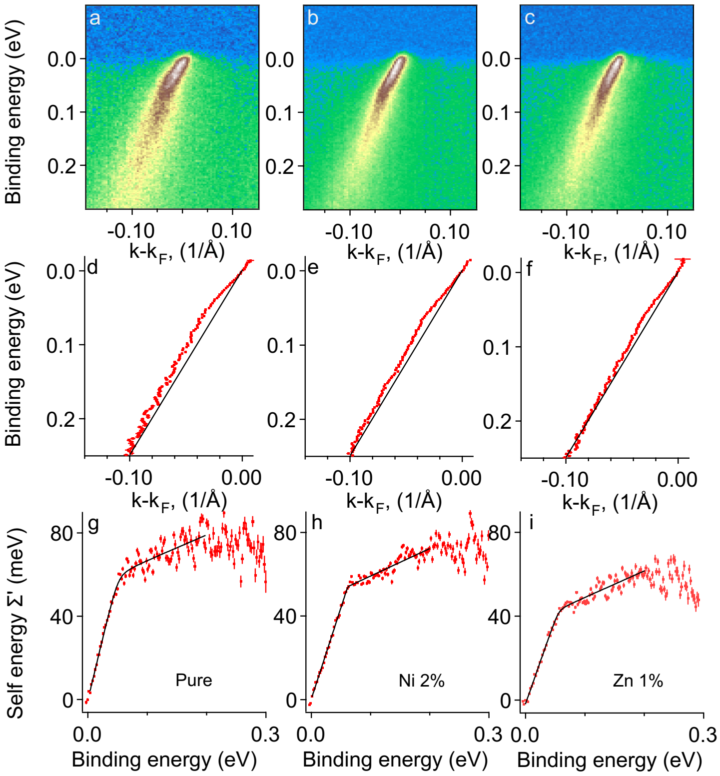

Figure 4.6: (a)–(c) Photocurrent intensity distribution in the nodal cuts. (a) Pure Bi-2212, (b) Ni substituted and (c) Zn substituted Bi-2212. Middle row shows corresponding experimental dispersion. In the last row the real part of the self-energy obtained by subtractions of the bare band is displayed. The black solid lines are guides to eye, while the red symbols represent the data points.

to the mode upon impurity substitution. A higher coupling to the mode would be related to a larger imaginary part of the self-energy and this would cause a stronger broadening and therefore a reduction of the intensity in the “hump” region. On the other hand such a broadening would also result in a flattening of the hump that has not been observed. Thus, in order to account for all changes in the line shape one also has to consider the whole spectrum of spin fluctuations [68, 74] as well as possible difference in elastic scattering contributions (e.g. due to different surface qualities) and different extrinsic backgrounds.

Now we turn to the nodal direction. The nodal cuts [Fig. 4.6, (a–c)] were measured strictly along the BZ diagonal. The aforementioned position in k-space was guaranteed by the measured maps, that were used to orient the sample. In addition the sample orientation was double checked using the steepest experimental dispersion as a criterion for the true nodal cut. Since the nodal region is also complicated by bilayer splitting [133], the matter of excitation energy remains important here too. Therefore the nodal spectra were measured with $h\nu = 27$ eV, when again only one of the bilayer split bands is visible [133]. The second row of Fig. 4.6 shows the experimental dispersion obtained from the maxima position of the Lorentzians providing the best fit to the momentum dispersion curves (MDC). The straightforward

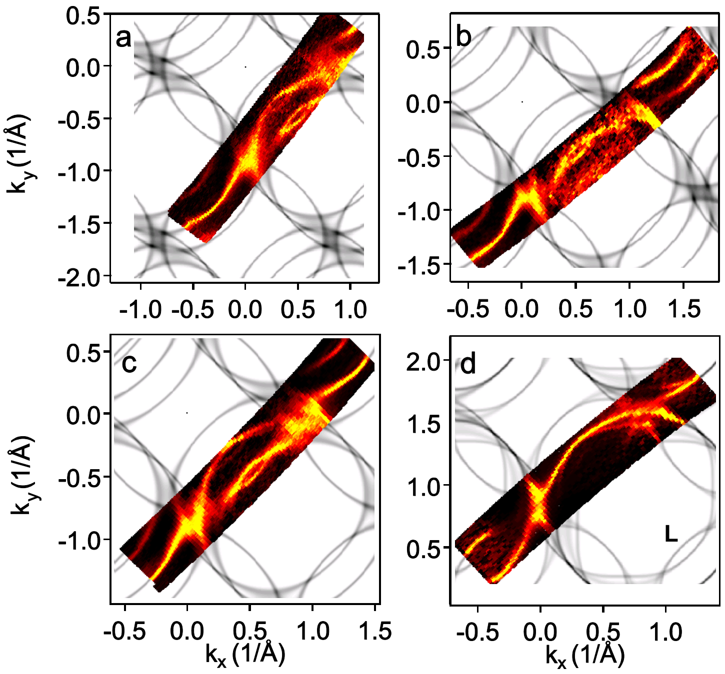

Figure 4.7: Cuts of $k\omega$-space made 20 meV below the Fermi level and tight binding fits. (a) Ni substituted sample. (b) Zn substituted sample. (c) Pure Bi-2212 close to optimal doping. (d) Overdoped Bi-2212, $\delta \approx 0.20$; letter L denotes "lens" formed by the shadow band and the 1st order diffraction replica.

way to estimate a degree of the renormalization effects is to draw one and the same "guide" line from the Fermi level to some fixed point on the experimental dispersion curve and treat the area between the dispersion curve and the guide line as an effective measure of renormalization. It is easy to see that renormalization in case of the Zn substituted sample is decreased as compared to the pure sample. Subtracting a bare particle band from the experimental dispersion the real part of the self-energy can be obtained. Here, as follows from a self-consistent Kramers-Kronig procedure [41], for the bare band dispersion a parabolic band with its bottom lying 0.8 eV below the Fermi level was used. Defining a coupling constant as the derivative of the real part of the self-energy at the FL one finds that $\lambda_{\text{pure}} \approx 1.06$, $\lambda_{\text{Ni}} \approx 0.88$, and for the Zn doped sample it has the lowest value $\lambda_{\text{Zn}} \approx 0.76$. It is worth to note that although the obtained absolute values for λ depend on the parameters of the bare band dispersion, their ratio remains almost insensitive to the position of the bottom of the bare band, provided that the bare band is the same for all three samples. Therefore more accurate would be to say that the coupling constant for the nodal direction is reduced by approximately 15% for the 2% Ni doped sample and by 30% for 1% Zn doped sample as compared to the pure one.

To make a connection between the observed suppression of the renormalization and the impurity substitution hole doping level of the samples cannot be left as an uncontrolled parameter as it is known that the renormalization features are weakening with overdoping both in nodal and antinodal directions [72, 120]. Therefore different hole doping might be a possible explanation. In order to evaluate the hole doping level, Fermi surface maps were measured for all samples. These maps, in addition, allowed for a precise positioning in the reciprocal space, when measuring nodal and antinodal spectra.

The experimental data, which are the cuts of $k\omega$-space made 20 meV below the Fermi level for the three samples under consideration, are summarized in Fig. 4.7. For comparison, the panel (d) contains an identical cut for the overdoped sample with the hole doping δ within 0.19 – 0.20. Grey scale images below the experimental data represent tight-binding fits to the antibonding sheet of the Fermi surface (FS) [134]. The first estimate for the doping level can be made by the size of “lens” [Fig. 4.7(d)] formed by the shadow and the 1st order diffraction replica. Observing the four maps, it is clear that the first three samples have very close hole doping, and that the doping of the fourth sample is notably higher. To be quantitative, the area of antibonding sheets of the FS cuts can be used as a good relative doping measure. Evaluation gives the following result: $(S_a - 1/2) : (S_b - 1/2) : (S_c - 1/2) : (S_d - 1/2) \approx 1.00 : 1.01 : 0.98 : 1.14$, where S_i denotes the ratio of the area confined by one “barrel” to the area of the whole BZ. The values for S_i were obtained from the tight-binding fit of experimental map for each panel (a–d). Since a charge doping induced suppression of the renormalization features would require a deviation of the hole concentration of about 30 % [72], we see that the difference in charge doping for the samples is negligible and cannot account for the substantial change in the line shape [Fig. 4.5(c)] at the antinode, as well as for the different renormalization constants (Fig. 4.6) for the nodal spectra.

At the same time the discussed experimental observations of the dip smearing in the antinodal EDC are in good agreement with the results of inelastic neutron scattering (INS) experiments. The comparison with INS is most pertinent here, since it gives a detailed insight into the changes in the spectrum of magnetic excitations produced by the impurities and allows for a comparison with the modifications seen in ARPES spectra. The direct observation of the magnetic resonance mode by INS in YBCO demonstrates its strong sensitivity to impurities incorporated into CuO_2 planes. When for the pure sample the mode is sharply peaked at $\sim$ 40 meV with a FWHM being resolution limited [66], for 1% Zn substituted YBCO the mode attains

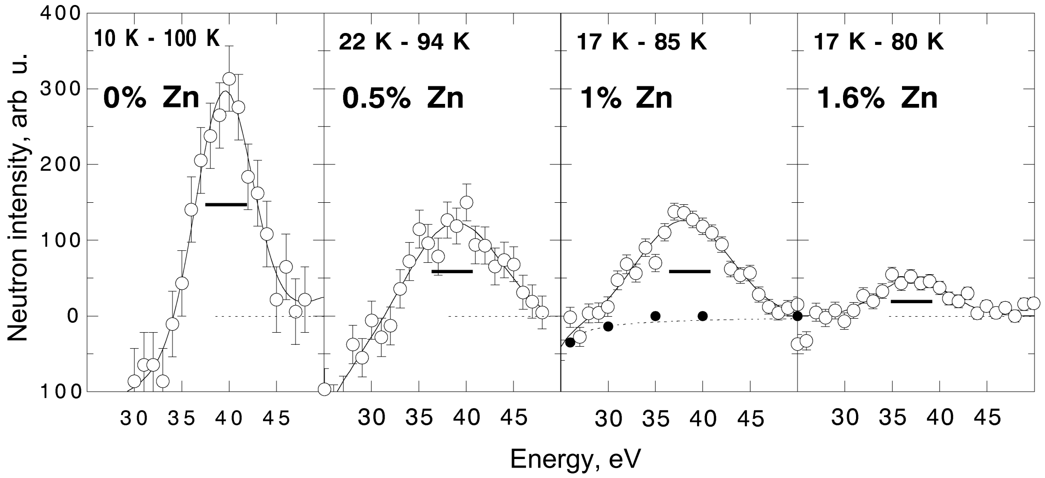

Figure 4.8: Effect of Zn substitution on the spin resonance in $YBa_2(Cu_{1-y}Zn_y)_3O_7$. Measurements have been normalized against phonons. The open symbols are the difference between the neutron intensity below and above T_C. Data after Refs. [67, 129, 130, 135].

a finite width of about 10 meV [129] with further gradual broadening for higher Zn concentrations (see Fig. 4.8). From Ref. 129 it follows that introduction of 3% Ni results in approximately the same intensity of the resonance at its peak as in the case of 1% Zn doping, supporting the idea that nonmagnetic Zn has stronger influence on spin dynamics than Ni, which is in agreement with the ARPES spectra.

Raman scattering experiments on optimally doped YBCO [136] show that the A_{1g} electronic collective mode, that follows the acoustic part of the magnetic resonance, gradually broadens with increase of Zn concentration. For 2% Zn substituted YBCO the A_{1g} mode almost disappears, while this is not the case for 3% Ni substituted YBCO where the mode loses only about half of its intensity [137]. It is also worth mentioning that Raman scattering experiments on Zn and Ni substituted YBCO crystals show no apparent changes in the structure of phonon anomalies [138, 139] at room temperature suggesting that the lattice dynamics remains unchanged. Similar results, except for the peak at 340 cm^{-1}, are obtained in Ref. 140 for the superconducting state. This peak shows small decrease of its intensity and insignificant, as compared to magnetic resonance mode, broadening from 1.6 to 1.9 meV. It is clear that such a broadening cannot account for the vanishing of the dip in the $(\pi, 0)$ spectra. Therefore one can conclude that the smearing of the dip in the ARPES antinodal spectra with impurities doping is a straightforward consequence of the magnetic resonance mode broadening, and possibly decrease of its (the mode) integral intensity.

For the nodal direction the situation is more complicated. According to [74] the renormalization effects in nodal spectra are mainly caused by scattering of the electrons between the nodes and the Van Hove singularity in the density of states at the $(\pi, 0)$ point by the resonance mode centered at the antiferromagnetic vector $Q(\pi, \pi)$. This serves as a good explanation for the fact that the renormalization effects are much weaker in the node than those in the vicinity of the $(\pi, 0)$ point. But it also means, that the renormalization has to increase with the resonance mode broadening in momentum space when impurities are doped into CuO_2 plaquette [129]. On the contrary, our observations show that the dimensionless coupling constant λ, decreases suggesting that the scattering by the antiferromagnetic vector $Q(\pi, \pi)$ does not constitute the dominant contribution in the nodal spectra renormalization effects [73]. The new resonance feature in the magnetic excitation spectrum [141, 142] peaked at energy close to 54 meV and incommensurate vector $Q^*_{\mathrm{IC}}(0.8\pi, 0.8\pi)$ provides scattering between the nodes, and therefore, should have a strong influence on the nodal spectra renormalization effects. However its evolution with impurity doping needs to be clarified, in order to check its pertinence for the problem in hand.

4.4 Summary

In this chapter it was shown that the substitution of Cu atoms in Cu-O plane changes renormalization features in ARPES spectra both in nodal and antinodal parts of the Brillouin zone. The smearing of the dip in the antinodal EDC can be well explained by coupling of electrons to the magnetic resonance mode. The effect of Zn and Ni substitution on the antinodal ARPES spectra is in good agreement with the influence of these impurities on magnetic resonance mode seen by INS experiments. This in addition to the previous ARPES studies of temperature and doping dependence [72, 117, 120, 133] of peak-dip-hump structure, mass renormalization near antinodal region and a kink in the nodal part of Brillouin zone, provides another evidence that the coupling to magnetic excitations, rather than phonons, is responsible for the observed unusual renormalization effects.

Chapter 5

$YBa_2Cu_3O_{7-\delta}$, electronic structure and renormalization effects

5.1 General information, crystal structure

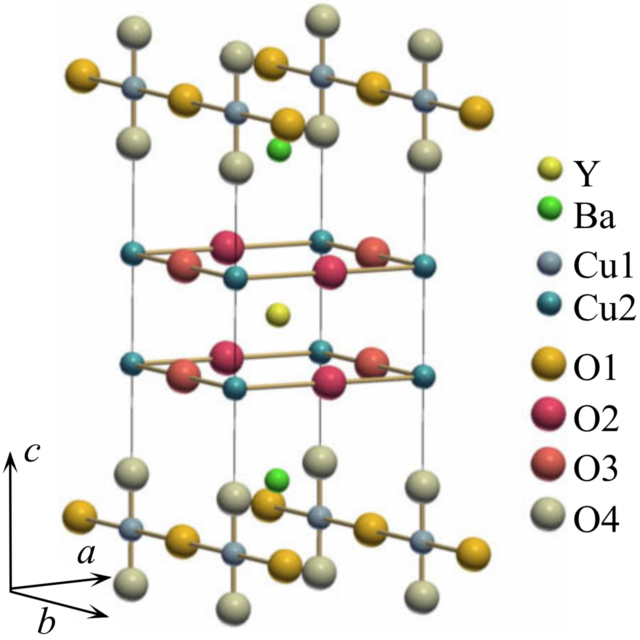

Figure 5.1: Crystal structure of $YBa_2Cu_3O_7$.

$YBa_2Cu_3O_{7-\delta}$ or YBCO-123 is the first superconductor to cross the boiling point of liquid nitrogen. The material was found by Paul Chu and his students at the University of Houston in 1986 [89] soon after the initial discovery of high temperature superconductivity by Bednorz and Müller [88]. Like all copper-oxide based high temperature superconductors it is a layered material and contains two CuO_2 planes per unit cell (Fig. 5.1) separated by a layer of Y atoms. The distinct feature of this superconductor is a set of one-dimensional CuO_3 chains running along the b-direction, which results in noticeable orthorhombicity of this material. There is also an evidence that the CuO_2 planes are not perfectly flat, but are slightly buckled, so that the O(2) and O(3) sites are shifted by $0.064a$ and $0.070a$ towards the neighbouring CuO_2 planes and thus become inequivalent [143].

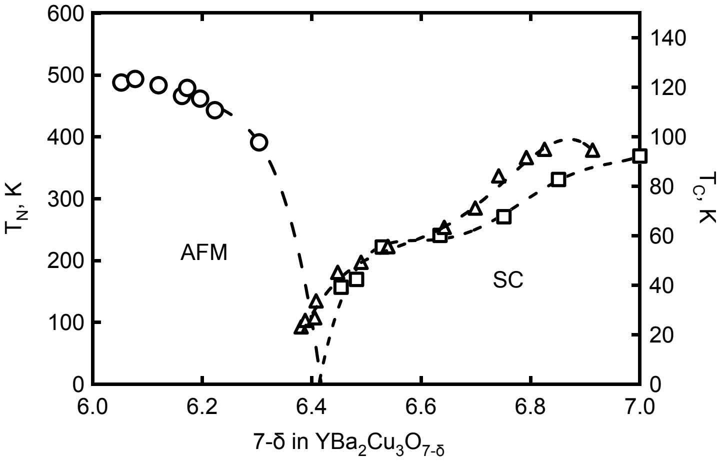

Figure 5.2: Néel and T_C temperatures vs oxygen stoichiometry for $YBa_2Cu_3O_7$. Triangles represent the data after Ref. 149, circles and squares are from Ref. 150. AFM and SC stand for antiferromagnetic and superconducting regions in the phase diagram.

The lattice parameters are $a = 3.822\,\text{Å}$, $b = 3.887\,\text{Å}$, and $c = 11.680\,\text{Å}$. †

Perfectly stoichiometric crystals of this material turn out to be slightly overdoped. Annealing as-grown crystals in the inert atmosphere one can partially remove oxygen atoms from O(1) sites in the chains, resulting in the non-stoichiometric compound $YBa_2Cu_3O_{7-\delta}$ [147,151]. This is an important procedure, as for Y-123 it is the amount of oxygen that determines the hole doping level of the CuO_2 planes. Typical relation between T_C and δ is given in Fig. 5.2. Already at $7-\delta \approx 6.35$ critical temperature drops to zero and samples turn into an antiferromagnetic charge transfer insulator [152–154]. There are also accompanying changes in the lattice symmetry. At low oxygen content $7-\delta \lesssim 6.35$ the crystal has tetragonal structure, while for higher chain filling and sufficiently low temperatures the symmetry changes to orthorhombic.

Additionally accounting for the ordering of the oxygen in the chains one can single out several orthorhombic phases [155–157, 160] that are emerging due to formation of different superstructures (see Fig. 5.3). The ordering effects are particularly notable when the chain filling $7-\delta$ is close to 6.5, i.e. when the oxygen atoms tend to arrange in a way that each second chain is filled, forming a so-called ortho-II phase. Existence of this phase is believed to be, at least partially, responsible for the "6.6"-plateau (see Fig. 5.2) in the dependence of T_C on the oxygen content [161]. However is not the only aspect of oxygen ordering. Chain fragmentation and disorder are known to decrease the hole doping of the CuO_2 planes [162,163], which

---

† The parameters are given for the sample with $7-\delta = 6.96$ and were measured at room temperature [144]. Further details, in particular temperature dependence and dependence on stoichiometry and impurities can be found in Refs. 65,145–148.

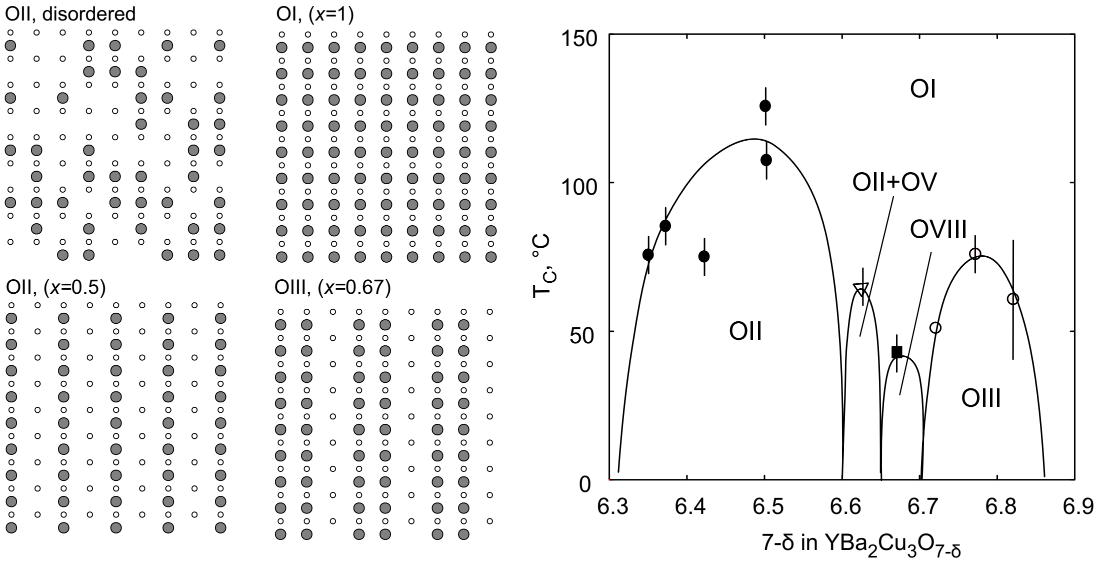

Figure 5.3: Patterns of oxygen ordering for different phases, empty and filled circles correspond to Cu and O atoms. (c) $\delta - T$ phase diagram is based on the data from Ref. [155–159] .

can be easily observed in experiment by quenching the high temperature disordered phase.

The oxygen ordering makes the dependence of T_C on the oxygen content rather ambiguous, especially at low oxygen filling, when the difference in T_C between the ordered and disordered phases may reach up to 10 K (7-δ=6.5) [164], or even turn the sample from insulator to superconductor (7-δ=6.4) [162]. However, there is empirical evidence of one-to-one correspondence between the hole doping level p and the lattice parameter c as well as the critical temperature T_C, that, in certain cases, alleviates the problem of charge doping determination [165].

Although the charge doping mechanism realized in Y-123 is superior in terms of charge homogeneity to the introduction of interstitial oxygen atoms, as in the case of Bi-2212 [166–169], it has also certain drawbacks. Unfortunately controlling the oxygen stoichiometry does not allow for substantial overdoping as the amount of oxygen is limited to 7 atoms per unit formula. One possible way to overcome this problem lies through a partial substitution of Y^{3+} ions with Ca^{2+}, which nominally brings one additional hole to the neighbouring CuO_2 layers per one substituted atom. Ca-substitution is a rather successful way of controlling the doping level and according to Ref. 170 it is equivalent to oxygen doping for low amount of substituted atoms ($\sim$ 2%). However at substantial Ca substitution a difference appears [171], as substituted cations dope holes mainly into CuO_2 plane, unlike conventional oxygen doping that introduces holes both into the CuO_2 planes and into the apical oxygen sites O(4).

5.2 Theoretical electronic structure

Obviously, the electronic structure, especially the low energy one is important for understanding the physics of any material. Theoretical calculations and experimental studies have been the two complementary sources of information about the detailed band structure. As the early photoemission data was not abundant in details the theory played a role of a guiding star helping experimentalists to understand their results. Thus a discussion of the theoretically predicted band structure appears to be a reasonable starting point.

Typical results of band structure calculations for the $YBa_2Cu_3O_7$ are summarized in Fig. 5.4. Although the full energy band structure seems to be very intricate, the picture is rather transparent in the close vicinity of the Fermi level, as there are only four bands predicted to form the Fermi surface.

There is a pair of CuO_2 plane derived bands crossing the Fermi level along the XS/UR and YS/TR directions, which are symmetric and antisymmetric combinations of the layer $pd\sigma^\star$ antibonding bands. The band, whose wave functions are symmetric with respect to the mirror plane set between the two CuO_2 layers, has higher binding energy and therefore is called a bonding band. This band is denoted by the letter ‘b’ in the Fig. 5.4. The other one, which is antisymmetric, is called an antibonding band and is labeled by the ‘a’ letter. These are the bands that are forming two major sheets of the Fermi surface [Fig. 5.4(c)] that look like a pair of concentric square-like contours around the S/R point.

The remaining two bands are the chain and the stick bands, denoted by letters ‘c’ and ‘s’. These mainly originate from the chain structure. The orbitals essential for the ‘c’ band are the chain $pd\sigma^\star$ band made from $O1_y$ and antibonding $pd\sigma^\star$ dumbbell orbital $O4_z$-$Cu1_{z^2-y^2}$-$O4_z$. As can be seen this band has a pronounced one-dimensional character with a strong dispersion along the y-direction and a rather weak dispersion along the x-direction. The orbitals important for the stick band are the antibonding $pd\pi^\star$ dumbbell orbitals ($O4_x$-$Cu1_{xz}$-$O4_x$ and $O4_y$-$Cu1_{yz}$-$O4_y$) and the linear combination of the $O1_z$ and the $pd\pi$ bonding dumbbell orbital

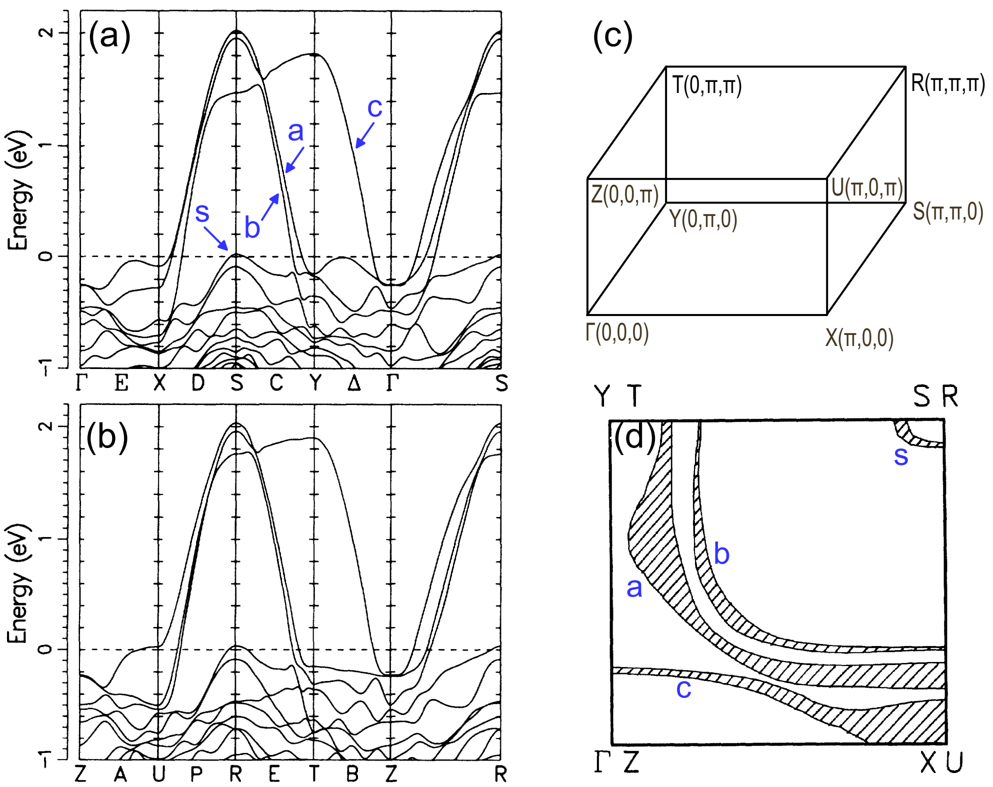

Figure 5.4: LDA band structure after Ref. 172, panel (a) for $k_z = 0$ and panel (b) for $k_z = \pi/c$. (c) High symmetry points in the 1st Brillouin zone. (d) Projected Fermi surface to be compared with photoemission experiment with no k_z selectivity.

$O4_y$-$Cu1_{yz}$-$O4_y$.

In addition to the bilayer splitting and quasi one-dimensional chain band another remarkable outcome of the LDA calculations for YBCO-123 is a notable k_z-dispersion, in particular for the chain band in the vicinity of X/Y point, which makes it different from Bi-2212 or even its closest relative YBCO-128.

5.3 Previous ARPES data and motivation for further studies

There is no big difference among the calculations performed by different authors [134,172,173] nowadays. However the LDA method is known to predict sometimes wrong positions for particular bands [174,175], though the method is still expected to be applicable, which make the experimental check a necessary step. Besides the basic band structure, the experiment can bring extra information about the many-body physics, which is beyond the band structure calculations, as they do not take into account all the electronic correlations in the system.

In the case of Bi-2212, the correspondence between the theoretical band structure and the renormalized quasiparticles observed in ARPES experiment was set up comparatively easy [98, 109, 176–180], so the attention could have been redirected to further detailed studies of the gap symmetry [176, 181, 182], unusual renormalization effects detected in the spectra [41, 69, 71, 117, 183], and attempts to find an experimental evidences that could ascertain the origin of the observed renormalization [70, 121, 132, 184]. However, for the case of YBCO-123 even unambiguous identification of spectral features confronted the researches with difficulties due to substantial differences in data interpretation among various studies [149,185–191].

Before going into details one actually has to substantiate why it is worth to continue the attempts with the compound universally considered to be unsuitable for ARPES investigations instead of changing for something simpler. There are several reasons that make this particular high-T_C cuprate family interesting. One of the reasons is that Y-123 has the most pronounced orthorhombic symmetry out of all high-T_C cuprates, so it is commonly believed that this anisotropy should also be marked in its superconducting properties via a deviation from pure d-wave pairing state [189]. Another reason is due to the availability of large high quality crystals, that made Y-123 the most thoroughly studied cuprate by the volume sensitive techniques. Particular interest is raised by the recent inelastic neutron scattering (INS) experiments [65, 66, 80, 141, 192–207], that provide us with the most detailed insight into the spectrum of magnetic excitations for this compound.

The early photoemission experiments on YBCO-123 date back to measurements done with X-rays in angle integrated mode. A profound review of this data can be found in the Ref. 187, while here only some of the most recent measurements, which are sufficient to describe the level of agreement between theory and the experiment as well as elucidate the encountered problems preventing further advance in studying this material, will be addressed.

Fig. 5.5 gives the summary on the experimentally observed band dispersions and their identification by some of the authors. While in one of the earliest works [208] it is claimed that both bonding and antibonding bands are clearly detected and that these bands are forming extended saddle points along Γ-X/Y-Γ direction with binding energies of about 19 and 150 meV, in the Refs. 185 and 186 it is believed that the feature at Y point with binding energy around 19 meV belongs to a surface

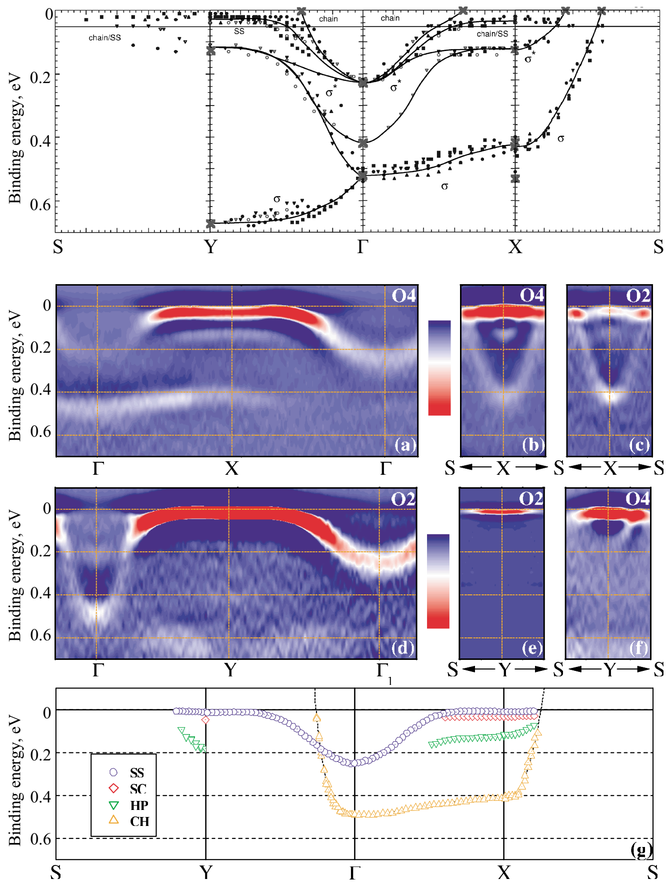

Figure 5.5: Low energy quasiparticle dispersion. The 1st row presents the data after Ref. 185. The band dispersions were extracted from peak positions in single EDC's. σ and $\sigma^\star$ denote the bonding and the antibonding bands respectively. The remaining two rows show the 2nd derivative of the ARPES data after Ref. 189 and the extracted band dispersions. Blue symbols trace the dispersion of the most pronounced feature, which is believed to be a surface state (SS). The other features were identified as superconducting peak (SC), hump (HP) and the chain band (CH).

state that arises from crippled after cleavage chains and, that the antibonding and bonding bands have significantly higher binding energies of about 120 and 660 meV correspondingly. In the more recent work [189], done with significantly improved instrumental resolution, the feature with the highest binding energy was ascribed to the chain states, and, contrary to the two previous investigations, no clear evidence of bilayer splitting was reported.

Work by Lu et al. touches upon another puzzle of Y-123, which is a known problem of clear observation of the superconducting gap. In most of the photoemission studies the gap in the superconducting Y-123 was found to be unusually small or zero [188, 208, 209], notwithstanding the high critical temperature comparable to that of Bi-2212 and contrary to the gap values of $\Delta \sim 30\,\text{meV}$ stemming from tunneling data [210] and Raman scattering experiments [170]. Unlike the mentioned ARPES studies, Schabel et al. [191] based on rather complicated EDC fits reported a sizable and anisotropic gap for ARPES spectra of Y-123. This, however, seems to be at odds with Ref. 189, as in the latter it is believed that the lack of the leading edge gap shift in the k-Fermi EDC is due to the intense feature at the Fermi level, which is most likely a surface state. According to the band structure calculation, that explicitly takes into account the presence of the surface [211], there are indeed several surface states, although the one closest to the FL is 300 meV too deep to prevent the SC gap from being clearly visible in the photoemission spectrum.

Therefore it is clear that before studying more subtle features in the electronic structure of Y-123 it is necessary to ascertain the nature of the low energy features including that of the “surface state”.

5.4 Current results, Fermi surface and overdoping - effects

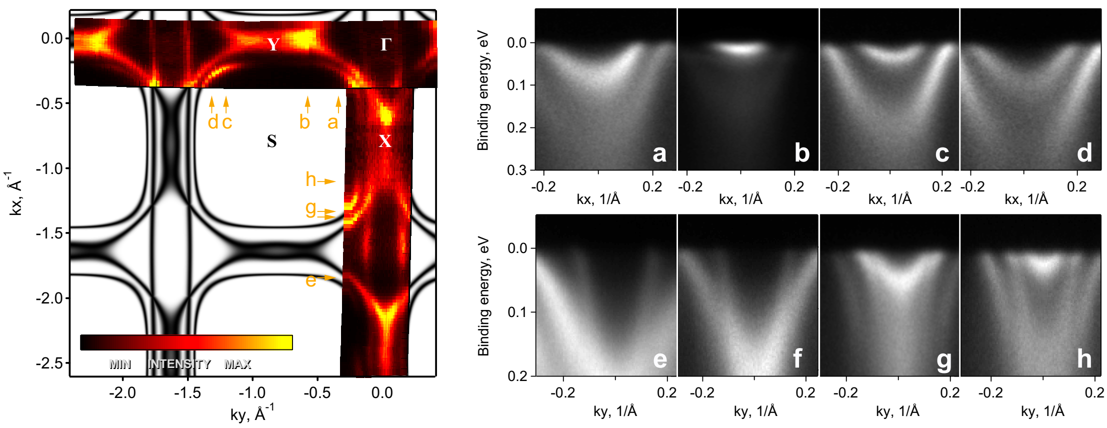

Figure 5.6: Experimental band structure of untwinned $YBa_2Cu_3O_{6.85}$. The left panel contains two experimental FS maps measured along Γ-X and Γ-Y directions and the tight-binding fit to it. (a)–(d), Energy-momentum intensity maps at various k_x values indicated in the FS map. The projection of k_y for these spectra was held constant; its value is denoted by yellow arrows with corresponding lettering on the FS map. (e)–(f), Similar measurements, taken after rotating the sample by 90° around Γ point. The image (e) is the sum of spectra measured with circular polarized light of left and right helicity. The other spectra were measured with linear polarized light.

Based on the data obtained in this research, this subchapter starts with a clarification of certain confusion regarding the experimentally observed electronic structure of the compound that has accumulated in the literature. Fig. 5.6 shows the experimental Fermi surface map of a near optimal doped untwinned $YBa_2Cu_3O_{6.85}$. In contrast to many previous studies, higher excitation energies (50–60 eV vs. 15–30 eV) were used. This enhances the intensity of the Fermi level (FL) crossings of both bonding and antibonding bands and allows one to examine a larger area in k-space. The visual agreement with the band structure calculations [134] is remarkable. There are two hole-like sheets of the Fermi surface centred around the S

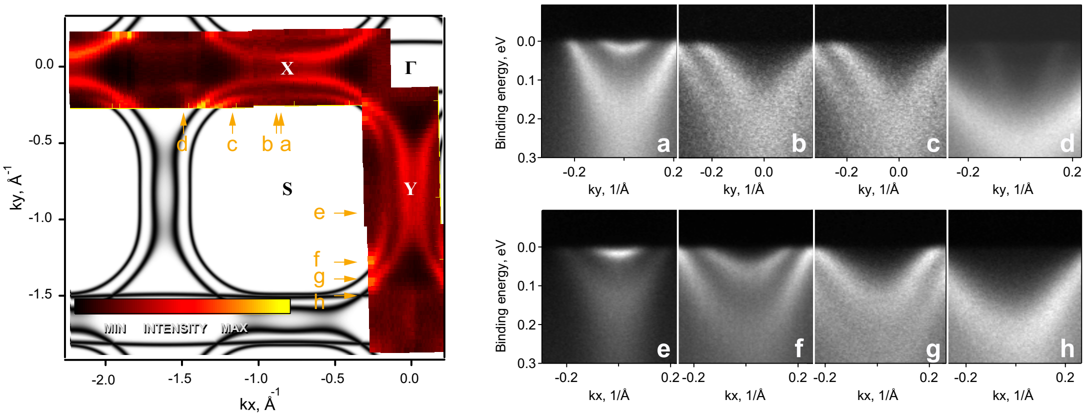

Figure 5.7: Experimental band structure of untwinned $YBa_2Cu_3O_{6.4}$, $T_C = 35$ K. Structure of the figure is analogous to Fig. 5.6. The map and all data images, except for the spectrum given in panel (a), were measured with linear polarized light and $h\nu = 50$ eV. The excitation energy for the image (a) was $h\nu = 55$ eV.

point. A set of one-dimensional features running along the Γ-X direction is a clear indication for the presence of states related to the chain substructure of YBCO-123. Even the form of the antibonding sheet of the FS develops W-like undulations close to the Y point. It is also remarkable that unlike Bi-2212 (ref. [133]) the bilayer splitting along the FS is more isotropic, so that even along the nodal Γ-S cut its value remains comparable to that along the antinodal Y-S cut. To further substantiate the identification of the bands, several typical intensity plots are provided in the panels (a)–(h) of Fig. 5.6. Each of these plots shows the photocurrent intensity as a function of binding energy and momentum along selected directions in k-space with the bright features tracing the band dispersion. Here, in analogy to another bilayer compound Bi-2212, one can follow the typical behaviour of the plane derived bonding and the antibonding bands. The spectra in the panels (e)–(h) show the band dispersion along the k_y-axis, where the one-dimensional chain bands are expected. Indeed, the corresponding parabolic-like band remains unchanged in all four cuts, giving rise to the pairs of lines parallel to the k_x-axis on the Fermi surface map. In image (e) the chain band is enveloped by the antibonding band and part of the bonding band can be seen in the left bottom corner dispersing beyond the image frame. The images (f)–(g) demonstrate how the CuO_2-plane derived bands cross the FL closer and closer to the Γ-X line when moving towards the X point, so that finally the chain band can be found in-between the bonding and antibonding bands. It looks like the relative position of the chain band with respect to the plane bands is not much different from the one predicted by LDA. Thus a good qualitative

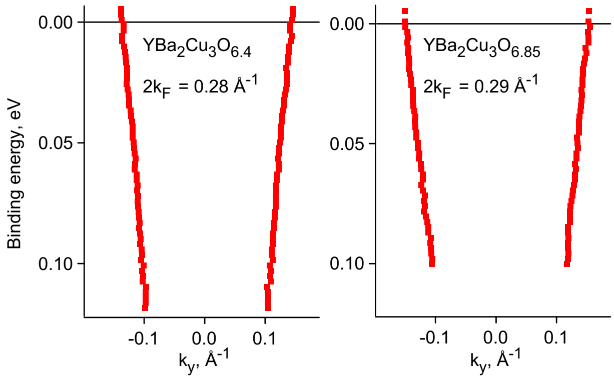

Figure 5.8: Dispersion of the chain band along the k_y direction . Dispersions were extracted using MDC fits of the spectra measured in the vicinity of the 2^{nd} Γ point, i.e. $k_x = \mathrm{const} \approx -1.6$ Å^{-1}, and $T = 30$ K.

agreement between presented data and LDA calculations [134] for the electronic structure of YBCO-123 can be found, although the data do not support the existence of the predicted Ba-O derived pocket centered at the S point.

Similar results were obtained for the samples with various stoichiometries: $YBa_2Cu_3O_{6.9}$, $YBa_2Cu_3O_{6.6}$, $YBa_2Cu_3O_{6.5}$ and $YBa_2Cu_3O_{6.4}$, while for the insulating $YBa_2Cu_3O_{6.0}$ no clear traces of the FS were detected. To complete the picture Fig. 5.7 shows the data for the most underdoped sample $YBa_2Cu_3O_{6.4}$. As one can see, the electronic structure remains qualitatively unchanged, the same bilayer split band and the chain one. The sample turns out to be well untwinned, as follows from the FS map, as well as from comparison of the spectra given in panel (d) and (h) of Fig. 5.7. Comparing the spectra given in Fig. 5.6(e)–(f) to the one plotted in Fig. 5.7(d), it is easy to notice that the chain intensity, measured relative to the plane bands intensity, is weaker for the underdoped sample, which well agrees with the smaller chain filling in the oxygen depleted sample. The chain dispersion is not significantly different between the $YBa_2Cu_3O_{6.4}$ and $YBa_2Cu_3O_{6.85}$ samples, which can be understood in terms of chain oxygen ordering. As long as one chain does not interact strongly with a neighbouring one the chain dispersion will mainly be determined by the interaction within the chain, thus the samples, where either every chain or every second one is filled should display similar chain dispersion, with the exception of the spectrum intensity.

However when trying to detect any signatures of superconductivity no positive conclusions can be made. Estimates of the leading edge gap shift between the nodal and antinodal EDC normally does not result in values greater than about 5 meV for the whole oxygen stoichiometries mentioned above. While for the strongly underdoped $YBa_2Cu_3O_{6.4}$ this can be attributed to very small hole doping level, for the

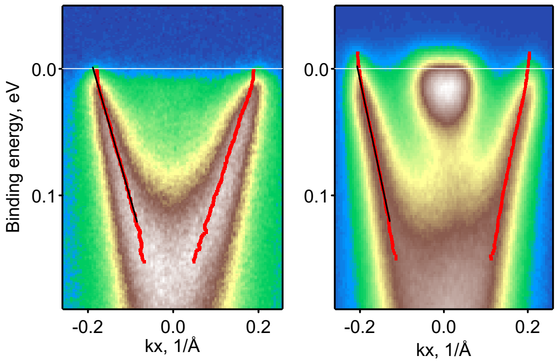

Figure 5.9: Bonding band dispersion for $YBa_2Cu_3O_{6.85}$, spectra measured at $T = 30$ K. The excitation energy and the k_y projection for the 1st and the 2nd image were $h\nu = 50$ eV, $k_y \approx -1.2\pi/a$ and $h\nu = 55$ eV, $k_y \approx 0.7\pi/a$ respectively. The black tilted lines are the guides to eye to, meat to elucidate the weak deviation of the band dispersion (red symbols) from the straight line.

optimally doped $YBa_2Cu_3O_{6.85}$ this is hard to reconcile with the expected superconducting gap of about 30 meV.

Moreover, it is known that in the superconducting state the band dispersion develops a so-called “kink”, a sudden change of the Fermi velocity at the energy range of 50–80 meV. The kink, being relatively mild along the nodal direction of the BZ [117, 183], transforms into a so-called S-shaped dispersion, and finally may split the dispersion into two branches in the vicinity of the antinodal point [69,132]. Again, extracting the MDC dispersion from the spectra measured in the vicinity of the antinodal point (see Fig. 5.9) reveals no kinks in the band dispersion, like if the critical temperature for the sample were below 30 K instead of 90 K.

The partial explanation for this, apparently unusual result, comes from the analysis of the FS area that reflects the hole doping level of the sample region probed in the ARPES measurement. Fitting the experimental FS as described in details in the chapter 2 results in an unusually high doping level regardless of the sample stoichiometry and critical temperature. The results are summarized in the Table 5.4.

As can be seen for the whole range of oxygen stoichiometries the electronic

Sample	T_C, K	$h\nu$, eV	hole doping, x
$YBa_2Cu_3O_{7-\delta}$	92	50	0.30
$YBa_2Cu_3O_{6.85}$	90	50	0.31
$YBa_2Cu_3O_{6.6}$	61	50	0.30
$YBa_2Cu_3O_{6.6}$	61	60	0.30
$YBa_2Cu_3O_{6.4}$	35	50	0.27

Table 5.1: Hole doping levels estimated by the FS area.

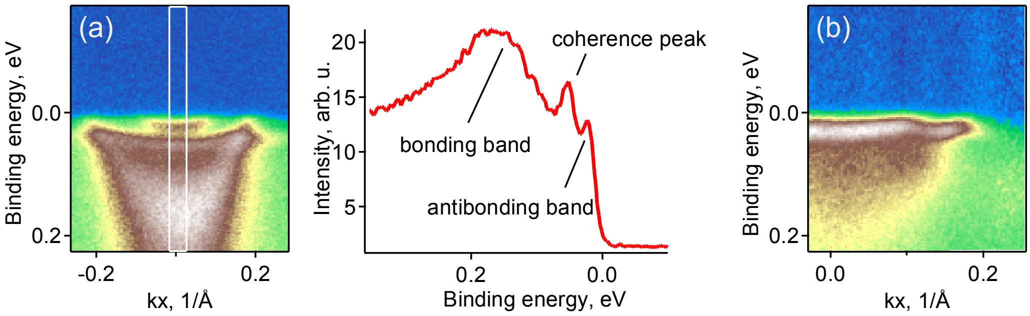

Figure 5.10: (a) Near nodal spectrum of $YBa_2Cu_3O_{6.85}$ that contains an additional flat feature and the EDC extracted from the spectrum; the momentum integration window being denoted by the white rectangle. (b) Comparison to a spectrum of Bi-2212 in the superconducting state, when the bonding and antibonding bands merge into a flat non-dispersing feature.

structure seen by the ARPES surface turns out to be extremely overdoped as compared to the bulk doping level. Probably only for the $YBa_2Cu_3O_{6.4}$ one could expect a tiny superconducting gap allowing for some deviation from the universal doping parabola [212].

However it is necessary to mention that ARPES on Y-123 is not limited only to the overdoped spectra. At certain excitation energy and experimental geometry there can appear additional almost non-dispersing feature (Fig. 5.10) in the vicinity of the $(\pi, 0)$ point. The general shape of the feature is reminiscent of the superconducting spectrum of Bi-2212 [Fig. 5.10 (b)], where the spectral weight is confined by the superconducting gap at lower binding energies and by the coupling to collective mode at higher binding energies, which hints that the feature might be the true superconducting spectrum with a corresponding nominal doping level. More rigorous reasoning to consider the flat feature in the spectra as the one arising from the superconducting component, as well as considerations on account of the origin of the overdoping effect and its spatial localization will be given in the following subchapters.

5.5 Superconducting component. Dependence on temperature and photon energy

Although visually the spectrum looks like a superposition of the non-superconducting bands, carrying no signatures of superconductivity, with the feature that reminds a spectral distribution that is normally observed in the superconducting state, the only visual resemblance is not enough for strict identification

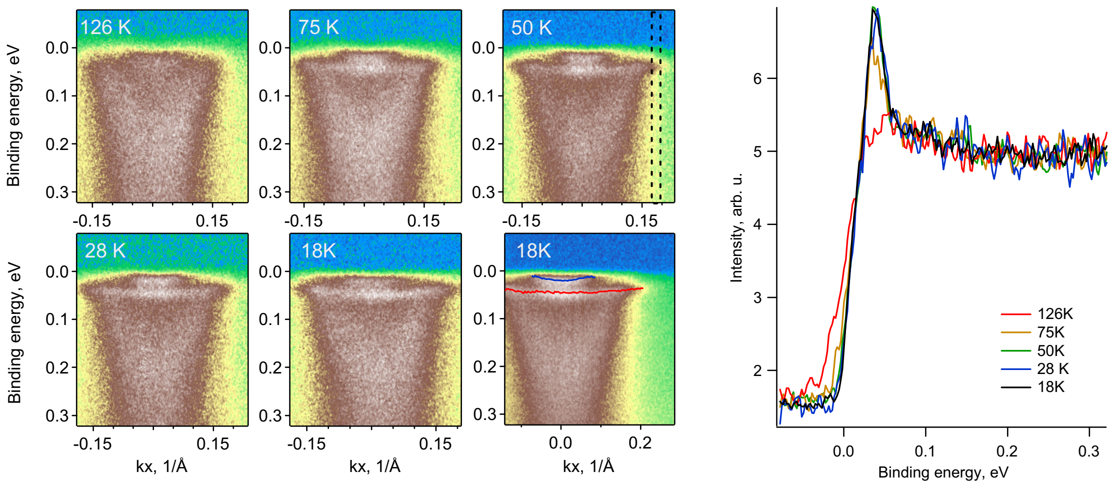

Figure 5.11: Temperature dependence of the superconducting feature for $YBa_2Cu_3O_{6.9}$. The right hand image shows evolution of the EDC's integrated in a small momentum window. The integration range is shown by a dashed rectangle plotted on top of the 50 K spectrum. The blue and the red curves in the 18 K show the peak dispersion of the overdoped antibonding band and the superconducting feature.

of the flat feature as a superconducting component. More solid evidence can be extracted from its dependence on temperature and excitation energy.

Figure 5.11 gives the typical temperature dependence of the spectral weight measured for the twinned $YBa_2Cu_3O_{6.9}$ sample, $T_C \approx 90\,\mathrm{K}$. As can be seen the feature remains persistent at all temperatures below T_C, but at 126 K it is completely gone. More clearly this dependence can be traced from the EDC's plotted in the rightmost panel of Fig. 5.11. The EDC's are the result of integration over momentum in a small window, which is shown in the 50 K panel. It can be seen that for all temperatures below T_C there is clearly observable a so-called "pile up" or superconducting peak [118], while for temperatures above T_C the peak completely vanishes, which is a typical behaviour of the spectral lineshape of HTSC.

Another evidence to consider the flat feature seen in the ARPES spectra as the one originating from the superconducting component with nominal doping level can be drawn from the dependence of the near-antinodal spectra on excitation energy. The corresponding experimental data is shown in Fig. 5.12. One can notice that, for the spectrum measured with $h\nu = 50\,\mathrm{eV}$ the antibonding band of the overdoped component is strongly enhanced. The same happens to the central part of the feature, supporting the idea that it should be a similar parabolic band, with the difference that it is modified by the BCS-like bending due to the presence of the superconducting gap. The lower position of the band bottom, is also consistent

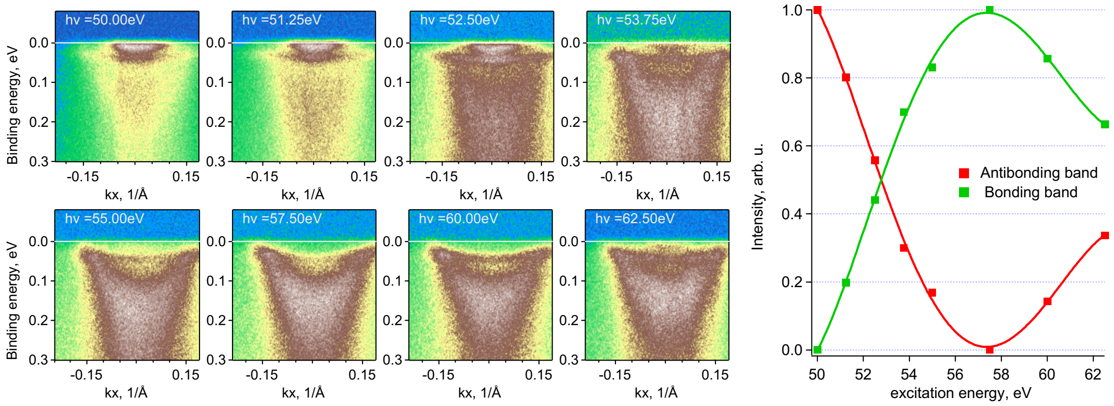

Figure 5.12: Dependence of the photoemission matrix elements on excitation energy. All images contain a mixture of the overdoped and superconducting components. The right graph shows the relative intensities of the bonding and antibonding bands, assuming the overdoped and superconducting components have close excitation energy dependence.

with the fact that the superconducting component (the feature) corresponds to a plane-derived band with a lower hole doping level.

For $h\nu = 55$ or 60 eV, on the opposite, the bonding band is strongly enhanced. We see that the outer part of the superconducting feature follows the same trend. Along with the intensity variations one can notice the signatures of kinks that are normally observed in spectra of superconducting Bi-2212 [69–72] and branching effects [68, 119, 213, 214] that give rise to a non-vanishing flat stripe of spectral weight at binding energy of about 50 meV.

In other words, the feature behaves as like its intensity is due to the gapped bonding and antibonding bands, that have matrix elements similar to their overdoped and hence ungapped counterparts. Similar dependence of the matrix elements on the excitation energy for the superconducting and overdoped bands is not an exception but rather a rule, which can be easily understood, as the dependence is manly determined by the symmetry of bands along the c axis with respect to the midpoint between the two CuO_2 planes [215]. Therefore this fact can be used to test that the feature and the overdoped plane bands are really cognate, i.e. derived from the same orbitals, but due to substantially higher doping level (one reason for this could be inhomogeneous doping) the overdoped component does not develop superconductivity.

Using the language of formulae and the above mentioned assertion, the total photocurrent intensity can be written as

$$\begin{aligned} I(k_x,\omega) = \mu_{\mathrm{BB}}(h\nu)\left[M^{\mathrm{OD}}_{\mathrm{BB}}(k_x,\omega)A^{\mathrm{OD}}_{\mathrm{BB}}(k_x,\omega)+M^{\mathrm{SC}}_{\mathrm{BB}}(k_x,\omega)A^{\mathrm{SC}}_{\mathrm{BB}}(k_x,\omega)\right] \\ +\mu_{\mathrm{AB}}(h\nu)\left[M^{\mathrm{OD}}_{\mathrm{AB}}(k_x,\omega)A^{\mathrm{OD}}_{\mathrm{AB}}(k_x,\omega)+M^{\mathrm{SC}}_{\mathrm{AB}}(k_x,\omega)A^{\mathrm{SC}}_{\mathrm{AB}}(k_x,\omega)\right] \\ \equiv \mu_{\mathrm{AB}}(h\nu)\,I_{\mathrm{AB}}(k_x,\omega)+\mu_{\mathrm{BB}}(h\nu)\,I_{\mathrm{BB}}(k_x,\omega). \end{aligned} \tag{5.1}$$

Here $A^{\cdot\cdot}_{\cdot\cdot}(k_x,\omega)$ is a spectral function, coefficient $M^{\cdot\cdot}_{\cdot\cdot}(k_x,\omega)$ accounts for a possible dependence of the matrix elements on momentum k_x and on the binding energy ω, as well as on the other parameters such as polarization and the angle at which the light enters the crystal.[†] Coefficients $\mu_{\cdot\cdot}$ give the dependence of the matrix element on the excitation energy. 'AB', 'BB', 'OD', 'SC' are the abbreviations for the antibonding, bonding, overdoped and superconducting bands, respectively.

As long as the above described assumption holds, it should be possible to express any spectrum as a linear combination of some two "basis" spectra that have different admixture of the bonding and antibonding bands. On practice, it is convenient to choose for the "basis" those spectra, which are the closest to $I_{\mathrm{AB}}(k_x,\omega)$ and $I_{\mathrm{BB}}(k_x,\omega)$, as in that case the coefficients in the linear combination would give the excitation energy dependence of the matrix elements $\mu_{\mathrm{AB}}(h\nu)$ and $\mu_{\mathrm{BB}}(h\nu)$.

To test the assumption, the spectra measured with excitation energy $h\nu = 50.0\,\mathrm{eV}$ and $h\nu = 57.5\,\mathrm{eV}$ were taken for the basis ones, and the spectra measured with the other excitation energies (see Fig. 5.12) were approximated using (5.1). The criterion for the optimal values of $\mu_{\mathrm{AB}}(h\nu)$ and $\mu_{\mathrm{BB}}(h\nu)$ was the minimal value of the following weighed error function

$$\chi = \sum_{\{k,\omega\}} \frac{[I^2(k,\omega)-\mu_{\mathrm{AB}}(h\nu)\,I_{\mathrm{AB}}(k,\omega)-\mu_{\mathrm{BB}}(h\nu)\,I_{\mathrm{BB}}(k,\omega)]^2}{I^2(k,\omega)}. \tag{5.2}$$

The assertion really stands the check as the χ remains below 0.015 – 0.020, and the difference between the true spectrum and the approximating linear combination practically reveals no structure.

Thus this provides another evidence to consider the spectra shown in Figs. 5.12, 5.1 as a superposition of the nominally doped and overdoped plane derived bonding

---

[†] As for the currently discussed spectra the polarization and the incidence angle of the light were the same, these factors are not explicitly stated in the formula. Nonetheless, matrix elements for the overdoped and superconducting components may have completely different dependence on these parameters, which makes it possible to enhance the superconducting component with respect to the overdoped one.

and antibonding band. As a by-product the procedure applied above also gives the dependence of the matrix elements on the excitation energy see (Fig. 5.12). It is also worth to notice that the above presented way to estimate the dependence of matrix elements on excitation energy is preferable to the usual way used in Ref. 131, as in this case the whole data set is used, and finding the coefficients $\mu_{AB}(h\nu)$ and $\mu_{BB}(h\nu)$ does not require iterative fitting of the peaks in EDC with a model function.[†]

5.6 Cleavage problem and overdoping effects

In the previous sections it was shown that neither for the nearly optimally doped sample ($YBa_2Cu_3O_{6.85}$) nor for the moderately underdoped one ($YBa_2Cu_3O_{6.6}$) was it possible to detect easily any evidence of the superconductivity like a sizable gap or strong kinks in the vicinity of the antinodal points. Instead, the spectra were dominated by a strongly overdoped component.

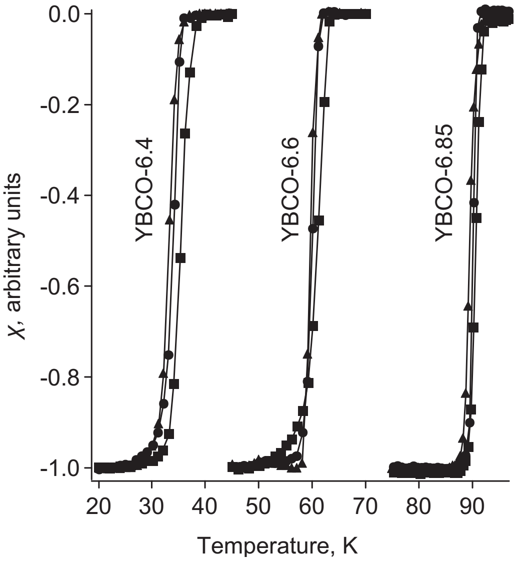

Figure 5.13: T_C curves for $YBa_2Cu_3O_{6.4}$, $YBa_2Cu_3O_{6.6}$ and $YBa_2Cu_3O_{6.85}$. Curves ▲, ●, and ■ demonstrate the spread of T_C among the samples of the same stoichiometry. Data courtesy V. Hinkov.

The first tentative explanation for this could be that the doping level of the samples is spatially inhomogeneous, and due to the unfavourable conditions only the overdoped region was picked up in the measurements. Along with the incredibility of such an event another, more substantial, reason could be produced to dismiss such a hypothesis. Strong inhomogeneities would mean that the critical temperature varies from something about 0 K, that corresponds to huge overdoping, to the value of 92 K, the temperature corresponding to optimal doping level. This is completely inconsistent with the narrow transition temperatures for the samples which do not exceed 1–3 K. Continuous variation of the doping level, which is to be expected in case of nonuniform oxygen distribution, would also imply that the band structure should vary continuously between the overdoped and underdoped cases. This, in turn, would entail spectra that are smeared between

---

[†] The minimum condition for the χ can be written as $\partial\chi/\partial\mu_{AB}(h\nu) = 0$ and $\partial\chi/\partial\mu_{BB}(h\nu) = 0$, which yields just a set of two linear equations with respect to $\mu_{AB}(h\nu)$ and μ_{BB}.

the two limiting cases, which is again not supported by the experimental observation, when primarily the overdoped spectra (Fig. 5.6), or the spectra with two fixed dopings are observed (Figs. 5.11, 5.12). Thus some other reasons different from inhomogeneous doping are responsible for the observed spectra.

Already in the early ARPES measurements [149, 208] it was noticed that there are practically no difference between the spectra measured for the oxygen doping range $6.4 < 7-\delta < 6.9$, which might result from a heavy overdoping of the exposed after the cleavage surface [187]. Unlike Bi-2212, that cleaves between the two Bi–O layer weakly bound by van der Waals force, Y-123 does not have such a natural cleavage plane. The numerous indirect studies suggest that the Y-123 does not seem to have a stable cleavage plane [216–218], although according to tunneling studies the cleavage between the Cu–O and Ba–O layers is the most preferable one. The first evidence for this type of cleavage to be the most probable comes form the works by Edwards et al. [210]. Comparing experimentally observed step heights (either a unit cell high $c \approx 12$ Å or 4 Å) in the topography images of cleaved surfaces with the known interlayer distances in Y-123 structure [147, 219] the authors came to a conclusion that only the interface between Ba–O and Cu–O layers fits the experimental data. The most convincing evidence comes from the recent tunneling experiments with good atomic resolution. The figure 5.14 (a)–(b) shows the topography image of the two complementary parts of the Y-123 crystal cleaved at low temperature. While one of the parts displays tetragonal symmetry in the atoms arrangement, the other one clearly reveals one-dimensional character. Again looking at the crystal structure (Fig. 5.1) it is easy to find that this is possible only for the aforementioned cleavage interface. In the measurements done by Maki et al. [220] one can discern two sublattices at the surface with tetragonal symmetry, such that the vertices of one sublattice are located in the square centers of the other lattice, which is possible only for the Ba–O layer.

An interesting and seemingly important factor is the temperature at which the crystal is cleaved. In the early photoemission study of $EuBa_2Cu_3O_{7-x}$ by List et al. [222] an irreversible loss of emission was reported, if the sample is ever heated above 80 K. This was interpreted as a massive loss of oxygen by the cleaved sample. Therefore in numerous later tunneling [210, 220, 223, 224] and photoemission [149, 188–190] studies the samples were never heated above the 20–40 K as only in that way the original structure of the cleaved surface could be preserved.

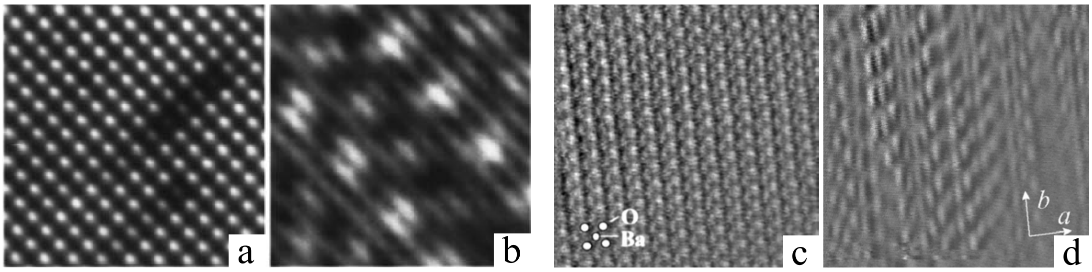

Figure 5.14: STM images of cleaved Y-123 surfaces. (a), (b) The two complementary parts of the cleaved crystal, the image size is 50 Å× 50 Å. The data after Pan et al. [221]. (c), (d) Similar experiment by Maki et al. [220], the image size is 55 Å× 55 Å. The image of the Ba–O plane clearly shows the two types of atoms.

For the tunneling the vacuum conditions are of the major importance, as any absorbed atoms would change what is found under the tip, thus it is no wonder that the atomic resolution might be lost after heating the sample, when the strong degassing is hardly avoidable. However, for the photoemission the problem does not seem to be so acute as described in [222], provided that the reasonable vacuum conditions ($p \lesssim 3 \cdot 10^{-10}$ mBar) are preserved in the experimental chamber. From the temperature dependence (Fig. 5.11) measured while cooling down the sample it can be concluded that there is no irreversible loss of spectral weight, and that all features are nicely returning to what has been seen at low temperatures before heating. It was also tried to cleave samples at room temperature and then cool down to 20 K, as well as measure the spectra from samples that were cleaved at 20 K. No notable difference was found between these two cases. Only a prolonged (about 24 h) stay of the surface in the vacuum chamber led to notable broadening of the spectral features due to scattering of the photo electrons on the adsorbed residual gas atoms. The spectra sharpness could be partially recovered after heating the cleaved surface to room temperature and cooling back again, which obviously allowed one to “shake off” some of the adsorbed atoms. Therefore the gradual loss of the oxygen by the cleaved surface seems to be unlikely.

As it can be intuitively expected and supported by the calculations [211], the cleavage between Cu–O and Ba–O layers would not substantially modify the generic bonding and antibonding bands [211], whose wave functions are localized in the CuO_2 bilayer, however the doping level determined by the chain block over which the cleavage took place cannot remain unaffected. So the reason for the overdoped spectra observed in ARPES data is charge redistribution at the cleaved surface, more precisely at the nearest to the surface bilayer. The next bilayer is unlikely to change

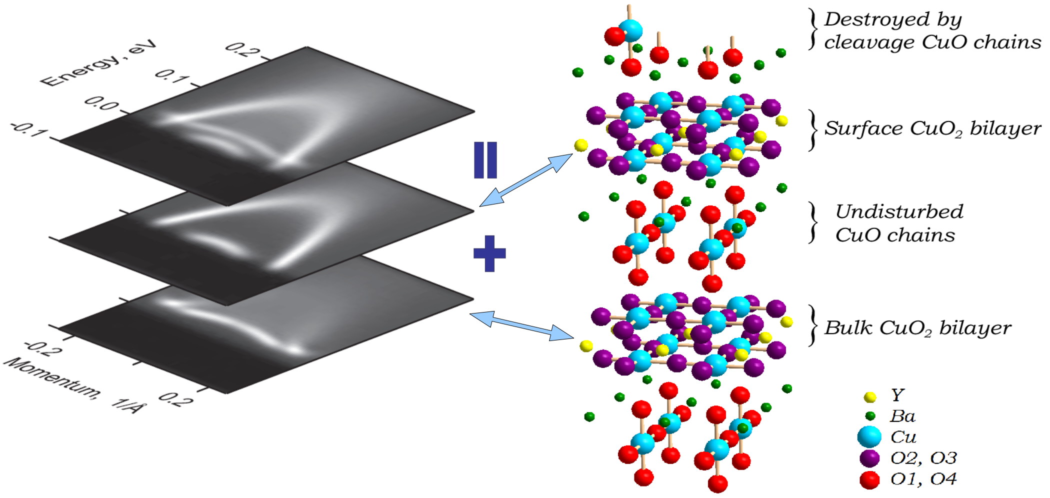

Figure 5.15: Localization of the overdoped and nominally doped components at the topmost and the next bilayers respectively. The left part of the Figure shows the corresponding model spectrum as a superposition of the overdoped and nominally doped spectra.

its doping level as the chains structure on its both sides remain untouched. This also naturally explains why the superconducting feature is generally much weaker as compared to the overdoped one, which is localized in the nearest to the surface bilayer. Schematically the situation can be illustrated by the Fig. 5.15. Further evidence for such arrangement of the overdoped and nominally doped components will be given in the next section.

5.7 Circular dichroism

In the previous subchapter it was argued that the overdoped component is localized in the near surface plane, while the states, whose doping correspond to the bulk one are located in the deeper layers below the cleavage surface. Although the overdoped and superconducting components have similar dependence of the matrix elements on the excitation energy they are not indistinguishable. Here it will be shown that owing to a different spatial localization of the two components and the different pattern of the electromagnetic field there will be a notable difference between the matrix elements that leads to appearance of circular dichroism for the component located at the surface. This particular effect, observed experimentally can be used as another argument against lateral inhomogeneity in the charge doping level, and in favour of doping variation along the normal to the surface.

Frequently, when estimating the photoemission matrix elements using Fermi golden rule [20]:

$$w_{\mathrm{i}\to\mathrm{f}} \sim \frac{2\pi}{\hbar}\left|\langle f|\hat{H}_{\mathrm{pert}}|i\rangle\right|^2 \delta(E_{\mathrm{f}} - E_{\mathrm{i}} - \hbar\omega), \tag{5.3}$$

the term div**A** in the perturbation to the Hamiltonian is neglected $\hat{H}_{\mathrm{pert}} = -\frac{ei\hbar}{mc}(\mathbf{A}\nabla + \frac{1}{2}\,\mathrm{div}\mathbf{A})$. Yet, for the particular case that we are dealing with, the major part of the signal comes from the near surface region [28, 29], thus the surface effects need to be properly accounted for.

The essential reason that makes the surface emission different from the bulk emission is the presence of the near surface induced electromagnetic fields arising from the mismatch in the dielectric constant between the solid and vacuum. The depth down to which the term div**A** modifies the matrix elements depends on the particular field pattern near the surface, exact microscopic calculation of which turns out to be a very difficult task. Nevertheless, a basic insight can be obtained considering a relatively simple jellium model. Employed to describe a free electron metal [225], the model shows that the vector potential of the electromagnetic wave $\mathbf{A}(\mathbf{r})$ experiences quickly decaying Friedel-like oscillations with a characteristic scale of a few angstroms. In a more recent study of TiS_2, which is closer to the case of superconducting cuprates, the layered structure of the crystal was taken into account [226]. From this study follows that rapid changes that $\mathbf{A}(\mathbf{r})$ undergoes are happening within a thin surface layer with characteristic thickness d_{surf} of about one unit cell along the normal to the surface, which is qualitatively a general picture that would follow from any microscopic model. To estimate the photoemission matrix element for the circularly polarized light, similar to Pforte et al. [227], the vector potential is considered to change linearly from its vacuum to bulk value within the surface layer of thickness d_{surf} as demonstrated in Fig. 5.16 (b).

Obviously the final result depends on the particular details of the experimental geometry. The angles and the mutual arrangement of the sample, excited electrons and the incident light are introduced in Fig. 5.17. Unlike the general case described in Figs. 3.7 and 3.8 the tilt angle α is kept zero, the angle $\beta - \varphi$ determines the light incidence angle. It is convenient to represent the incident circularly polarized wave $\mathbf{A}(\mathbf{r})$ as a sum of the two plane polarized waves with a phase shift of $\pi/2$:

$$\mathbf{A}(\mathbf{r}) = \mathbf{A}_{\mathrm{C}}\cos(\omega t - \mathbf{q}\mathbf{r}) + \mathbf{A}_{\mathrm{S}}\sin(\omega t - \mathbf{q}\mathbf{r}), \tag{5.4}$$

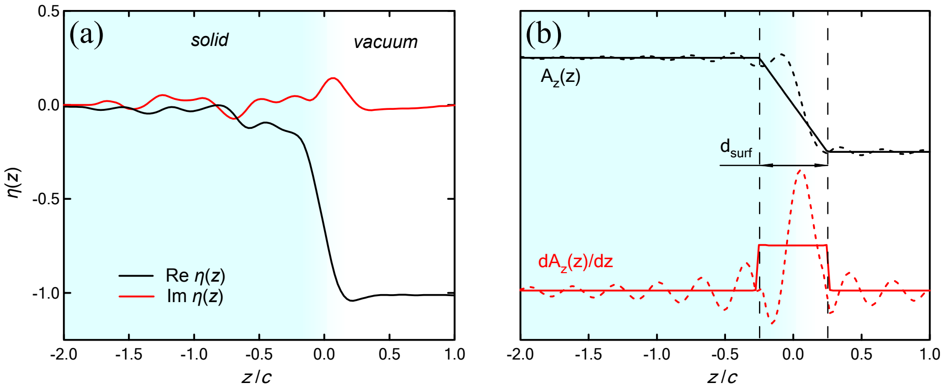

Figure 5.16: (a) Typical field oscillations at the solid-vacuum interface, $\eta(z) = (E_z(z,\omega) - E_z^{\text{bulk}}(z,\omega))/(D_z(\omega) - E_z^{\text{bulk}}(z,\omega))$ is a normalized difference of the longitudinal electric wave field. Calculation for TiS_2 [226]. (b) Simplified model for the field variation at the interface used to estimate the matrix element. Dashed curves give the "true" variation of the normal to the interface z component of the vector potential and its derivative. The solid curve is the model dependence used instead.

than it can be shown that for such a superposition of periodic perturbations

$$\begin{aligned} w_{\text{i}\to\text{f}} &\sim \frac{2\pi}{\hbar}\left|\langle f|\hat{V}_\text{C} - i\hat{V}_\text{S}|i\rangle\right|^2, \text{ where} \\ \hat{V}_\text{C,S} &= -\frac{ei\hbar}{mc}(\mathbf{A}_\text{C,S}\nabla + \frac{1}{2}\,\text{div}\mathbf{A}_\text{C,S}). \end{aligned} \tag{5.5}$$

At this stage the particular pattern of the near surface induced field comes into play. Macroscopically, from the continuity condition for the components of **D** and **E** vectors one has:

$$\begin{aligned} \mathbf{E}_{\|}^{\text{vacuum}} &= \mathbf{E}_{\|}^{\text{sample}}, \\ \mathbf{E}_{\perp}^{\text{vacuum}} = \mathbf{D}_{\perp}^{\text{vacuum}} &= \mathbf{D}_{\perp}^{\text{sample}} = \varepsilon\mathbf{E}_{\perp}^{\text{sample}}, \end{aligned} \tag{5.6}$$

where the subscripts $\|/\perp$ indicate vector components parallel/perpendicular to the sample surface, and ε is the sample permeability. Using the gauge with the scalar potential of the electromagnetic field taken to be zero, the last equation can be rewritten as:

$$\mathbf{A}_{\|}^{\text{vacuum}} = \mathbf{A}_{\|}^{\text{sample}}, \;\; \mathbf{A}_{\perp}^{\text{vacuum}} = \varepsilon\mathbf{A}_{\perp}^{\text{sample}}. \tag{5.7}$$

Microscopically, as has previously been pointed out, the jump in the vector potential appears as a smooth transition with a spatial extension d_surf of about one lattice parameter c, within which the vector potential $\mathbf{A}(\mathbf{r})$ changes from its vacuum value to the bulk one. For the discussed geometry $\text{div}\mathbf{A}_\text{S} = 0$ due to the boundary conditions, and div$\mathbf{A}_\mathrm{C}$ can be approximated as:

$$\begin{aligned}\mathrm{div}\mathbf{A}_\mathrm{C} &\approx \frac{|\mathbf{A}_\perp^\mathrm{sample} - \mathbf{A}_\perp^\mathrm{vacuum}|}{d_\mathrm{surf}} = \frac{(1/\varepsilon - 1)|\mathbf{A}_\perp^\mathrm{vacuum}|}{d_\mathrm{surf}} \\ &= C|\mathbf{A}_\perp^\mathrm{vacuum}| = C|\mathbf{A}_\mathrm{C}|\sin(\beta - \varphi),\end{aligned} \tag{5.8}$$

where C is a complex constant that effectively accounts for the width of the transition layer and for the sample permeability.

To estimate the matrix element (5.3) we assume that the final state is a plane wave: $|f\rangle = |e^{i\mathbf{kr}}\rangle$, with $\mathbf{k}$ being the quasimomentum of the excited photoelectron. Leaving out the irrelevant coefficients yields:

$$\begin{aligned}w_{\mathrm{i}\to\mathrm{f}} &\sim \left|\langle i|\mathbf{A}_\mathrm{C}\nabla + \frac{1}{2}\,\mathrm{div}\mathbf{A}_\mathrm{C} - i\mathbf{A}_\mathrm{S}\nabla|e^{i\mathbf{kr}}\rangle\right|^2 \\ &= \left|\langle i|e^{i\mathbf{kr}}\rangle\right|^2\left|\mathbf{A}_\mathrm{C}i\mathbf{k} + \mathbf{A}_\mathrm{S}\mathbf{k} + \frac{1}{2}\,\mathrm{div}\mathbf{A}_\mathrm{C}\right|^2.\end{aligned} \tag{5.9}$$

To get the matrix element for the opposite circular polarization one just needs to reverse the direction of the vector $\mathbf{A}_\mathrm{S}$, therefore for the dichroism we obtain:

$$\begin{aligned}D \equiv dw_{\mathrm{i}\to\mathrm{f}}^\mathrm{cr} - dw_{\mathrm{i}\to\mathrm{f}}^\mathrm{cl} \sim \left|\langle i|e^{i\mathbf{kr}}\rangle\right|^2\Big\{\Big|\mathbf{A}_\mathrm{C}i\mathbf{k} + \mathbf{A}_\mathrm{S}\mathbf{k} \\ + \frac{1}{2}\,\mathrm{div}\mathbf{A}_\mathrm{C}\Big|^2 - \left|\mathbf{A}_\mathrm{C}i\mathbf{k} - \mathbf{A}_\mathrm{S}\mathbf{k} + \frac{1}{2}\,\mathrm{div}\mathbf{A}_\mathrm{C}\right|^2\Big\}.\end{aligned} \tag{5.10}$$

Since $|\mathbf{A}_\mathrm{C}i\mathbf{k} - \mathbf{A}_\mathrm{S}\mathbf{k}| = |\mathbf{A}_\mathrm{C}i\mathbf{k} + \mathbf{A}_\mathrm{S}\mathbf{k}|$ there will be no circular dichroism if div$\mathbf{A}_\mathrm{C}$ equals zero. It is worth to mention that this is a rather general statement, which is true for any geometry as long as the final states can be well approximated by the plane waves [228]. As pointed out in the Ref. 36 the deviation of the final states from plane waves might be considerable for low kinetic energies ($\lesssim$ 10 eV), hence leading to possible circular dichroism. Nonetheless, for the energy range that we are using the free electron approximation is well justified [33, 229] and the dichroism due to non-plane wave character of final states can be excluded.

After simple computations, taking into account the experimental geometry, the expression (5.10) reduces to the final form that we are going to use:

$$D \sim \left|\langle i|e^{i\mathbf{kr}}\rangle\right|^2 \mathrm{Re}(C)|\mathbf{A}_\mathrm{C}||\mathbf{A}_\mathrm{S}||\mathbf{k}|\sin(\eta)\sin(\beta - \varphi). \tag{5.11}$$

An important consequence of this formula is that in the described geometry the photoemission signal arising from the near surface region would exhibit circular dichroism proportional to $\sin(\eta) \approx \eta$. It is this particularity that can be used to distinguish the contribution to the spectrum arising from the near surface layer, where

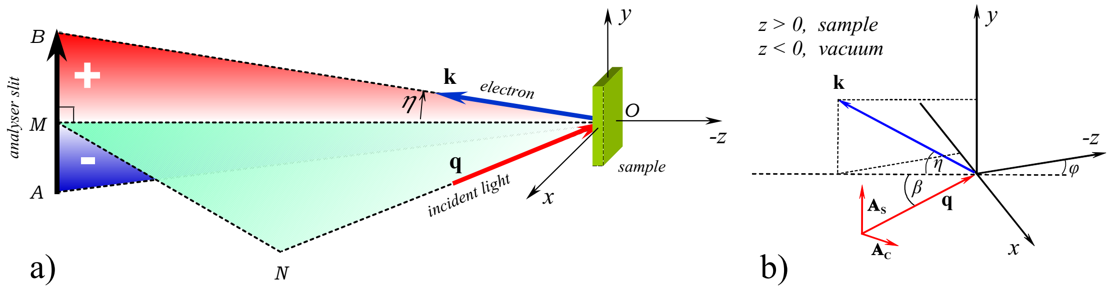

Figure 5.17: (a) Sign of the circular dichroism as a function of the analyser angle η for the geometry used in the experiment. The red-white-blue scale denotes the strength and the sign of the dichroism. (b) Mutual arrangement of the sample (after being rotated by angle φ around y axis), the wave vector of the incident light $\mathbf{q}$ and the wave vector of the emitted photoelectron $\mathbf{k}$. The circularly polarized wave is represented as a sum of two plane ones with a polarization vectors $\mathbf{A}_S$ and $\mathbf{A}_C$.

the term with div $\mathbf{A}$ is important, from the one coming from the deeper regions of the sample. Representing 2D ARPES spectra as a sum of a "bulk" and the "surface" component we can write:

$$\begin{aligned} I^{\mathrm{cl}}(\eta,\omega) &= I^{\mathrm{bulk}}(\eta,\omega) + I^{\mathrm{surf}}(\eta,\omega)(1+\alpha\eta), \\ I^{\mathrm{cr}}(\eta,\omega) &= I^{\mathrm{bulk}}(\eta,\omega) + I^{\mathrm{surf}}(\eta,\omega)(1-\alpha\eta), \end{aligned} \tag{5.12}$$

where α accounts for the dichroism strength. The constituent bulk and surface related components can easily be obtained:

$$\begin{aligned} I^{\mathrm{surf}}(\eta,\omega) &= \frac{1}{2\alpha\eta}(I^{\mathrm{cl}}(\eta,\omega) - I^{\mathrm{cr}}(\eta,\omega)), \\ I^{\mathrm{bulk}}(\eta,\omega) &= \frac{1}{2}(I^{\mathrm{cl}}(\eta,\omega) + I^{\mathrm{cr}}(\eta,\omega)) - I^{\mathrm{surf}}(\eta,\omega). \end{aligned} \tag{5.13}$$

Figure 5.18 demonstrates how the derived formulae can be applied to the experimental data. The row (a) treats the spectra where the overdoped antibonding and chain bands are contributing. As can be seen from the difference image there is practically no dichroism on the chain band as compared to the overdoped antibonding band. This means that the antibonding states are localized in the region with significant div $\mathbf{A}$. On the other hand the remnants of chains at the very cleaved surface are heavily disrupted to result in a photoemission signal that reminds the bulk dispersion, so the signal of chain band observed in the spectrum should come from the next undisturbed chain block (see Fig. 5.15). The fact that there is practically no dichroism on the chain band suggests that the first undisturbed chain block is already out of the near surface region with significant div $\mathbf{A}$. This also means that the next CuO_2 bilayer, the one which is expected to be superconducting, should be out

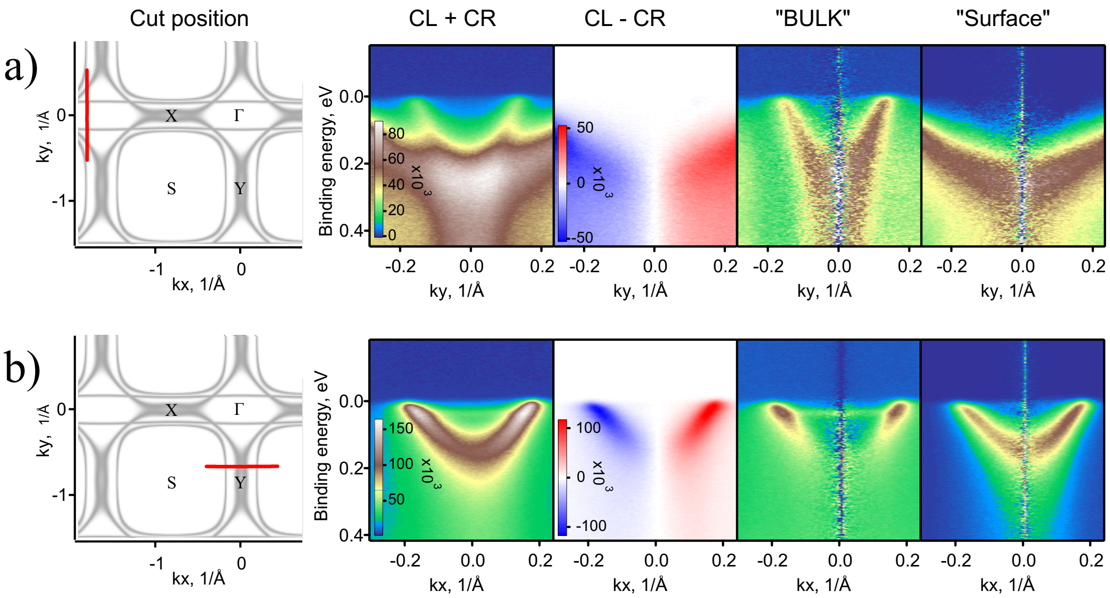

Figure 5.18: (a, b) Panels from left to right: position of the energy-momentum cuts in the reciprocal space; sum of the spectra measured with opposite circular polarizations; their difference; extracted bulk component; extracted surface component. Colour scale bars show the absolute intensity. In the block (a) the process of disentangling the surface related antibonding band and the chain band is demonstrated ($h\nu = 50\,\text{eV}$, $k_x^{\text{slit}} \approx -1.82\,\text{Å}^{-1}$). Block (b) depicts the same procedure, but for the surface and bulk components of the bonding band ($h\nu = 55\,\text{eV}$, $k_y^{\text{slit}} \approx -0.70\,\text{Å}^{-1}$). The antibonding band in this case is suppressed by the unfavourable matrix elements.

of that region and display no dichroism. Indeed, splitting the spectrum of the overdoped bonding band (Fig. 5.18 b) into the surface and the bulk components one can see that the surface component reminds the spectrum measured in the normal state above T_C, exhibiting no signatures of renormalization. The spectrum of the bulk component looks qualitatively different. The strong band renormalization and branching effects [69, 72, 117], which are known signatures of superconductivity, are clearly visible in the spectrum supporting the expectation.

Although the use of circularly polarized light helps to elucidate the spatial localization of the overdoped and superconducting components, as well as allows for disentangling of the two spectra, one should not forget that such disentangling is not 100% complete; the reason being a rather crude model (Fig. 5.16) used to describe the light field at the cleaved interface.

5.8 Superconducting gap and anisotropic renormalization in Ca-doped Y-123

To further explore the properties of the superconducting component we studied partially Ca-substituted YBCO-123 samples. In Fig. 5.19 spectra for $(\mathrm{Ca}_x\mathrm{Y}_{1-x})\mathrm{BaCu}_3\mathrm{O}_{7-\delta}$, ($x$=0.15±0.03) are shown, where the superconducting component dominates. The samples were initially grown for INS scattering experiments and the amount of substituted Ca was a compromise between the quality of the samples and the effect of Ca atoms on the doping level. In panels (a)–(e) one can directly observe the momentum dependence of the leading edge gap (LEG) value with its anisotropic character consistent with d-wave symmetry. The temperature evolution of the gap is given in Fig. 5.19 (f)–(j) and leaves no doubt as to the superconducting nature of these spectra. A very important observation here is the occurrence of renormalization anomalies in the band dispersion and their strong momentum and temperature dependence. It is notable that there are practically no renormalization effects due to the mode coupling for the overdoped component. Comparing the spectra for the overdoped component given in Fig. 5.9 one immediately notes a direct relation between the doping level and the strength/presence of the renormalization. It is these dependencies that were used to argue that the reason for the unusual renormalization effect in Bi-2212 is the coupling to magnetic excitations [121, 132], as it is unlikely to expect such a strong dependence for the coupling to a phonon mode.

In Fig 5.19 (c)–(d) one can also notice that the strong renormalization in the vicinity of the $(\pi, 0)$ point results in the suppression of the spectral weight at certain energy, so that single EDC's extracted from these images would develop a so-called peak-dip-hump line shape. Here it has to be stressed that this line shape in this particular energy is a true many body effect, and not a trivial superposition of the bilayer split band, which is supported by the dependence of the photoemission matrix elements on the excitation energy presented in Fig. 5.12. As can be seen the admixture of the bonding band for this particular energy is negligible and cannot give rise to a hump in the spectrum. According to the spin fluctuation theory [74, 230] one can ascribe appearance of this line shape to coupling to the INS resonance and the resonance energy can be estimated as a peak to dip distance. For the data in panel (d) the peak and dip positions were fitted and the estimate

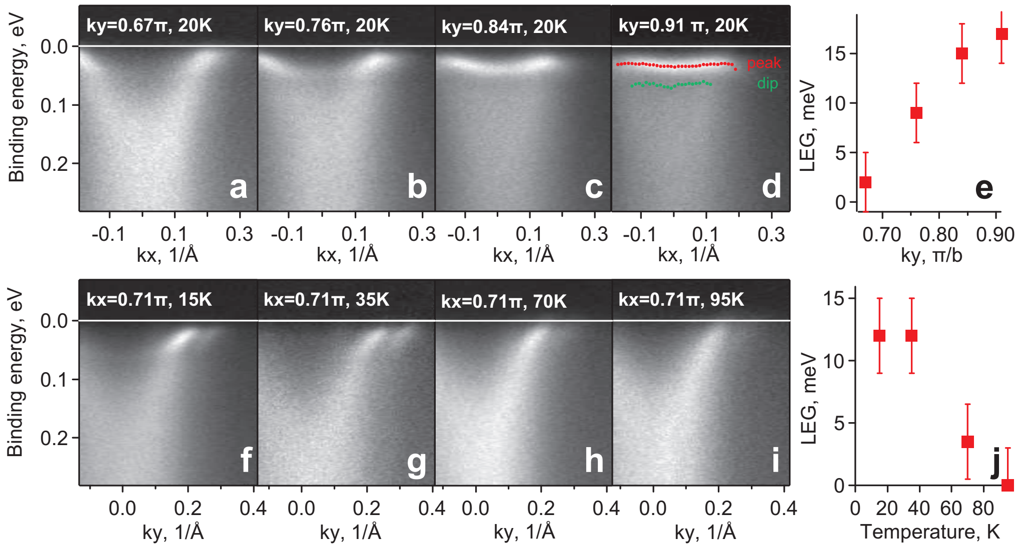

Figure 5.19: Superconducting component. (a)–(d) opening of a superconducting gap and enhancement of the band renormalization effects when approaching the antinodal point. Symbols in the image (d) denote the peak and the dip positions extracted from the EDC's comprising this data set. (e) extracted value of the superconducting gap. (f-g) evolution of the spectral weight and the gap (j) as a function of temperature. The spectra were measured from a freshly cleaved $(Y_{1-x}Ca_x)BaCu_3O_{7-\delta}$, ($x$=0.15±0.03, T_C=77 K) using linearly polarized light, $h\nu = 50$ eV.

for the resonance energy gave (33 ± 3)meV, which is in good agreement with the data for $(Y_{0.85}Ca_{0.15})Ba_2Cu_3O_7$ ($T_C = 75$ K) reported in Ref. [201]. This proves the conclusions about the mode origin made earlier for Bi-2212 to be equally applicable for the YBCO case, hence backing their generality.

To account for the prevalence of the superconducting component for Ca substituted sample, in addition to the matrix elements effects, one needs to assume the appearance of another cleavage plane. The analysis of the crystal structure suggests that the additional cleavage is most likely to happen within the Y-layer, since in this case the topmost CuO_2 plane would be too strongly disrupted to give a spectrum similar to the bulk (including but not limited to the bilayer splitting), while the nearest to the surface bilayer, being practically undisturbed and sharing the charge from both adjacent chain layers, would result in a signal corresponding to the superconducting component. In view of the different ionic radii of Ca (1.18 Å) and Y (0.89 Å) the cleavage over the Y-layer appears favourable also due to the slackening introduced by 15% Ca substitution, however tunneling data may be necessary to irrevocably settle this particular issue concerning Ca substitution.

5.9 Summary

Unlike the well studied Bi-2212 family of cuprates, ARPES on Y-123 turns out to be much more complicated. The observed spectra have a strong contribution from the strong overdoped surface component with the hole doping level of about $x \approx 0.30$, which is weakly dependent on the sample stoichiometry. In a strict sense the term “surface state” is not the best description for the surface component as this component is not a new state that results from the introduced upon cleavage interface breaking the translational symmetry, but is derived from the same orbitals as the bulk bands. The fact that the surface component develops no signs of superconductivity is a mere consequence of the unusually high doping level. This conclusion is supported by the fact that the overdoped bands give rise to the Fermi surface and band structure consistent with the predictions of the LDA calculations, as well as, from the dependence of the photoemission matrix element on the excitation energy, which closely follows that of the superconducting bulk component. The use of specific experimental geometry allows one to enhance the signal coming from the superconducting component. In particular, experiments with circularly polarized light bundled with simple theoretical considerations can be used to separate the surface and the bulk components. This type of experiments also suggests that the overdoped component is mainly localized in the topmost CuO_2 bilayer, while the next bilayers represent bulk and retain superconductivity.

Using partially Ca substituted samples it was possible to obtain spectra with a strongly suppressed overdoped component. This can be explained by a shift of the most probable cleavage plane from the Ba–O interface to the Y layer. Spectra from the Ca substituted sample clearly reveal a sizable superconducting gap, and strong renormalization effects in the vicinity of the antinodal point. The fact that the renormalization vanishes above T_C and has strong momentum dependence, diminishing away from the X/Y point, strongly suggests that the reason for this renormalization in Y-123 is coupling of the electronic subsystem to spin resonance, similar to the case of Bi-2212.

Appendix A

Kramers-Kronig transformation using FFT

When doing numerical modeling of the spectral function, it is necessary to know the self-energy. Often one deals with self-energy models that give relatively simple mathematical relations either for the imaginary or for the real part of the self-energy, but no such simple formulae being available for the complementary part. In principle it is possible to calculate the complementary part doing the direct integration of the Kramers-Kronig relations (1.31). However, keeping an adequate level of accuracy requires a small integration step of about 1 meV and a rather extended integration range of 2–5 eV. The former is necessary to preserve the fine structure in the self-energy, while the latter is needed to minimize the errors due to the truncation of the integration domain. This means that one has to handle data arrays consisting of about $N = 2000 - 5000$ points. As an example consider the imaginary part of the self-energy defined on the grid of length N: $\{\mathrm{Im}\,\Sigma_i\}, i = 0, ..., N-1$. The number of mathematical operations necessary to get the value of the real part of the self-energy $\mathrm{Re}\,\Sigma_m$ at some grid point m would be proportional to N. Then the number of operations that are necessary to calculate the whole line shape $\{\mathrm{Re}\,\Sigma_j\}, j = 0, ..., N-1$ of the real part of the self-energy becomes proportional to N^2. This makes the calculations very slow, especially when the model is used for fitting the experimental data and has to be recalculated many times for different fit parameters. However the problem is not so desperate as more advanced methods can be used [231,232].

From the formula (1.31) we see that the real part of the self-energy is simply a convolution of the imaginary part with the kernel $h(\omega) = -1/(\pi\omega)$:

$$\mathrm{Re}\,\Sigma(\omega) = \{\mathrm{Im}\,\Sigma \star h\}(\omega). \tag{A.1}$$

Recalling that the Fourier transform of the convolution is a product of Fourier transforms [†] of the convoluted functions and that $\mathfrak{F}\{h\}(t) = -i\,\mathrm{sign}(t)$ one finds:

$$\begin{aligned} &\mathfrak{F}\{\mathrm{Re}\,\Sigma(\omega)\}(t) = -i\ \mathrm{sign}(t)\,\mathfrak{F}\{\mathrm{Im}\,\Sigma(\omega)\}(t) \text{ or,} \\ &\mathrm{Re}\,\Sigma(\omega) = \mathfrak{F}^{-1}\{-i\ \mathrm{sign}(t)\,\mathfrak{F}\{\mathrm{Im}\,\Sigma(\omega)\}(t)\}(\omega). \end{aligned} \tag{A.2}$$

In practice the self-energy values are defined in the discrete points within a limited energy range. Assume that $\Sigma(\omega)$ is sampled in the N points that are equally spaced in the range $(-\Omega_{\mathrm{max}}/2,\ \Omega_{\mathrm{max}}/2)$ where the self-energy notably differs from zero, while outside this energy range it can be safely neglected. Let $\Sigma_m = \Sigma(m\Omega_{\mathrm{max}}/N)$ be the self-energy values at the vertices of the introduced grid $m = -N/2, ..., N/2 - 1$. Then for any $\omega \in (-\Omega_{\mathrm{max}}/2,\ \Omega_{\mathrm{max}}/2)$ real and imaginary part of the self-energy can be interpolated using the finite Fourier series:

$$\begin{aligned} \mathrm{Re}\,\Sigma(\omega) &= \sum_{n=-N/2}^{N/2-1} p_n \exp(2\pi i \frac{\omega n}{\Omega_{\mathrm{max}}}), \\ \mathrm{Im}\,\Sigma(\omega) &= \sum_{n=-N/2}^{N/2-1} q_n \exp(2\pi i \frac{\omega n}{\Omega_{\mathrm{max}}}), \end{aligned} \tag{A.3}$$

where

$$\begin{aligned} p_n &= \frac{1}{N} \sum_{m=-N/2}^{N/2-1} \mathrm{Re}\,\Sigma_m \exp(2\pi i \frac{nm}{N}), \\ q_n &= \frac{1}{N} \sum_{m=-N/2}^{N/2-1} \mathrm{Im}\,\Sigma_m \exp(2\pi i \frac{nm}{N}). \end{aligned} \tag{A.4}$$

Substituting (A.3) into (A.2) one immediately finds that there is a simple connection between p_n and q_n:

$$p_n = -i\,\mathrm{sign}(n) q_n, \tag{A.5}$$

which enables an efficient calculation of $\mathrm{Re}\,\Sigma_m$ by $\mathrm{Im}\,\Sigma_m$, or vice versa. The recipe is very simple. Applying discrete fast Fourier transform (FFT) to $\{\mathrm{Im}\,\Sigma_m\}$, $m = -N/2, ..., N/2 - 1$, the array of coefficients $\{q_m\}$ can be obtained. Then using (A.5), the coefficients $\{p_m\}$ are found, which upon inverse DFFT result in the array $\{\mathrm{Re}\,\Sigma_m\}$.

[†] Here $\mathfrak{F}$ is defined as $\mathfrak{F}\{g\}(\omega) = \int g(x) \exp(+i\omega x) \mathrm{d}x$.

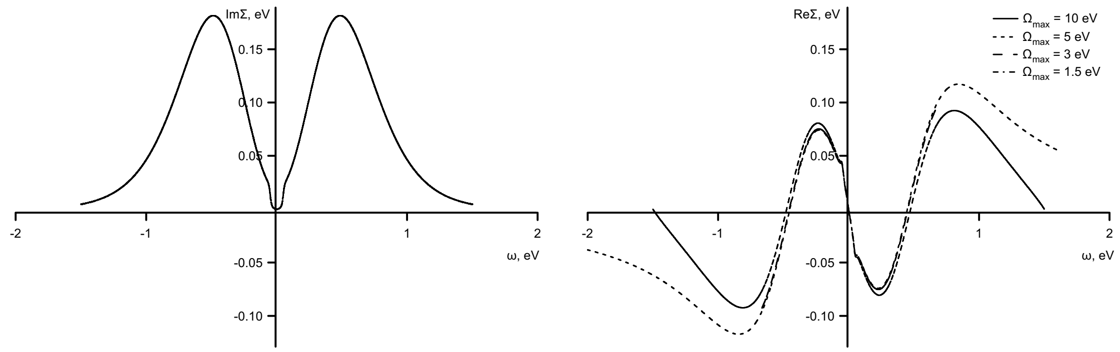

Figure A.1: Result of calculation $\mathrm{Re}\,\Sigma(\omega)$ by $\mathrm{Im}\,\Sigma(\omega)$ using DFFT transformation.

If N is a product of small integers, the number of operations required by standard FFT/IFFT algorithms is of the order of $N \ln N$. This gives appreciable speed up of the calculations as compared to N^2 obtained with direct integration of the Kramers-Kronig relations. For instance, for the grid size $N = 100$ the calculation would run about 100 times faster.

Figure A.1 illustrates the sensitivity of the method to the choice of the cut-off frequency Ω_{max}. As can be seen from the plots, when tails of $\mathrm{Im}\,\Sigma(\omega)$ are cut then there could be notable deviations, although in the low energy region $\omega \in (-0.5, 0.5)$ the deviations are negligible.

Publication List

1. V. B. Zabolotnyy, S. V. Borisenko, A. A. Kordyuk, J. Geck, D. S. Inosov, A. Koitzsch, J. Fink, M. Knupfer, B. Büchner, S.-L. Drechsler, H. Berger, A. Erb, M. Lambacher, L. Patthey, V. Hinkov, and B. Keimer, *Momentum and temperature dependence of renormalization effects in the high-temperature superconductor* $YBa_2Cu_3O_{7-\delta}$, Phys. Rev. B **76**, 064519 (2007).

2. J. Geck, S. V. Borisenko, H. Berger, H. Eschrig, J. Fink, M. Knupfer, K. Koepernik, A. Koitzsch, A. A. Kordyuk, V. B. Zabolotnyy, and B. Büchner *Anomalous quasiparticle renormalization in* $Na_{0.73}CoO_2$*: Role of interorbital interactions and magnetic correlations* Phys. Rev. Lett. **99**, 046403 (2007).

3. V. B. Zabolotnyy, S. V. Borisenko, A. A. Kordyuk, D. S. Inosov, A. Koitzsch, J. Geck, J. Fink, M. Knupfer, B. Büchner, S.-L. Drechsler, V. Hinkov, B. Keimer, and L. Patthey, *Disentangling surface and bulk photoemission using circularly polarized light*, Phys. Rev. B **76**, 024502 (2007).

4. D. S. Inosov, S. V. Borisenko, I. Eremin, A. A. Kordyuk, V. B. Zabolotnyy, J. Geck, A. Koitzsch, J. Fink, M. Knupfer, B. Büchner, H. Berger, and R. Follath, *Relation between the one-particle spectral function and dynamic spin susceptibility of superconducting* $Bi_2Sr_2CaCu_2O_{8+\delta}$, Phys. Rev. B **75**, 172505 (2007).

5. A. A. Kordyuk, V. B. Zabolotnyy, D. S. Inosov and S. V. Borisenko, *From tunneling to photoemission: Correlating two spaces*, J. Electron Spectrosc. Relat. Phenom., 91, **159**, (2007).

6. D. V. Evtushinsky, A. A. Kordyuk, S. V. Borisenko, V. B. Zabolotnyy, M. Knupfer, J. Fink, B. Büchner, A. V. Pan, A. Erb, C. T. Lin, and H. Berger, *Unadulterated spectral function of low-energy quasiparticles in* $Bi_2Sr_2CaCu_2O_{8+\delta}$, Phys. Rev. B **74**, 172509 (2006).

7. J. Fink, A. Koitzsch, J. Geck, V. Zabolotnyy, M. Knupfer, B. Büchner, A. Chubukov, and H. Berger, *Reevaluation of the coupling to a bosonic mode of the charge carriers in* $(Bi,Pb)_2Sr_2CaCu_2O_{8+\delta}$ *at the antinodal point*, Phys. Rev. B **74**, 165102 (2006).
8. A. A. Kordyuk, S. V. Borisenko, V. B. Zabolotnyy, J. Geck, M. Knupfer, J. Fink, B. Büchner, C. T. Lin, B. Keimer, H. Berger, A. V. Pan, Seiki Komiya, and Yoichi Ando, *Constituents of the quasiparticle spectrum along the nodal direction of high-*T_C *Cuprates*, Phys. Rev. Lett. **97**, 017002 (2006).
9. A. Koitzsch, S. V. Borisenko, J. Geck, V. B. Zabolotnyy, M. Knupfer, J. Fink, P. Ribeiro, B. Büchner, and R. Follath, *Current spinon-holon description of the one-dimensional charge-transfer insulator* $SrCuO_2$*: Angle-resolved photoemission measurements* , Phys. Rev. B **73**, 201101 (2006).
10. S. V. Borisenko, A. A. Kordyuk, V. Zabolotnyy, J. Geck, D. Inosov, A. Koitzsch, J. Fink, M. Knupfer, B. Büchner, V. Hinkov, C. T. Lin, B. Keimer, T. Wolf, S. G. Chiuzbaian, L. Patthey, and R. Follath, *Kinks, nodal bilayer splitting, and interband scattering in* $YBa_2Cu_3O_{6+x}$, Phys. Rev. Lett. **96**, 117004 (2006).
11. S. V. Borisenko, A. A. Kordyuk, A. Koitzsch, J. Fink, J. Geck, V. Zabolotnyy, M. Knupfer, B. Büchner, H. Berger, M. Falub, M. Shi, J. Krempasky, and L. Patthey, *Parity of the pairing bosons in a high-temperature Pb-*$Bi_2Sr_2CaCu_2O_8$ *bilayer superconductor by angle-resolved photoemission spectroscopy*, Phys. Rev. Lett. **96**, 067001 (2006).
12. V. B. Zabolotnyy, S. V. Borisenko, A. A. Kordyuk, J. Fink, J. Geck, A. Koitzsch, M. Knupfer, B. Büchner, H. Berger, A. Erb, C. T. Lin, B. Keimer, and R. Follath, *Effect of Zn and Ni impurities on the quasiparticle renormalization of superconducting Bi-2212*, Phys. Rev. Lett. **96**, 037003 (2006).
13. A. Koitzsch, S. V. Borisenko, D. Inosov, J. Geck, V. B. Zabolotnyy, H. Shiozawa, M. Knupfer, J. Fink, B. Büchner, E. D. Bauer, J. L. Sarrao, and R. Follath, *Observing the heavy fermions in* $CeCoIn_5$ *by angle-resolved photoemission*, Physica C, **460-462**, 666 (2007).
14. D. S. Inosov, S. V. Borisenko, I. Eremin, A. A. Kordyuk, V. B. Zabolotnyy, J. Geck, A. Koitzsch, J. Fink, M. Knupfer and B. Büchner, *About the relation*

between the quasiparticle Green's function in cuprates obtained from ARPES data and the magnetic susceptibility, Physica C **460-462**, 939, (2007).

15. D. S. Inosov, A. A. Kordyuk, S. V. Borisenko, V. B. Zabolotnyy, J. Fink, M. Knupfer, B. Büchner, R. Follath, V. Hinkov, B. Keimer, H. Berger, "*Waterfalls*" *phenomenon in superconducting cuprates*, arXiv:cond-mat/0702374 (to be published).

16. A. Gruneis, C. Attaccalite, T. Pichler, V. Zabolotnyy, H. Shiozawa, S.L. Molodtsov, D. Inosov, A. Koitzsch, M. Knupfer, J. Schiessling, R. Follath, R. Weber, P. Rudolf, L. Wirtz, A. Rubio, *Electron-electron correlation in graphite*, arXiv:0704.2682 (to be published).

17. S. V. Borisenko, A. A. Kordyuk, A. N. Yaresko, V. B. Zabolotnyy, D. S. Inosov, R. Schuster, B. Büchner, R. Weber, R. Follath, L. Patthey, H. Berger, *Pseudogap and charge density waves in two dimensions*, arXiv:0704.1544 (to be published).

Bibliography

[1] K. Onnes, Comm. Leiden **120 b** (1911).

[2] J. Bardeen, L. N. Cooper, and J. R. Schrieffer, Phys. Rev. **106**, 162 (1957).

[3] J. Bardeen, Phys. Rev. **79**, 167 (1950).

[4] J. Bardeen, Phys. Rev. **80**, 567 (1950).

[5] J. Bardeen, Phys. Rev. **81**, 829 (1951).

[6] C. E. Gough, Nature **326**, 855 (1987).

[7] M. Lorenz et al., Journal of Low Temperature Physics **117**, 527 (1999).

[8] N. P. Seregin, F. S. Nasredinov, and P. P. Seregin, J. Phys.: Condens. Matter **13**, 149 (2001).

[9] C.-O. Almbladh, Journal of Physics **35**, 127 (2006).

[10] L. Hedin and J. Lee, Journal of Electron Spectroscopy and Related Phenomena **124**, 289 (2002).

[11] G. D. Mahan, Phys. Rev. B **2**, 4334 (1970).

[12] H. R. Hertz, Annalen der Physik **267**, 983 (1887).

[13] A. Einstein, Annalen der Physik **325**, 199 (1906).

[14] W. E. Speicer, Phys. Rev. **112**, 114 (1958).

[15] C. N. Berglund and W. E. Spicer, Phys. Rev. **136**, A1030 (1964).

[16] S. Hüfner, *Photoelectron Spectroscopy*, Springer-Verlag, Berlin, 1995.

[17] C. Caroli, D. Lederer-Rozenblatt, B. Roulet, and D. Saint-James, Phys. Rev. B **8**, 4552 (1973).

[18] J. B. Pendry, Surface Science **57**, 679 (1975).

[19] A. Bansil et al., Journal of Physics and Chemistry of Solids **63**, 2175 (2002).

[20] L. Landau and E. Lifshitz, *Quantum mechanics. Nonrelativistic theory.*, Pergamon Press, 1977.

[21] F. Pforte, T. Michalke, A. Gerlach, A. Goldmann, and R. Matzdorf, Phys. Rev. B **63**, 115405 (2001).

[22] T. Miller, W. E. McMahon, and T.-C. Chiang, Phys. Rev. Lett. **77**, 1167 (1996).

[23] W. Eberhardt and F. J. Himpsel, Phys. Rev. B **21**, 5572 (1980).

[24] A. M. Bradshaw and N. V. Richardson, Pure & Appl. Chem. **68**, 457 (1996).

[25] Y. Aiura et al., Phys. Rev. Lett. **91**, 256404 (2003).

[26] L. Roca et al., Applied Surface Science **212**, 62 (2003).

[27] M. P. Seach and W. A. Dench, Surface and interface analysis **1**, 2 (1979).

[28] L. Hedin and J. D. Lee, Phys. Rev. B **64**, 115109 (2001).

[29] M. R. Norman and M. Randeria, Phys. Rev. B **59**, 11191 (1990).

[30] N. Barret, E. E. Krasovskii, J.-M. Themlin, and V. N. Strokov, Phys. Rev. B **71** (2005).

[31] N. Nücker et al., Phys. Rev. B **39**, 12379 (1989).

[32] A. Damascelli, Z. Hussain, and Z.-X. Shen, Rev. Mod. Phys. **75**, 473 (2003).

[33] J. Olde et al., Phys. Rev. B **41**, 9958 (1990).

[34] P. O. Nilsson and N. Dählback, Solid State Comm. **29**, 303 (1978).

[35] V. N. Strocov, H. I. Starnberg, P. O. Nilsson, H. E. Brauer, and L. J. Holleboom, Phys. Rev. Lett. **79**, 467 (1997).

[36] V. N. Strocov et al., Phys. Rev. Lett. **81**, 4943 (1998).

[37] M. Randeria et al., Phys. Rev. Lett. **74**, 4951 (1995).

[38] J. D. Koralek and J. F. Douglas, Phys. Rev. Lett. **96** (2006).

[39] G. D. Mahan, *Many particle physics.*, Plenum Press, 1981.

[40] H. Bruus and K. Flensberg, *Many-body quantum theory incondensed matter physics*, Oxford Press, New York, 1981.

[41] A. A. Kordyuk et al., Phys. Rev. B **71**, 214513 (2005).

[42] S. Engelsberg and J. R. Schrieffer, Phys. Rev. **131**, 993 (1963).

[43] B. I. Lundqvist, Zeitschrift für Physik B Condensed Matter **6**, 206 (1967).

[44] J. Schäfer et al., Phys. Rev. Lett. **92**, 097205 (2004).

[45] T. Dahm, P. J. Hirschfeld, L. Zhu, and D. J. Scalapino, Phys. Rev. B **71**, 1098 (2005).

[46] J. M. Luttinger, Phys. Rev. **119**, 1153 (1960).

[47] M. Oshikawa, Phys. Rev. Lett. **84**, 3370 (2000).

[48] J. M. Luttinger, Phys. Rev. **121**, 942 (1961).

[49] T. A. Maier, T. Pruschke, and M. Jarrell, Phys. Rev. B **66**, 075102 (2002).

[50] C. Gröber, M. G. Zacher, and R. Eder, cond-mat , 9902015 (1999).

[51] Y.-L. Liu, Phys. Rev. B **72**, 155104 (2005).

[52] I. Dzyaloshinskii, Phys. Rev. B **68**, 085113 (2003).

[53] T. D. Stanescu, P. Phillips, and T.-P. Choy, Phys. Rev. B **75**, 104503 (2007).

[54] C. Gros, B. Edegger, V. N. Muthukumar, and P. W. Anderson, PNAS **103**, 14298 (2006).

[55] R. Sensarma, M. Randeria, and N. Trivedi, Phys. Rev. Lett. **98**, 027004 (2007).

[56] L. N. Cooper, Phys. Rev. **104**, 1189 (1956).

[57] M. Eschrig, Advances in Physics **55**, 47 (2006).

[58] D. D. Osheroff, Rev. Mod. Phys. **69**, 667 (1997).

[59] J. Bardeen, L. N. Cooper, and J. R. Schrieffer, Phys. Rev. **108**, 1175 (1957).

[60] H. Fröhlich, Phys. Rev. **79**, 845 (1950).

[61] N. N. Bogoliubov, Nuovo Cimento **7**, 794 (1958).

[62] J. G. Valatin, Nuovo Cimento **7**, 843 (1958).

[63] N. Bulut and D. J. Scalapino, Phys. Rev. B **54**, 14971 (1996).

[64] H. Matsui et al., Phys. Rev. Lett. **90**, 217002 (2003).

[65] P. Dai, H. A. Mook, R. D. Hunt, and F. Doğan, Phys. Rev. B **63**, 054525 (2001).

[66] H. F. Fong et al., Phys. Rev. Lett. **75**, 316 (1995).

[67] H. F. Fong, B. Keimer, D. Reznik, D. L. Milius, and I. A. Aksay, Phys. Rev. B **54**, 6708 (1996).

[68] J. Fink et al., Phys. Rev. B **74**, 165102 (2006).

[69] A. Kaminski et al., Phys. Rev. Lett. **86**, 1070 (2001).

[70] T. Cuk et al., Phys. Rev. Lett. **93**, 117003 (2004).

[71] A. D. Gromko et al., Phys. Rev. B **68**, 174520 (2003).

[72] T. K. Kim et al., Phys. Rev. Lett. **91**, 167002 (2003).

[73] A. V. Chubukov and M. R. Norman, Phys. Rev. B **70**, 174505 (2004).

[74] M. Eschrig and M. R. Norman, Phys. Rev. B **67**, 144503 (2003).

[75] W. Assmust and W. Schmidbauer, Supmand. Sci. Technol. **6**, 555 (1993).

[76] R. M. Hazen et al., Phys. Rev. Lett. **60**, 1174 (1988).

[77] T. M. Shaw et al., Phys. Rev. B **37**, 9856 (1988).

[78] S. H. Pan, E. W. Hudson, J. Ma, and J. C. Davis, Appl. Pys. Lett. **73**, 58 (1998).

[79] S. H. Pan et al., Nature **413**, 282 (2001).

[80] V. Hinkov et al., Nature **430**, 650 (2004).

[81] C. T. Lin, W. Zhou, and W. Y. Liang, Physica C **195**, 291 (1992).

[82] V. I. Voronkova and T. Wolf, Physica C **218**, 175 (1993).

[83] D. Iwanenko and I. Pomeranchuk, Phys. Rev. **65**, 343 (1944).

[84] F. R. Elder, R. V. Langmuir, and H. C. Pollock, Phys. Rev. **74**, 52 (1948).

[85] Procedings of EPAC, *First results of the UE212 quasiperiodic elliptical electromagnetic undulators at SLS*, Paris, France, 2002.

[86] A. A. Kordyuk, S. V. Borisenko, M. Knupfer, and J. Fink, Phys. Rev. B **67**, 064504 (2003).

[87] P. Aebi et al., Phys. Rev. Lett. **72**, 2757 (1994).

[88] J. G. Bednorz and K. A. Müller, Z. Phys. B **64**, 189 (1986).

[89] M. K. Wu et al., Phys. Rev. Lett. **58**, 908 (1987).

[90] H. Maeda, Y. Tanaka, M. Fukutomi, and T. Asano, Jpn. J. Appl. Phys., Part 2 **4**, L209 (1988).

[91] S. A. Sunshine et al., Phys. Rev. B **38**, 893 (1988).

[92] H. W. e. a. Zandbergen, Physica C **156**, 325 (1988).

[93] J. M. Tarascon et al., Phys. Rev. B **37**, 9382 (1988).

[94] P. A. Sterne and C. S. Wang, Journal of Physics C: Solid State Physics **21**, L949 (1988).

[95] G. Calestani, C. Rizzoli, M. G. Francesconi, and G. D. Andreetti, Physica C: Superconductivity **161**, 598 (1989).

[96] Y. Ito et al., Phys. Rev. B **58**, 2851 (1998).

[97] P. A. Miles et al., Phys. Rev. B **55**, 14632 (1997).

[98] H. Lin, S. Sahrakorpi, R. S. Markiewicz, and A. Bansil, Phys. Rev. Lett. **96**, 097001 (2006).

[99] A. Bansil, M. Lindroos, S. Sahrakorpi, and M. R. S., Phys. Rev. B **71** (2005).

[100] D. L. Feng et al., Phys. Rev. Lett. **86**, 5550 (2001).

[101] A. A. Kordyuk et al., Phys. Rev. B **66**, 014502 (2002).

[102] M. Izquierdo, J. Avila, L. Roca, G. Gu, and M. C. Asensio, Phys. Rev. B **72**, 174517 (2005).

[103] A. Mans et al., Phys. Rev. Lett. **96**, 107007 (2006).

[104] V. Arpiainen and M. Lindroos, Phys. Rev. Lett. **97**, 037601 (2006).

[105] A. Koitzsch et al., Phys. Rev. B **69**, 220505 (2004).

[106] V. N. Strocov, R. Claessen, and P. Blaha, Phys. Rev. B **68**, 144509 (2003).

[107] H. Ding et al., Phys. Rev. Lett. **76**, 1533 (1996).

[108] Y.-D. Chuang et al., Phys. Rev. Lett. **83**, 3717 (1999).

[109] S. V. Borisenko et al., Phys. Rev. Lett. **84**, 4453 (2000).

[110] M. C. Asensio et al., Phys. Rev. B **67**, 014519 (2003).

[111] A. Kaminski et al., Nature **416**, 610 (2002).

[112] S. V. Borisenko, K. A. Kordyuk, A. A., M. Knupfer, B. H. Fink, J and, and C. T. Lin, Nature, Brief communication arrising **2**, 1 (2004).

[113] S. V. Borisenko et al., Phys. Rev. Lett. **92**, 207001 (2004).

[114] J. M. Luttinger, Phys. Rev. **118**, 1417 (1960).

[115] T. Valla et al., Phys. Rev. Lett. **85**, 828 (2000).

[116] T. Valla et al., Science **285**, 2110 (1999).

[117] P. V. Bogdanov et al., Phys. Rev. Lett. **85**, 2581 (2000).

[118] M. R. Norman et al., Phys. Rev. Lett. **79**, 3506 (1997).

[119] A. W. Sandvik, D. J. Scalapino, and N. E. Bickers, Phys. Rev. B **69**, 094523 (2004).

[120] P. D. Johnson et al., Phys. Rev. Lett. **87**, 177007 (2001).

[121] A. A. Kordyuk et al., Phys. Rev. Lett. **92**, 257006 (2004).

[122] T. P. Devereaux, T. Cuk, Z.-X. Shen, and N. Nagaosa, Phys. Rev. Lett. **93**, 117004 (2004).

[123] J. Shi et al., Phys. Rev. Lett. **92**, 186401 (2004).

[124] X. J. Zhou et al., Phys. Rev. Lett. **96**, 119702 (2006).

[125] T. Valla, Phys. Rev. Lett. **96**, 119701 (2006).

[126] T. Cuk et al., Phys. Status Solidi B **242**, 11 (2005).

[127] G.-H. Gweon et al., Nature **430**, 187 (2004).

[128] J. F. Douglas et al., Nature **446**, E5 (2007).

[129] Y. Sidis et al., Phys. Rev. Lett. **84**, 5900 (2000).

[130] Y. Sidis et al., arXiv:cond-mat/0006265v1 (2000).

[131] A. A. Kordyuk et al., Phys. Rev. Lett. **89**, 077003 (2002).

[132] S. V. Borisenko et al., Phys. Rev. Lett. **90**, 207001 (2003).

[133] A. A. Kordyuk et al., Phys. Rev. B **70**, 214525 (2004).

[134] O. K. Andersen, A. I. Liechtenstein, O. Jespen, and F. Paulsen, J. Phys. Chem. Solids **56**, 1573 (1995).

[135] H. F. Fong et al., Phys. Rev. Lett. **82**, 1939 (1999).

[136] M. Le Tacon et al., arXiv:cond-mat/0504287v3 (2005).

[137] Y. Gallais et al., Phys. Rev. Lett. **88**, 177401 (2002).

[138] N. Watanabe and N. Koshizuka, Phys. Rev. B **57**, 632 (1998).

[139] M. Käll, A. P. Litvinchuk, L. Börjesson, P. Berastegui, and L.-G. Johansson, Phys. Rev. B **53**, 3566 (1996).

[140] M. Limonov, D. Shantsev, S. Tajima, and A. Yamanaka, Phys. Rev. B **65**, 024515 (2001).

[141] S. Pailhès et al., Phys. Rev. Lett. **93**, 167001 (2004).

[142] I. Eremin, D. K. Morr, A. V. Chubukov, K. H. Bennemann, and M. R. Norman, Phys. Rev. Lett. **94**, 147001 (2005).

[143] O. K. Andersen, O. Jepsen, A. I. Lichtenstein, and I. I. Mazin, Phys. Rev. B **49**, 4145 (1996).

[144] H. P. Casalta et al., Physica C **258**, 321 (1996).

[145] H. F. Poulsen et al., Phys. Rev. B **53**, 15335 (1996).

[146] M. Houssay, J. Feldmannz, R. Clootsz, and A. M., Supercond. Sci. Technol. **11**, 44 (1998).

[147] J. D. Jorgensen et al., Phys. Rev. B **41**, 1863 (1990).

[148] K. Kakurai et al., Phys. Rev. B **48**, 3485 (1993).

[149] R. Liu et al., Phys. Rev. B **45**, 5614 (1992).

[150] H. Alloul, P. Mendels, H. Casalta, J. F. Marucco, and J. Arabski, Phys. Rev. Lett. **67**, 3140 (1991).

[151] P. Schleger, W. N. Hardy, and B. X. Yang, Physica C **176**, 261 (1991).

[152] D. C. Johnston, S. K. Sinha, A. J. Jacobson, and J. M. Newsam, Physica C **153-155**, 572 (1988).

[153] J. M. Tranquada et al., Phys. Rev. Lett. **60**, 156 (1988).

[154] S. Shamoto, M. Sato, J. M. Tranquada, B. J. Sternlieb, and G. Shirane, Phys. Rev. B **48**, 13817 (1993).

[155] N. H. Andersen, M. von Zimmermann, and T. Frello, Physica C **317-318**, 259 (1999).

[156] P. Schleger et al., Phys. Rev. Lett. **74**, 1446 (1995).

[157] P. Schleger et al., Physica C **241**, 103 (1995).

[158] W. Schwarz, O. Blaschko, G. Collin, and F. Marucco, Phys. Rev. B **48**, 6513 (1993).

[159] D. de Fontaine, G. Ceder, and M. Asta, Nature **343**, 544 (1990).

[160] J. Reyes-Gasga et al., Physica C **159**, 831 (1989).

[161] T. A. Zaleski and T. K. Kopeć, Phys. Rev. B **74**, 014504 (2006).

[162] B. V. Veal and A. P. Paulikas, Physica C **184**, 321 (1991).

[163] R. McCormack, D. de Fontaine, and G. Ceder, Phys. Rev. B **45**, 12976 (1992).

[164] J. S. Bobowski et al., arXiv:cond-mat/0612344 (2006).

[165] R. Liang, D. A. Bonn, and W. N. Hardy, Phys. Rev. B **73**, 180505 (2006).

[166] K. McElroy et al., Phys. Rev. Lett. **94**, 197005 (2005).

[167] G. Kinoda and T. Hasegawa, Phys. Rev. B **67**, 224509 (2003).

[168] H. Mashima et al., Phys. Rev. B **73**, 060502 (2006).

[169] J. Lee et al., Nature **442**, 546 (2006).

[170] K. C. Hewitt et al., Phys. Rev. B **69**, 064514 (2004).

[171] M. Merz et al., Phys. Rev. Lett. **80**, 5192 (1998).

[172] W. E. Pickett, R. E. Cohen, and H. Krakauer, Phys. Rev. B **42**, 8764 (1990).

[173] O. K. Andersen et al., Physica C **185-189**, 147 (1995).

[174] M. Z. Hasan et al., Phys. Rev. Lett. **92**, 246402 (2004).

[175] J. Geck et al., arXiv:cond-mat/0704.1048v2 .

[176] H. Ding et al., Phys. Rev. B **54**, R9678 (1996).

[177] A. Kaminski et al., Phys. Rev. Lett. **84**, 1788 (2000).

[178] S. V. Borisenko et al., Phys. Rev. B **64**, 094513 (2001).

[179] S. V. Borisenko et al., Phys. Rev. B **69**, 224509 (2004).

[180] A. Bansil and M. Lindroos, Phys. Rev. Lett. **83**, 5154 (1999).

[181] Z.-X. Shen and et al., Phys. Rev. B **70**, 1553 (1993).

[182] S. V. Borisenko et al., Phys. Rev. B **66**, 140509 (2002).

[183] A. A. Kordyuk et al., Phys. Rev. Lett. **97**, 017002 (2006).

[184] T. Cuk, Z.-X. Shen, A. Gromko, Z. Sun, and D. S. Dessau, Nature, brief communications arising **18**, 1 (2004).

[185] M. C. Schabel et al., Phys. Rev. B **57**, 6090 (1998).

[186] M. C. Schabel et al., Phys. Rev. B **57**, 6107 (1998).

[187] B. W. Veal and C. Gu, J. of Electron Spectroscopy and Related Phenomena **66**, 321 (1994).

[188] J. G. Tobin et al., Phys. Rev. B **45**, 5563 (1992).

[189] D. H. Lu et al., Phys. Rev. Lett. **86**, 4370 (2001).

[190] R. Liu et al., Phys. Rev. B **46**, 11056 (1992).

[191] M. C. Schabel et al., Phys. Rev. B **55**, 2796 (1997).

[192] P. Dai, M. Yethiraj, H. A. Mook, T. B. Lindemer, and F. Doğan, Phys. Rev. Lett. **77**, 5425 (1996).

[193] P. Dai, H. A. Mook, and F. Doğan, Phys. Rev. Lett. **80**, 1738 (1998).

[194] P. Dai et al., Science **284**, 1344 (1999).

[195] H. A. Mook et al., Phys. Rev. B **69**, 134509 (2004).

[196] H. A. Mook et al., Phys. Rev. B **66**, 144513 (2002).

[197] H. A. Mook, P. Dai, and F. Doğan, Phys. Rev. Lett. **88**, 097004 (2002).

[198] H. A. Mook, P. Dai, and F. Doğan, Phys. Rev. B **64**, 012502 (2001).

[199] J.-H. Chung et al., Phys. Rev. B **67**, 014517 (2003).

[200] H. A. Mook, M. Yethiraj, G. Aeppli, T. E. Mason, and T. Armstrong, Phys. Rev. Lett. **70**, 3490 (1993).

[201] S. Pailhès et al., Phys. Rev. Lett. **96**, 257001 (2006).

[202] S. Pailhès et al., Phys. Rev. B **71**, 220507 (2005).

[203] S. Pailhès et al., Phys. Rev. Lett. **91**, 237002 (2003).

[204] D. Reznik et al., Phys. Rev. Lett. **93**, 207003 (2004).

[205] H. He et al., Phys. Rev. Lett. **86**, 1610 (2001).

[206] H. A. Mook et al., Nature **395**, 580 (1998).

[207] P. Bourges et al., Science **288**, 1234 (2000).

[208] K. Gofron et al., J. Phys. Chem. Solids **54**, 1193 (1993).

[209] R. Claessen et al., Phys. Rev. B **44**, 2399 (1991).

[210] H. L. Edwards, J. T. Markert, and A. L. de Lozanne, Phys. Rev. Lett. **69**, 2967 (1992).

[211] C. Calandra, F. Manghi, and T. Minerva, Phys. Rev. B **46**, 3600 (1992).

[212] M. Presland, J. Tallon, R. Buckley, R. Liu, and N. Flower, Physica C **176**, 95 (1991).

[213] M. R. Norman, M. Eschrig, A. Kaminski, and J. C. Campuzano, Phys. Rev. B **64**, 184508 (2001).

[214] M. Eschrig and M. R. Norman, Phys. Rev. Lett. **89**, 277005 (2002).

[215] D. L. Feng et al., Phys. Rev. B **65**, 220501 (2002).

[216] N. Schroeder, R. Böttner, S. Ratz, U. Dietz, E. Gerhardt, and T. Wolf, Phys. Rev. B **47**, 5287 (1993).

[217] K. Ogawa, J. Fujiwara, H. Takei, and A. H., Physica C **190**, 39 (1991).

[218] M. Lindroos et al., Physica C **212**, 347 (1993).

[219] M. Beno et al., Appl. Phys. Lett. **51**, 57 (1987).

[220] M. Maki, T. Nishizaki, K. Shibata, and K. Norio, J. Phys. Soc. Japan **70**, 1877 (2001).

[221] S. H. Pan, E. W. Hudson, and J. C. Davis, Rev. Sci. Inst. **70**, 1459 (1999).

[222] R. S. List et al., Phys. Rev. B **38**, 11966 (1988).

[223] H. L. Edwards, D. J. Derro, A. L. Barr, J. T. Markert, and A. L. de Lozanne, Phys. Rev. Lett. **75**, 1387 (1995).

[224] D. J. Derro et al., Phys. Rev. Lett. **88**, 097002 (2002).

[225] P. J. Feibelman, Phys. Rev. Lett. **34**, 1092 (1975).

[226] D. Samuelsen and W. Schattke, Phys. Rev. B **51**, 2537 (1995).

[227] F. Pforte, T. Michalke, A. Gerlach, A. Goldmann, and R. Matzdorf, Phys. Rev. B **63**, 115405 (2001).

[228] R. L. Dubs, S. N. Dixit, and V. McKoy, Phys. Rev. B **32**, 8389 (1985).

[229] A. Baalmann, M. Neumann, W. Braun, and W. Radlik, Solid State Commun. **54**, 583 (1985).

[230] A. Abanov and A. V. Chubukov, Phys. Rev. Lett. **83**, 1652 (1999).

[231] D. W. Johnson, J. Phys. A: Math. Gen. **8**, 490 (1974).

[232] R. J. Henery, J. Phys. A: Math. Gen. **17**, 3415 (1984).

Acknowledgements

I want to thank my supervisor Prof. Bernd Büchner for the possibility to do my PhD research at IFW-Dresden and for his help in my work. Special gratitude should be expressed to Dr. Sergey Borisenko for his constant scientific and professional help. I want to thank all the members of the ARPES group for their criticism and comments during our discussions and preparation of the publications: Dr. Alexander Kordyuk, Prof. Jörk Fink, Roman Schuster, Dmytro Inosov, Dr. Martin Knupfer, Dr. Andreas Koitzch, Dr. Jochen Geck.

As no modern photoemission experiment would be possible without synchrotron light, I express my gratitude to synchrotron teams at BESSY and SLS, in particular to Dr. Rolf Follath, Dr. Luc Patthey, Dr. Gheorghe Chiuzbăian, Dr. Ramona Weber, Dr. Jorge Lobo, to Fritz Dubi and Christoph Hess.

Another important component of any experimental work consists of high quality samples, therefore I want to thank Vladimir Hinkov, Prof. Bernhard Keimer and Dr. Andreas Erb for the excellent Y-123 and impurity substituted Bi-2212 samples.

Special thanks to Dmytro Ínosov and Roman Schuster for their help with the LaTeX-system and for the corrections suggested while reading the manuscript of the thesis.

I want to appreciate all the brave attempts made by Dr. Roland Hübel and Ronny Schönfelder to prevent the “crazy physicists” from destroying all pieces of equipment and saving us from complete chaos in the Labs.